

**IONIC CONDUCTIVITY OF OXALIC ACID CROSSLINKED CHITOSAN  
AND APPLICATION IN ELECTRICAL DOUBLE LAYER CAPACITOR  
(EDLC)**

**IMAN BINTI ARIS FADZALLAH**

**FACULTY OF SCIENCE  
UNIVERSITY OF MALAYA  
KUALA LUMPUR**

**2015**

**IONIC CONDUCTIVITY OF OXALIC ACID CROSSLINKED  
CHITOSAN AND APPLICATION IN ELECTRICAL DOUBLE  
LAYER CAPACITOR (EDLC)**

**IMAN BINTI ARIS FADZALLAH**

**DISSERTATION SUBMITTED IN FULFILLMENT OF  
THE REQUIREMENTS FOR THE DEGREE OF  
MASTER OF SCIENCE**

**DEPARTMENT OF PHYSICS  
FACULTY OF SCIENCE  
UNIVERSITY OF MALAYA  
KUALA LUMPUR**

**2015**

# UNIVERSITI MALAYA

## ORIGINAL LITERARY WORK DECLARATION

Name of Candidate: **IMAN BINTI ARIS FADZALLAH**

I/C/Passport No:

Registration/Matric No.: **SGR100110**

Name of Degree: **MASTER OF SCIENCE**

Title of Project Paper/Research Report/Dissertation/Thesis ("this Work"):

**"IONIC CONDUCTIVITY OF OXALIC ACID CROSSLINKED CHITOSAN AND APPLICATION IN ELECTRICAL DOUBLE LAYER CAPACITOR (EDLC)"**

Field of Study: **ADVANCED CHEMISTRY**

I do solemnly and sincerely declare that:

- (1) I am the sole author/writer of this Work,
- (2) This Work is original,
- (3) Any use of any work in which copyright exists was done by way of fair dealing and for permitted purposes and any excerpt or extract from, or reference to or reproduction of any copyright work has been disclosed expressly and sufficiently and the title of the Work and its authorship have been acknowledged in this Work,
- (4) I do not have any actual knowledge nor do I ought reasonably to know that the making of this work constitutes an infringement of any copyright work,
- (5) I hereby assign all and every rights in the copyright to this Work to the University of Malaya ("UM"), who henceforth shall be owner of the copyright in this Work and that any reproduction or use in any form or by any means whatsoever is prohibited without the written consent of UM having been first had and obtained,
- (6) I am fully aware that if in the course of making this Work I have infringed any copyright whether intentionally or otherwise, I may be subject to legal action or any other action as may be determined by UM.

(Candidate Signature)

Date:

Subscribed and solemnly declared before,

Witness's Signature

Date:

Name

Designation

## ABSTRACT

In the present study, proton conducting solid polymer electrolytes (SPE) consisting of chitosan as polymer host, oxalic acid (OA) as proton donor and glycerol as plasticizer were prepared by solution casting method. Two systems of polymer conducting membrane composed of chitosan-oxalic acid and chitosan-oxalic acid-glycerol, namely System I and System II respectively. The ionic conductivity values for the membranes were obtained by performing electrochemical impedance spectroscopy. The membrane OA40 (containing 40 wt. % chitosan + 60 wt. % OA) in System I exhibits the highest conductivity value of  $4.96 \times 10^{-7} \text{ S cm}^{-1}$ . The membrane OG60 (containing 24 wt. % chitosan + 16 wt. % OA + 60 wt. % glycerol) in System II exhibits the highest conductivity value of  $9.12 \times 10^{-5} \text{ S cm}^{-1}$ . The ionic interaction between chitosan, OA and glycerol were studied using Fourier transform infrared (FTIR) spectroscopy. The FTIR study on System I reveals the interaction between chitosan and OA by deconvoluting the absorption peak between 1800 and  $1400 \text{ cm}^{-1}$ . Whereas in System II, the  $\text{-OH}$  characteristic band at  $3500 \text{ cm}^{-1}$  become broader with the addition of glycerol which indicates the interaction between chitosan and glycerol. The amorphousness of the highest conducting membranes in both systems was confirmed by x-ray diffraction (XRD) evaluation. The crystallinity percentage was determined to be 13 and 11 % for membranes OA40 and OG60 respectively. The OG60 membrane was then fabricated into electrical double layer capacitor (EDLC) devices with symmetrical porous carbon electrodes. The electrochemical stability window was measured by linear sweep voltammetry (LSV) shows wide potential up to 2.2 V. The specific capacitance ( $C_s$ ) obtained from galvanostatic charge-discharge analysis is  $13 \text{ F g}^{-1}$  with applied potential at 1 mA.

## ABSTRAK

Dalam kajian ini, polimer elektrolit pepejal (SPE) mengalirkan proton mengandungi Chitosan sebagai hos polimer, asid oksalik (OA) sebagai penyumbang proton dan gliserol sebagai pemplastik telah disediakan dengan menggunakan teknik tuangan larutan. Dua system polimer elektrolit terdiri dari chitosan-OA dan chitosan-OA-gliserol, masing-masing dinamakan sebagai Sistem I dan Sistem II. Nilai ionic kekonduksian membran telah didapati dengan menggunakan 'electrochemical impedance spectroscopy'. Membran OA40 (mengandungi 40 wt. % chitosan + 60 wt. % OA) dari Sistem I menunjukkan nilai kekonduksian tertinggi iaitu  $4.96 \times 10^{-7} \text{ S cm}^{-1}$ . Membran OG60 (mengandungi 24 wt. % chitosan + 16 wt. % OA + 60 wt. % gliserol) dari Sistem II pula menunjukkan nilai kekonduksi tertinggi  $9.12 \times 10^{-5} \text{ S cm}^{-1}$ . Interaksi ionik antara chitosan, OA dan gliserol dipelajari dengan menggunakan 'Fourier transform infrared' (FTIR) spektroskopi. Dalam Sistem I, 'deconvolution' puncak penyerapan antara  $1800$  dan  $1400 \text{ cm}^{-1}$  membongkar interaksi antara chitosan dan OA. Manakala dalam Sistem II, jalur karakteristik  $\text{-OH}$  pada  $3500 \text{ cm}^{-1}$  menjadi semakin lebar dengan penambahan gliserol; menunjukkan interaksi antara chitosan dan gliserol. Nilai amorfus bagi membran yang mempunyai nilai kekonduksi tertinggi telah disahkan dengan x-ray diffraction (XRD). Nilai peratusan kekristalan ialah 13 % dan 11 % bagi membran OA40 dan OG60 masing-masing. Kemudian membran OG60 difabrikasi menjadi peranti 'electrical double layer capacitor' (EDLC) dengan elektrod simetri poros karbon. Tetingkap stabil elektrokimia diukur dengan 'linear sweep voltammetry' (LSV) menunjukkan potensi yang luas sehingga 2.2 V. Kapasiti spesifik ( $C_s$ ) yang diperoleh dari analisa galvanostatik caj-nyahcaj ialah  $13 \text{ F g}^{-1}$  dengan potensi yang dikenakan pada 1 mA.

## **ACKNOWLEDGEMENT**

All praises to Allah; the Exalted and the Almighty for giving me the blessing and opportunity to pursue my education. I would like to express my gratitude to both my supervisors; Prof. Dr. Abdul Kariem Arof and Associate Prof. Dr. Siti Rohana Majid for guiding and educating me with patience and perseverance; also Prof Dr. M.A. Careem with his generous assistance and ideas. Not forgetting, Prof. Dr. Rosiyah who introduced me to the world of polymer with her vast experience and insight which served as the foundation in my understanding. To quoted Dan Rather; the dream begins with a teacher who believes in you, who tugs and pushes and leads you to the next plateau, sometimes poking you with a sharp stick called 'truth'. I also would like to thank University of Malaya for the PPP grant award for making this research possible. My appreciation extends to the science officers from Department of Physics, University of Malaya and COMBICAT for their cooperation. Thanks to the colleagues from Centre for Ionics University of Malaya (C.I.U.M) with their assistance and boundless help; to 'kakang-kakang' seniors in Polymer Lab, Department of Chemistry, University of Malaya- I am glad that we met. My heartfelt thanks to Syahidah, Ati and Term for being there for me during my ups and downs; Hana-Deqna and Zila for guiding me during my earlier days in C.I.U.M. My endless gratitude goes to my parents; Abi and Umami in supporting me for each step I took. Their infinite love cannot be replaced and I prayed to Allah the Almighty shower mercy on them as they have nourished me with education since i was small. I am also thankful to my siblings; Mujalong, Yamo, Mawan, Ijat and Rayyan. The bickering, sulking and laughing are important ingredients that make us as the Aris' crews. My gratitude can be summarized in what Friedrich Nietzsche said 'The essence of all beautiful art, all great art, is gratitude'.

**IMAN ARIS FADZALLAH**

# LIST OF CONTENTS

<b>Content</b>	<b>Page</b>
<i>Declaration</i>	ii
<i>Abstract</i>	iii
<i>Abstrak</i>	iv
<i>Acknowledgement</i>	v
<i>List of Contents</i>	vi
<i>List of Figures</i>	x
<i>List of Tables</i>	xvi
<i>List of Journal &amp; Seminar/ Conferences Presentation</i>	xviii
<i>List of Abbreviations</i>	xix
<b>CHAPTER 1: INTRODUCTION</b>	1
1.1 Research background	1
1.2 Scope and objectives of the research	2
1.3 Thesis organization	3
<b>CHAPTER 2: LITERATURE REVIEW</b>	5
2.1 Introduction	5
2.2 Electrochemical capacitors (EC)	5
2.2.1 Electrical double layer capacitor (EDLC)	8
2.2.2 Redox based electrochemical capacitor	14
2.2.3 Hybrid electrochemical capacitors	18
2.3 Polymer electrolyte	19
2.3.1 Liquid electrolyte	20
2.3.2 Solid polymer electrolyte	22
2.3.2.1 Cellulose based electrolytes	23

2.3.2.2 <i>Gelatin based electrolytes</i>	24
2.3.2.3 <i>Chitosan based electrolytes</i>	25
2.4 Improvement of polymer electrolyte properties	30
2.5 Ionic conductivity characterization	32
2.5.1 <i>Arrhenius model</i>	33
2.5.2 <i>Vogel-Tamman-Fulcher model</i>	34
2.6 Electrical double layer capacitor characterization	37
2.7 Summary	40
<b>CHAPTER 3: EXPERIMENTAL METHODS</b>	41
3.1 Introduction	41
3.2 Materials	41
3.3 Sample preparation	42
3.3.1 <i>Chitosan-Oxalic acid system (System I)</i>	42
3.3.2 <i>Flow chart of the experimental methods</i>	43
3.3.3 <i>Chitosan-Oxalic acid-Glycerol system (System II)</i>	44
3.4 Electrical Impedance Spectroscopy (EIS)	45
3.5 Fourier transform infra-red (FTIR) spectroscopy	47
3.6 X-Ray Diffraction (XRD)	49
3.7 Electrochemical window stability study	50
3.8 Electrical double layer capacitor (EDLC)	52
3.8.1 <i>Electrode preparation</i>	52
3.8.2 <i>Electrical double layer capacitor (EDLC) fabrication</i>	52
3.8.3 <i>Cyclic voltammetry (CV)</i>	53
3.8.4 <i>Charge-discharge studies of EDLC</i>	54
3.9 Summary	55

<b>CHAPTER 4: ELECTRICAL IMPEDANCE SPECTROSCOPY (EIS) STUDIES</b>	56
4.1 Introduction	56
4.2 Conductivity Studies on Chitosan–Oxalic acid system (System I)	56
4.2.1 <i>Temperature dependence of conductivity</i>	64
4.2.2 <i>AC conductivity studies on System I</i>	67
4.2.3 <i>Electrical Analyses on System I</i>	71
4.3 Conductivity Studies on Chitosan–Oxalic acid–Glycerol system (System II)	78
4.3.1 <i>Temperature dependence of conductivity for System II</i>	82
4.3.2 <i>AC conductivity studies on System II</i>	85
4.3.3 <i>Electrical Analyses for System II</i>	87
4.4 Summary	91
<b>CHAPTER 5: FOURIER TRANSFORM INFRARED SPECTROSCOPY ANALYSES</b>	92
5.1 Introduction	92
5.2 FTIR Studies for Chitosan- Oxalic acid system (System I)	96
5.2.1 <i>Deconvolution and band fitting of IR absorptions</i>	98
5.3 FTIR Studies for Chitosan-Oxalic acid-Glycerol system (System II)	103
5.4 Summary	105
<b>CHAPTER 6: X-RAY DIFFRACTION ANALYSES</b>	107
6.1 Introduction	107
6.2 XRD study for Chitosan–Oxalic acid system (System I)	109
6.2.1 <i>Deconvolution of XRD patterns for Chitosan–Oxalic acid system (System I)</i>	111
6.3 XRD study for Chitosan–Oxalic acid–Glycerol system (System II)	114
6.3.1 <i>Deconvolution of XRD patterns for Chitosan–Oxalic acid–Glycerol system (System II)</i>	116
6.4 Summary	119

<b>CHAPTER 7: APPLICATION OF PLASTICIZED POLYMER ELECTROLYTE IN ELECTRICAL DOUBLE LAYER CAPACITOR</b>	120
7.1 Introduction	120
7.2 Electrochemical stability of the plasticized electrolyte	122
7.3 Electrochemical study on of electrical double layer capacitor (EDLC)	123
7.3.1 <i>Cyclic voltammetry study</i>	123
7.3.2 <i>Charge-discharge study</i>	126
7.4 Summary	131
<b>CHAPTER 8: DISCUSSION</b>	132
<b>CHAPTER 9: CONCLUSION AND SUGGESTIONS FOR FURTHER WORK</b>	142
<b>REFERENCES</b>	145

## LIST OF FIGURES

Figure	Caption	Page
Figure 2.1 :	Sketch of Ragone plot for various energy and conversion devices. The indicated areas are rough lines (Kötz & Carlen, 2000)	5
Figure 2.2 :	Schematics of an electrochemical double layer and its electrode/electrolyte interface model (Zhang <i>et al.</i> , 2009)	8
Figure 2.3 :	Illustration of an electrochemical double layer capacitor (EDLC) in its charge state (Pandolfo & Hollenkamp, 2006)	9
Figure 2.4 :	Schematic diagram of the pore size network of an activated carbon grain (Simon & Burke, 2008)	12
Figure 2.5 :	Cyclic voltametrics of the fabricated carbon–carbon symmetric supercapacitor using LiClO <sub>4</sub> doped CS/starch blend electrolyte at scan rates. (a) 50 mV s <sup>-1</sup> , (b) 25 mV s <sup>-1</sup> , (c) 20 mV s <sup>-1</sup> , (d) 15 mV s <sup>-1</sup> (e) 10 mV s <sup>-1</sup> , and (f) 5 mV s <sup>-1</sup> (Sudhakar and Selvakumar, 2012)	13
Figure 2.6 :	Cyclic voltamograms of the cells at 10 mV s <sup>-1</sup> (Ramasamy <i>et al.</i> , 2014)	13
Figure 2.7 :	This schematic of cyclic voltammetry for manganese dioxide, MnO <sub>2</sub> <sup>-</sup> electrode cell in mild aqueous electrolyte (0.1 M K <sub>2</sub> SO <sub>4</sub> ). The upper part is related to the oxidation from Mn(III) to Mn(IV) and the lower part refers to the reduction Mn(IV) to Mn(III) (Simon & Gogotsi, 2008)	15
Figure 2.8 :	Charge-discharge profile of Ni(OH) <sub>2</sub> on dense CNT at different discharging current densities (Feng <i>et al.</i> , 2014)	17
Figure 2.9 :	Arrhenius plots of specific conductivity of 1.0 M lithium bis(fluorosulfonyl)imide (LiFSI), lithium hexafluorophosphate (LiPF <sub>6</sub> ), lithium bis(trifluoromethane sulfonyl) imide (LiTFSI), lithium perchlorate (LiClO <sub>4</sub> ), and lithium tetrafluoroborate (LiBF <sub>4</sub> ) in a mixture of ethylene carbonate (EC)/ethyl methyl carbonate (EMC) with ratio of 3:7 (v/v) (Han <i>et al.</i> , 2011)	20
Figure 2.10 :	Electrode/electrolyte interfacial resistance of Li/S cells with 1 M trifluoromethanesulfonate (LiCF <sub>3</sub> SO <sub>3</sub> ) in tetra(ethylene glycol) dimethyl ether (TEGDME) electrolyte containing <i>x</i> % of toluene additive. Frequency range: 2 MHz–100 mHz (Choi <i>et al.</i> , 2008)	21
Figure 2.11 :	X-ray diffraction of (a) gelatin with ionic liquid 1-ethyl-3-	24

	methylimidazolium acetate ( $C_2mim$ )(OAc) and (b) gelatin with ionic liquid 1-ethyl-3-methylimidazolium acetate ( $C_2mim$ )(OAc) and fixed amount of 0.1 g europium triflate ( $Eu(CF_3SO_3)_3$ ) (Leones <i>et al.</i> , 2012)	
Figure 2.12 :	Structure of (a) cellulose, (b) chitin, and (c) chitosan (redraw from Shukla <i>et al.</i> , 2013)	25
Figure 2.13 :	Chemical structure of glycerol	30
Figure 2.14 :	Nyquist plots for chitosan acetate-lithium triflate ( $LiCF_3SO_3$ ) containing (a) 0.1 g EC (b) 0.3 g EC. Bulk resistance, $R_b$ is taken at the intersection of the depressed semicircle and the tilted spike (Osman <i>et al.</i> , 2001)	32
Figure 2.15 :	Log ( $\zeta$ ) vs. $1000/T$ plot for the polymer electrolyte film (PVA+15 wt% $LiClO_4$ ) + 15 wt. % 1-ethyl-3-methylimidazolium ethylsulfate (Saroj & Singh, 2012)	33
Figure 2.16 :	Arrhenius plot for PVAc–DMF– $LiClO_4$ of various compositions (Baskaran <i>et al.</i> , 2004)	34
Figure 2.17 :	VTF plots of ionic conductivity for PVAc–DMF– $LiClO_4$ gel polymer electrolytes of various compositions (Baskaran <i>et al.</i> , 2004)	35
Figure 2.18 :	Cyclic voltammograms of carbon aerogel (CA), activated carbon aerogel (ACA), and commercial activated carbon (AC) electrodes at a scan rate of (a) 10 mV/s and (b) 100 mV/s (Kwon <i>et al.</i> , 2014)	37
Figure 2.19 :	Charge–discharge characteristics of two EDLC cells at different current densities of (a) 150, (b) 200, and (c) 300 $\mu A\ cm^{-2}$ (Pandey <i>et al.</i> , 2011)	38
Figure 3.1 :	Flow chart of the experimental methods	42
Figure 3.2 :	Typical Nyquist plot of a membrane (Niya & Hoorfar, 2013)	44
Figure 3.3 :	The FTIR spectra for the prepared samples; plain starch, 1% pure chitosan film and pure glycerol (Liu <i>et al.</i> , 2013)	46
Figure 3.4 :	Deconvolution of $SCN^-$ band from 1990 $cm^{-1}$ to 2103 $cm^{-1}$ wavenumbers for sample with 40 wt. % $NH_4SCN$ (Aziz <i>et al.</i> , 2012)	47
Figure 3.5 :	X-ray patterns for plain starch, pure chitosan and starch-chitosan blend films with different glycerol concentration (Liu <i>et al.</i> , 2013)	48
Figure 3.6 :	XRD pattern of chitosan acetate with deconvoluted peaks (Hassan <i>et al.</i> , 2013)	49
Figure 3.7 :	Linear sweep voltammograms of the single-ion conductor polymer	51

	samples at room temperature (Lian <i>et al.</i> , 2014)	
Figure 3.8 :	The design of electrical double layer capacitor (EDLC)	52
Figure 3.9 :	Cyclic voltammetry (CV) analysis in 1 M H <sub>2</sub> SO <sub>4</sub> aqueous solution (Liu <i>et al.</i> , 2006)	53
Figure 3.10 :	Current 10 mA, current density 694 A kg <sup>-1</sup> of activated carbon. Curves at cycle 915 and 916 (Lewandowski and Olejniczak, 2007)	54
Figure 4.1 :	Chemical structure of oxalic acid.	56
Figure 4.2 :	Resonance structures for oxalic acid ((a) and (c)) along with oxalate ion ((b) and (d)) for its first dissociation reaction (redraw from Solomon & Fryhle, 2004)	59
Figure 4.3 :	Inductive effects in oxalic acid (redraw from Solomon & Fryhle, 2004)	59
Figure 4.4 :	Nyquist plots of samples containing different wt. % of oxalic acid (a) 10 (OA10) (b) 20 (OA20) (c) 30 (OA30) (d) 40 (OA40) and (e) 50 (OA50)	60
Figure 4.5 :	Graph of ionic conductivity of membranes for various OA contents at room temperature (300 K) with error bars	62
Figure 4.6 :	Possible conduction mechanism in chitosan-oxalic acid system	63
Figure 4.7 :	Nyquist plots for OA40 sample at elevated temperatures	65
Figure 4.8 :	Plot of $\log \zeta_{dc}$ vs. $10^3/T$ (K <sup>-1</sup> ) for OA 40 membrane with error bars	65
Figure 4.9 :	Fit to equation (4.10) of the real part of conductivity vs. frequency for (a) sample membranes with different oxalic acid contents at room temperature, 300 K, and (b) sample membrane OA40 at various temperatures (dotted line represent the extrapolation)	68
Figure 4.10 :	Variation of exponent $s$ versus temperature for OA40	70
Figure 4.11 :	The dielectric constant, $\epsilon_r$ for samples with different amount of OA versus $\log f$ at room temperature, 300 K (the inset shows the enlarged plot at high frequencies)	71
Figure 4.12 :	The dielectric constant, $\epsilon_r$ of 40 wt. % OA (OA40) sample versus $\log f$ at various temperatures (the inset shows the enlarged plot at high frequencies)	71
Figure 4.13 :	Oxalic acid dependence of dielectric constant, $\epsilon_r$ and ionic conductivity at room temperature, 300 K	72

Figure 4.14 :	Temperature dependence of dielectric constant, $\epsilon_r$ for OA40 at selected frequencies	73
Figure 4.15 :	Variation of $\tan \delta$ with frequency for samples with different amount of OA at room temperature, 300 K	74
Figure 4.16 :	Variation of $\tan \delta$ with frequency for OA40 sample at elevated temperatures	75
Figure 4.17 :	Log $\eta$ versus weight percentage of oxalic acid	76
Figure 4.18:	Variation of log $\eta$ with temperature for the highest conducting sample OA40 (dotted line depicts that the points lie on a straight line hence obeying Arrhenius expression)	76
Figure 4.19 :	Nyquist plots of samples containing different wt. % of glycerol (a) 10 (OG10), (b) 20 (OAG0), (c) 30 (OG30), (d) 40 (OG40), (e) 50 (OG50) and (f) 60 (OG60)	78
Figure 4.20 :	Graph of ionic conductivity of membranes for various glycerol contents at room temperature (300 K) with error bars	79
Figure 4.21 :	Possible conduction mechanism in chitosan-oxalic acid-glycerol system	81
Figure 4.22 :	Nyquist plot for OG60 sample at various temperatures	82
Figure 4.23 :	Plot of log $\zeta_{dc}$ vs. $10^3/T$ ( $K^{-1}$ ) for OG60 membrane with error bars	82
Figure 4.24 :	Fit to Eq. (4.10) of the real part of conductivity against frequency for (a) sample membranes with different oxalic acid contents at room temperature, 300K, and (b) sample membrane OG60 at various temperatures (dotted line represent the extrapolation)	85
Figure 4.25 :	The dielectric constant, $\epsilon_r$ for samples with different amount of glycerol versus log $f$ at room temperature, 300 K (the inset shows the enlarged plot at high frequencies)	87
Figure 4.26 :	Glycerol dependence of dielectric constant, $\epsilon_r$ and ionic conductivity at room temperature, 300 K	88
Figure 4.27 :	Variation of $\tan \delta$ with frequency for sample with different amount of plasticizer glycerol at room temperature, 300 K	89
Figure 4.28 :	Log $\eta$ versus amount of glycerol (wt. %)	89
Figure 5.1 :	A schematic diagram of Fourier transform infrared (FTIR)	92
Figure 5.2 :	FT-IR spectra of (a) pure chitosan, (b) OA10, (c) OA20, (d) OA30, (e) OA40, (f) OA50, and (g) pure OA	95

Figure 5.3 :	FTIR spectra in the range between 3700 and 3000 $\text{cm}^{-1}$ for (a) pure chitosan, (b) OA10, (c) OA20, (d) OA30, (e) OA40 and (f) OA50.	97
Figure 5.4 :	FTIR spectra in the range between 1800 and 1400 $\text{cm}^{-1}$ for (a) pure chitosan, (b) OA10, (c) OA20, (d) OA30, (e) OA40 and (f) OA50	97
Figure 5.5 :	The scheme of hydrogen bonding occurrence. The Z atom is the electronegative atom such as O, N, & F (Solomon & Fryhle, 2004)	98
Figure 5.6 :	Deconvolution and band-fitting of IR spectra between 3700 and 3000 $\text{cm}^{-1}$ for (a) chitosan, (b) OA10, (c) OA20, (d) OA30, (e) OA40, (f) OA50	99
Figure 5.7 :	Deconvolution and band-fitting of IR spectra between 1800 and 1400 $\text{cm}^{-1}$ for (a) chitosan, (b) OA10, (c) OA20, (d) OA30, (e) OA40, (f) OA50	101
Figure 5.8 :	Variation of peak areas of $\text{NH}_3^+$ and $\text{NH}_2$ as a function of oxalic acid content	102
Figure 5.9 :	FT-IR spectra of (a) OG10, (b) OG20, (c) OG30, (d) OG40, (e) OG50, (f) OG60	103
Figure 6.1 :	A schematic diagram of an x-ray diffractometer	107
Figure 6.2 :	XRD patterns of (a) chitosan (b) OA10 (c) OA20 (d) OA30 (e) OA40 (f) OA50 (g) pure OA (inset)	109
Figure 6.3 :	The deconvolution of XRD patterns of (a) chitosan, (b) OA10, (c) OA20, (d) OA30, (e) OA40, (f) OA50	111
Figure 6.4 :	Chemical structure of chitosan, showing position numbering. The two angles $\Psi$ and $\Phi$ define the chain conformation, and the angle $\chi$ define the O-6 orientation (redraw from Muzzarelli <i>et al.</i> , 2012)	112
Figure 6.5 :	Hydrogen bonds interaction between glycerol and carboxamide group of chitosan (redraw from Domjan <i>et al.</i> , 2009)	114
Figure 6.6 :	X-ray diffractograms of the plasticized sample membranes (a) OG10 (b) OG20 (c) OG30 (d) OG40 (e) OG50 (f) OG60	115
Figure 6.7 :	The deconvolution of XRD patterns of (a) OG10 (b) OG20 (c) OG30 (d) OG40 (e) OG50 (f) OG60	116
Figure 6.6 :	The possible attraction between carboxylate ions and glycerol based on XRD results	117
Figure 7.1 :	Linear sweep voltammetry (LSV) of the highest conducting	123

plasticized polymer electrolyte OG60

Figure 7.2 :	Cyclic voltammograms for EDLC comprises OG60 as electrolyte	124
Figure 7.3 :	Charge-discharge characteristic for EDLC at fixed current, 1 mA	126
Figure 7.4 :	Charge-discharge profile at different applied current	129
Figure 7.5 :	Charge-discharge profile at applied current (a) 0.1 mA and (b) at 1 mA. The continuous line (–) depicts the GCD curve at 1st cycle meanwhile dotted line (--) depicts curve at 10th cycle	130

University of Malaya

## LIST OF TABLES

<b>Table</b>	<b>Caption</b>	<b>Page</b>
Table 2.1 :	Comparison of the properties of battery, electrostatic capacitor and EC (Zhang <i>et al.</i> , 2009)	6
Table 2.2 :	Comparison of EDLC and pseudocapacitor (Zhang <i>et al.</i> , 2009)	16
Table 2.3 :	Some works on chitosan base polymer electrolyte	28
Table 2.4 :	VTF parameters and mechanical properties for poly(vinyl acetamide)-dimethyl formamide-lithium perchlorate (PVAc-DMF-LiClO <sub>4</sub> ) electrolyte compositions (Baskaran <i>et al.</i> , 2004)	36
Table 2.5 :	Typical discharge capacitance of EDLC cells at a current density 200 $\mu\text{A cm}^{-2}$ (taken from Pandey <i>et al.</i> , 2011)	39
Table 3.1 :	Various weight percentages of oxalic acid in chitosan membranes	41
Table 3.2 :	The particular weight percent of glycerol in chitosan-oxalic acid membranes	43
Table 3.3 :	Relationship between the four basic immittance function (MacDonald & Johnson, 2005)	44
Table 4.1 :	Different weight percentage (wt. %) of oxalic acid used to prepare chitosan membranes and the thickness, bulk resistance and ionic conductivity values of all membranes at room temperature (300 K) with efficient area of 3.14 cm	62
Table 4.2 :	Ionic conductivity values of OA40 at various temperatures with area and bulk resistance $R_b$	66
Table 4.3 :	Comparison of parameters obtained from fit of the experimental data to Eq. 8 for (a) sample membranes with different oxalic acid content at room temperature, 300 K and (b) sample membrane OA40 at various temperatures	69
Table 4.4 :	Different weight percentage (wt. %) of glycerol used to prepare chitosan membranes and the thickness, bulk resistance and ionic conductivity values of all membranes at room temperature (300 K) with efficient area of 3.14 cm	80
Table 4.5 :	Ionic conductivity values of OG60 at various temperature with area and bulk resistance $R_b$	83
Table 4.6 :	Comparison of parameters obtained from fit of the experimental	86

data to Eq. 8 for (a) sample membranes with different glycerol content at room temperature, 300 K and (b) sample membrane OG60 at various temperatures

Table 5.1 :	The vibrational modes and wavenumbers for chitosan, oxalic acid and glycerol	94
Table 5.2 :	Deconvolution of IR spectra between 3700 and 3000 $\text{cm}^{-1}$	100
Table 5.3 :	Deconvolution of IR spectra between 1800 and 1400 $\text{cm}^{-1}$	102
Table 6.1 :	Room temperature conductivity value and degree of crystallinity of chitosan and the crosslinked membranes	113
Table 6.2 :	Room temperature conductivity value and degree of crystallinity of chitosan and the crosslinked membranes	118
Table 7.1 :	The specific capacitance, $C_s$ value at respective scan rate	125
Table 7.2 :	The calculated values of potential difference $\Delta V$ , specific capacitance $C_s$ , energy density $E$ , and power density $P$ at different working potential	128
Table 7.3 :	The calculated values of potential difference $\Delta V$ , specific capacitance $C_s$ , energy density $E$ , and power density $P$ at different applied current	129
Table 7.4 :	Parameters of GCD at different cyclic processes	131

## LIST OF JOURNAL & SEMINAR/ CONFERENCES PRESENTATION

### List of published Articles in Journal

1. **Fadzallah, I. A.**, Majid, S. R., Careem, M. A. & Arof, A. K. (2014). Relaxation process in chitosan-oxalic acid solid polymer electrolytes. *Ionics*, 20, 969-975.
2. **Fadzallah, I. A.**, Majid, S. R., Careem, M. A. & Arof, A. K. (2014). A study on ionic interactions in chitosan–oxalic acid polymer electrolyte membranes. *Journal of Membrane Science*, 463, 65-72.

### List of Presentation in Seminar and Conferences

1. **Fadzallah, I. A.**, & Majid, S. R. ‘A study of chitosan crosslinked as membrane for direct methanol fuel cell,’ presented at *Annual Physics Research Colloquium*, 28-29 June 2012, University of Malaya, Kuala Lumpur, Malaysia.
2. **Fadzallah, I. A.**, Majid, S. R., & Arof, A. K. ‘Ionic crosslinked chitosan membrane for fuel cell application: Ionic conductivity and electrical properties study. Presented at *8th Mathematical and Physical Sciences Graduate Congress (MPSGC)*, 8-10 Disember 2012, University of Chulalongkorn, Bangkok, Thailand.
3. **Fadzallah, I. A.**, Majid, S. R., & Arof, A. K. ‘Electrochemical studies on chitosan-based membrane,’ presented at *4th International Conference on Functional Materials and Devices (ICFMD)*, 8-11 April 2013, Pulau Pinang, Malaysia.
4. **Fadzallah, I. A.**, Majid, S. R., Careem, M. A., & Arof, A. K. ‘Electrochemical studies on chitosan-based membrane,’ presented at *International Conference on Science & Engineering of Materials International (ICSEM)*, 6-8 January 2014, Greater Noida, India.
5. **Fadzallah, I. A.**, M. A. Careem & Arof, A.K. ‘Electrochemical studies on chitosan-based membrane,’ presented at *International Conference on Materials Science and Technology (ICMST)*, 13-17 October 2014, PUSPIPTEK, Serpong Tangerang, Indonesia.

## LIST OF ABBREVIATIONS

(C <sub>2</sub> mim)(OAc)	1-ethyl-3-methylimidazolium acetate
(C <sub>3</sub> mim)(C <sub>2</sub> SO <sub>4</sub> )	1-ethyl-3-methylimidazolium ethylsulfate
(Ch)(OAc)	Trimethyl-ethanolammonium
(COOH)COO <sup>-</sup>	Oxalate ion
ACA	Activated carbon aerogel
CA	Carbon aerogel
Carot	Carotene
CNT	Carbon nanotube
Co <sub>3</sub> O <sub>4</sub>	Cobalt (II, III) oxide
DMF	Dimethylformamide
EC	Ethylene carbonate
Eu(CF <sub>3</sub> SO <sub>3</sub> ) <sub>3</sub>	Europium (III) trifluoromethanesulfonate
Fe <sub>3</sub> O <sub>4</sub>	Iron (II, III) oxide
Gel	Gelatin
H <sub>2</sub> SO <sub>4</sub>	Sulphuric acid
H <sub>3</sub> BO <sub>3</sub>	Boric acid
HEC	Hydroxyethylcellulose
HF	Hydrogen fluoride
IrO <sub>2</sub>	Iridium dioxide
K <sub>2</sub> SO <sub>4</sub>	Potassium sulphate
Li <sub>2</sub> CO <sub>3</sub>	Lithium carbonate
LiBF <sub>4</sub>	Lithium tetrafluoroborate
LiCF <sub>3</sub> SO <sub>3</sub>	Lithium trifluoromethanesulfonate
LiClO <sub>4</sub>	Lithium perchlorate
LiFSi	Lithium bis(fluorosulfonyl) imide
LiPF <sub>6</sub>	Lithium hexafluorophosphate
LiTFSI	Lithium bis(trifluoromethane sulfonyl) imide
MePrPipNTf <sub>2</sub>	N-Methyl-N-propylpiperidinium bis(trifluoromethanesulphonyl)
MnO <sub>2</sub>	Manganese dioxide
NC	Networked cellulose
NH <sub>4</sub> I	Ammonium iodide
NH <sub>4</sub> SCN	Ammonium thiocyanate
Ni(OH) <sub>2</sub>	Nickel (II) hydroxide
NMP	<i>N</i> -methyl-2-pyrrolidone
PC	Propylene carbonate
PEG	Poly(ethylene glycol)
PEO	Poly(ethylene oxide)
PVA	Poly(vinyl alcohol)
PVAc	Poly(vinyl acetate)
PVFM	Poly(vinyl formal)
PVP	Poly(vinyl pyrrolidone)
RuO <sub>2</sub>	Ruthenium dioxide
TEGDME	Tetraethylene glycol dimethyl ether

# CHAPTER 1

## INTRODUCTION

### 1.1 Research background

One of the greatest challenges in the 21<sup>st</sup> century is unquestionably energy storage and conversion. As the concern over fossil fuel depletion and global warming increases, the world needs to seek for renewable energy sources in order to sustain energy requirement. Methods for storing electricity and retrieving when it is needed will also have to be improved (Ma *et al.*, 2014). The increased use of portable electronic equipment such as mobile telephones and laptops and to encourage the use of electric vehicles have generated the search for alternative and renewable energy sources such as batteries, fuel cells and capacitors (Pernaut & Goulart, 1995; Hashmi & Upadhyaya, 2002; Emmenegger *et al.*, 2003; Lavall *et al.*, 2008).

Over the past few years, electrochemical capacitors that store energy in the electric double layer at the electrode/electrolyte interface have ignited significant worldwide research because of the large specific capacitance, rapid charging/discharging rates, high power performance, long cycle life, and environment-friendly features (Nohara *et al.*, 2003; Yu *et al.*, 2012; Ma *et al.*, 2014). Most of the reports on supercapacitors are based on liquid electrolytes (Ingram *et al.*, 2004; Ma *et al.*, 2013). Although liquid electrolytes possess high ionic conductivity they are prone to leakage, corrosion and explosions (Staiti *et al.*, 2002; Lavall *et al.*, 2008). Replacing liquid electrolytes with solid electrolytes in supercapacitors has been explored by many

researchers. Solid electrolytes have several advantages over liquids that include easy handling without spillage of hazardous liquids and thus making it environmentally safe, minimal internal corrosion, simple principle and mode of construction and flexibility in packaging (Sivaraman *et al.*, 2010; Yu *et al.*, 2011).

Various ways have been employed in order to enhance the performance of solid polymer electrolyte such as addition of plasticizers (Masuda *et al.*, 2007; Lee *et al.*, 2010), ceramic fillers (Wen *et al.*, 2003; Shin *et al.*, 2005) and polymer blending (Micheal & Prabakaran 2004; Venkatesan *et al.*, 2014). The low room temperature ionic conductivity of solid polymer-salt complexes is likely due to their high crystalline fraction and is the main drawback for technological applications. Plasticization has proved to be an effective way to enhance conductivity of solid polymer electrolytes (Qian *et al.*, 2002). Plasticization will make the polymer electrolyte more amorphous and will assist in the dissociation of the salt thereby increasing the number of mobile charge carriers (Pradhan *et al.*, 2007; Pandey *et al.*, 2013).

## **1.2 Scope and objectives of the research**

In this work, chitosan based solid polymer electrolyte will be prepared with the addition of oxalic acid as the proton source and glycerol as the plasticizer. The scope of this research includes incorporating the polymer host (i.e. chitosan) with different concentrations (wt. %) of oxalic acid. The ionic conductivity of the polymer electrolytes is further enhanced by plasticizing the polymer-oxalic acid system with different glycerol concentrations. The electrochemical property such as capacitive behaviour and galvanostatic charge-discharge of the highest conducting plasticized polymer electrolyte

will then be investigated before it is used as an electrolyte in electrical double layer capacitors.

It is therefore obvious that the objectives of the present work are:

- To develop a high conducting solid polymer electrolyte using chitosan as the polymer host.
- To enhance and optimize the ionic conductivity value of the chitosan based polymer electrolyte by plasticization with glycerol.
- To characterize the chitosan based polymer electrolytes using electrochemical impedance spectroscopy (EIS), Fourier transform infrared spectroscopy (FTIR) and x-ray diffraction (XRD).
- To fabricate an electrical double layer capacitor (EDLC) device using the optimized plasticized polymer electrolyte.

### **1.3 Thesis organization**

This thesis is divided into nine chapters. Chapter 1 presents the motivation of the present work and is a brief introduction of the activities of the present investigation. The literature review in Chapter 2 though inexhaustive, provides an overview of different types of electrochemical capacitors, polymer electrolytes, improvement of polymer electrolytes, their properties and application. Chapter 3 describes the experimental methods. Chapter 4 looks at the effect of oxalic acid and glycerol addition to the ionic conductivity and electrical properties of chitosan and chitosan-oxalic acid systems. Chapter 5 discusses further on the interactions between chitosan-oxalic acid and chitosan-oxalic acid-glycerol systems Fourier Transform Infrared (FTIR). The degree of crystallinity for polymer electrolytes is presented in Chapter 6. Chapter 7 reports on the

electrochemical behaviour of the plasticized polymer electrolyte and its application in an electrical double layer capacitor (EDLC). Discussion on the results obtained is divulged in Chapter 8. Chapter 9 concludes the dissertation with some suggestions for further studies.

University of Malaya

# CHAPTER 2

## LITERATURE REVIEW

### 2.1 Introduction

Energy is important for our daily activities since it is needed to power our homes, drive our cars, and even to feed and clothe us. A wide range of technological uses of energy have emerged and developed, so much so that energy availability has become a major issue in society. Wood and hydrocarbon natural fossil fuels, such as coal and crude oil are the easiest way to acquire useful energy. However, climate change and the decreasing availability of fossil fuels require society to move towards sustainable and renewable resources. This has led to an increase in renewable energy production from the sun and wind. Electric vehicles or hybrid electric vehicles with low carbon dioxide emission that require batteries are being developed to help reduce environmental issues. Energy storage systems such as batteries and electrochemical capacitors have started to influence a larger part in our daily activities (Simon & Gogotsi, 2008).

### 2.2 Electrochemical capacitors (EC)

Electrochemical capacitors (EC) have been known for many years and the world witnessed the first patented EC work in 1957 by Becker who described a capacitor based on high surface area carbon. EC has been considered for use in hybrid electric vehicles in a development program initiated in 1989. EC was supposed to boost the

battery or the fuel cell in hybrid electric vehicles by providing the necessary power for acceleration and additionally allow for recuperation of braking energy (Kötz & Carlen, 2000; Burke, 2007). The EC applications are principally boost components supporting batteries or replacing batteries in electric vehicles. Typical energy storage and conversion devices (batteries, capacitors, EC and fuel cells) are presented as a Ragone plot in Figure 1. EC fill in the gap between batteries and the conventional capacitors (Kötz & Carlen, 2000; Simon & Gogotsi, 2008).

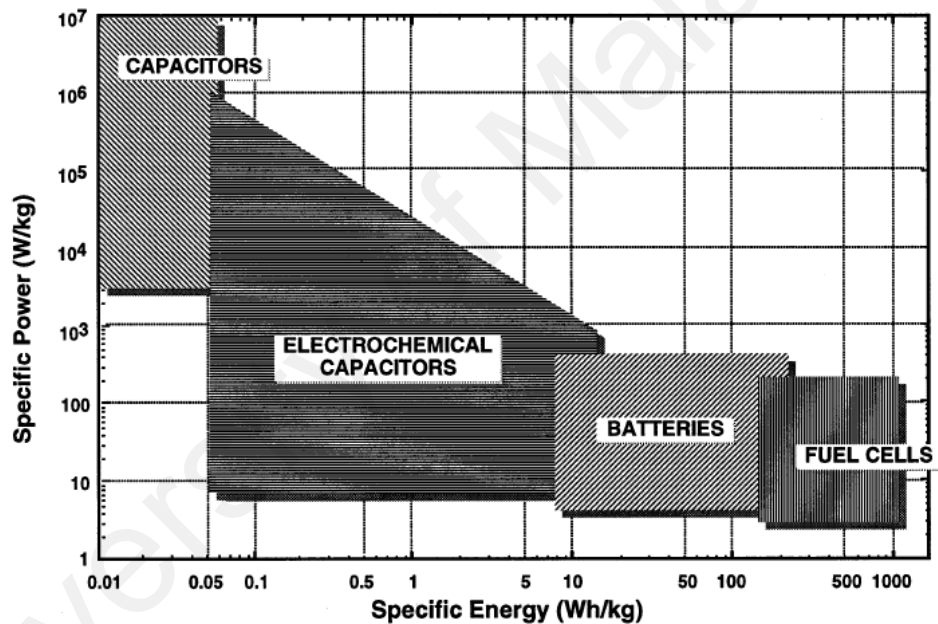


**Figure 2.1:** Sketch of Ragone plot for various energy and conversion devices. The indicated areas are rough lines (Kötz & Carlen, 2000).

EC and high power batteries are significantly different in terms of both design and performance. EC are power devices that can be fully charged or discharged in seconds (60 – 120 s) and their energy density (about 5 W h kg<sup>-1</sup>) is lower than batteries. However, a much higher power delivery or uptake (10 kW kg<sup>-1</sup>) can be achieved for shorter times (few seconds). High power batteries are intended to be charged/discharged in minutes (at least 10 – 15 minutes) rather than in seconds. From Fig. 1, it can be

observed that batteries and low temperature fuel cells are typical low power devices whereas conventional capacitors may have a power density of  $10^6$  watts per  $\text{dm}^3$  but very low energy density. EC has been used to complement or replace batteries in the energy storage field such as for uninterruptible power supplies (back-up supplies used to protect against power disruption) and load levelling (Burke, 2007; Simon & Gogotsi, 2008).

The differences between battery, conventional capacitor (electrostatic capacitor) and EC are listed in Table 2.1 (Zhang *et al.*, 2009). It can be noted that ECs have energy density that is ten times higher than the conventional capacitors. Besides, ECs have high power density, short charge-discharge time, high charge-discharge efficiency and long cycle life. In short, the main advantage of EC as a storage device is that it exhibits short-term pulse that can be useful in hybrid power sources along with the possibility of full discharge and the short-circuit between the two electrodes is also not harmful (Frackowiak & Béguin, 2001).

**Table 2.1:** Comparison of the properties of battery, electrostatic capacitor and EC (Zhang *et al.*, 2009).

	Battery	Electrostatic capacitor	Electrochemical capacitor (EC)
Discharge time	0.3 - 3 h	$10^{-3}$ to $10^{-6}$ s	0.3 - 30 s
Charge time	1 - 5 h	$10^{-3}$ to $10^{-6}$ s	0.3 - 30 s
Energy density ( $\text{W h kg}^{-1}$ )	10-100	<0.1	1-10
Specific power ( $\text{W kg}^{-1}$ )	50 - 200	>10000	$\approx$ 1000
Charge-discharge efficiency	0.7 - 0.85	$\approx$ 1	0.85 - 0.98
Cycle life	500-2000	>500000	>100000

ECs can be classified according to the charge storage mechanism as well as the active materials used. The first type is electrical double layer capacitor (EDLC) which uses high surface area carbon electrodes and the charge storage mechanism arises from the charge separation at the electrode/electrolyte interface (Zhang *et al.*, 2009). Other types of EC are redox based EC and hybrid EC (Yang *et al.*, 2005, Simon & Gogotsi, 2008).

### 2.2.1 Electrical double layer capacitor (EDLC)

EDLC stores charge electrostatically using reversible adsorption of ions of the electrolyte onto the electrochemically stable and have high accessible specific surface area active materials (Simon & Gogotsi, 2008). The double layer capacitance,  $C$  at the electrode/electrolyte interface and can be formulated as:

$$C = \frac{\epsilon_r \epsilon_0 A}{d} \quad (2.1)$$

where  $\epsilon_r$  is the electrolyte dielectric constant,  $\epsilon_0$  is vacuum dielectric constant of,  $A$  is the electrode surface area and  $d$  is the effective thickness of the double layer (charge separation distance). The double layer capacitance is between 5 and 20  $\mu\text{F}$  depending on type of electrolyte used (Simon & Gogotsi, 2008). The electrical charge in EDLC is accumulated in the double layer mainly by electrostatic forces without phase transformations in the electrode materials. The stored electrical energy is based on the separated charged species in an electrical double layer across the electrode/electrolyte interface (Frackowiak & Béguin, 2001). The charge-storage mechanism of this type of EC is predominately due to double-layer (DL) charging effects (Zhang *et al.*, 2009). According to Graham there are three regions of adsorped ions on the electrode surface. The first region or layer is the inner Helmholtz plane (IHP). The second is the outer

Helmholtz plane (OHP) and the third layer is the diffusion layer (see Figure 2.2). The IHP region is made of adsorbed ions (cations or anions in the solid polymer electrolyte) while the OHP region corresponds to the hydrated ion (solvated ion) layer. Subsequently, the diffusion layer develops outside the OHP (Kang *et al.*, 2014 *electrochimica acta*).

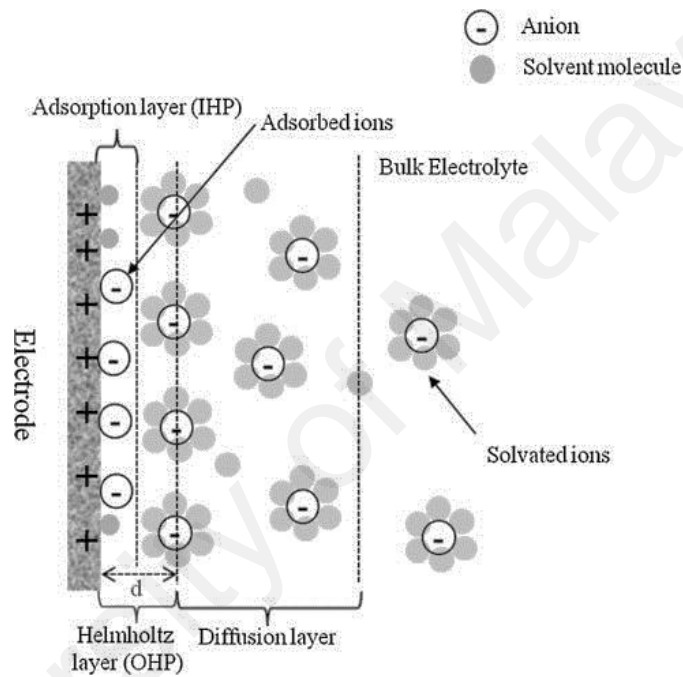


**Figure 2.2:** Schematics of an electrochemical double layer and its electrode/electrolyte interface model (Zhang *et al.*, 2009).

The EDLC is constructed much like a battery, with two electrodes sandwiching the solid polymer electrolyte, with an ion permeable separator located between the electrodes (see Fig. 2.3). Each electrode/electrolyte interface represents a capacitor and the complete cell can be expressed as two capacitors in series. For a symmetrical capacitor (similar electrode materials), the cell capacitance ( $C_{cell}$ ) will be:

$$\frac{1}{C_{cell}} = \frac{1}{C_1} + \frac{1}{C_2} \quad (2.2)$$

where  $C_1$  and  $C_2$  represent the capacitance of the first and second electrodes respectively (Pandolfo & Hollenkamp, 2006). The capacitance in EDLC arises directly analogous to a parallel plate capacitor. As an excess or deficiency of charge builds up on the electrode surface, the counter ions build up in the electrolyte near the electrode/electrolyte interface in order to provide electroneutrality (Zhang *et al.*, 2009).

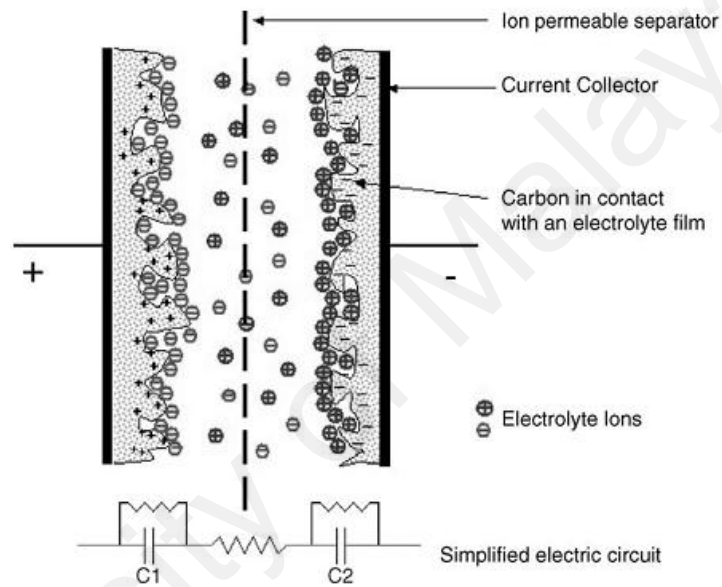


**Figure 2.3:** Illustration of an electrical double layer capacitor (EDLC) in its charge state (Pandolfo & Hollenkamp, 2006).

The energy and power stored in EDLC is calculated using Eq. 2.3 and Eq. 2.4 respectively (Pandolfo & Hollenkamp, 2006):

$$E = \frac{1}{2} CV^2 \quad (2.3)$$

and

$$P = \frac{V^2}{4R} \quad (2.4)$$

where  $C$  is the dc capacitance in Farads,  $V$  the nominal voltage and  $r$  is the equivalent series resistance in ohms. With the voltage is proportionally related to energy and power, an increased in three fold in voltage will increase the order of magnitude in energy,  $E$  as well in power,  $P$ , stored at the same capacitance. This shows that cell voltage is an important determining factor for both energy and power of EDLC. The capacitance of a device is dominantly dependent on the characteristics of the electrode materials.

The electrostatic charge storage in EDLC does not results faradaic (redox) reaction at the electrodes (Simon & Gogotsi, 2008). Hence the electrode must be considered as blocking from the electrical point of view. This is the main difference from batteries since there is no limitation by the electrical kinetics through a polarization resistance. The absence of faradaic reaction eliminates the swelling in the active material that batteries show during charge-discharge cycles. In addition, the solvent of the electrolyte does not take part in the charge storage mechanism, unlike Li-ion batteries where it contributes to the solid/electrolyte interphase when high potential cathodes or graphite anode are used.

The main key to reach high capacitance in EDLC is to use high specific surface area blocking (faradaic reaction does not involved) and electronically conducting electrodes. The preference of using carbon as the electrode material is mainly due to its unique combination of chemical and physical properties (Pandolfo & Hollenkamp, 2006); these are

- high electron conductivity,
- high range of surface area ( $> 2000 \text{ m}^2 \text{ g}^{-1}$ ),
- good corrosion resistance,

- high temperature stability,
- controlled pore structure,
- processability and compatibility in composite materials,
- relatively low cost.

The first two of these properties are critical to the construction of EDLC electrodes. The conductivity of carbon material is influenced by the increasing proportion of conjugated carbon in the  $sp^2$  state during carbonization as electrons associated with  $\pi$ -bonds are delocalized and become available as charge carriers. Hence the electrical conductivity increases as separate conjugated systems also become interconnected to form a conducting network. The conductivity of solid carbon started to increase in the temperature range between 600 and 700 °C that corresponds to the range which carbon loses its acidic functionalities (primarily by formation of H<sub>2</sub>O and CO<sub>2</sub>). Furthermore, the heat treatment increases the conductivity of carbon by alternating the degree of structural disorder, varying from nearly amorphous carbon to the near perfect crystals of graphite which formed at temperatures higher than 2300 °C (Pandolfo & Hollenkamp, 2006).

Activation process is needed in order to increase surface area and porosity from a carbonized organic precursor (known as char) and results in broad group of materials production which referred to as activated carbons (Pandolfo & Hollenkamp, 2006). Chars generally have a relatively low porosity and their structure consists of crystallites with a large number of interstices between them. The interstices tend to be occupied with disorganized carbon residues that block the entrances to the pores. The activation processes open these pores and form additional porosity that can be categorized as thermal activation and chemical activation. The development of porous network in the

bulk of the carbon particles that results in the presence of micropores (smaller than 2 nm), mesopores (between 2 and 50 nm) and macropores (larger than 50 nm) can be seen in Fig. 2.4 (Simon & Burke, 2008). The mobility of ions within the pores is different to the mobility of ions in the bulk of the electrolytic solution, and thus it is greatly influenced by the pore size of the electrode (Sharma & Bhatti, 2010). The pore size is important for easy access of the electrolyte ions into the pores. Small pore size will make the bigger sized ions difficult to pass through disabling the ions to contribute to the double layer capacitance. Hence the pore size must be chosen to suit the electrolyte and thereby ensure that the pore size distribution is optimal based on the size of the ions (Frackowiak & Béguin, 2001; Sharma & Bhatti, 2010).

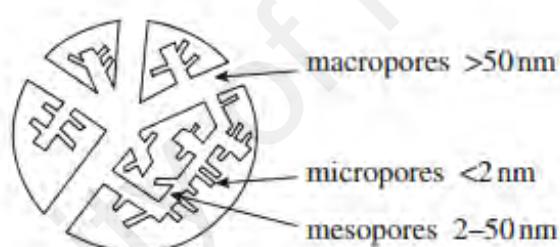


**Figure 2.4:** Schematic diagram of the pore size network of an activated carbon grain (Simon & Burke, 2008).

Sudhakar and Selvakumar (2012) reported an EDLC based on polymer blend of chitosan and starch with lithium perchlorate as dopant and glycerol as plasticizer. In this work the maximum specific capacitance obtained by the highest conducting electrolyte of  $7.7 \times 10^{-4} \text{ S cm}^{-1}$  was  $133 \text{ F g}^{-1}$  at a scan rate of  $10 \text{ mV s}^{-1}$  in which the behaviour observed is comparable to rectangular shape, a characteristic feature of double layer capacitive which can be seen in Fig. 2.5.

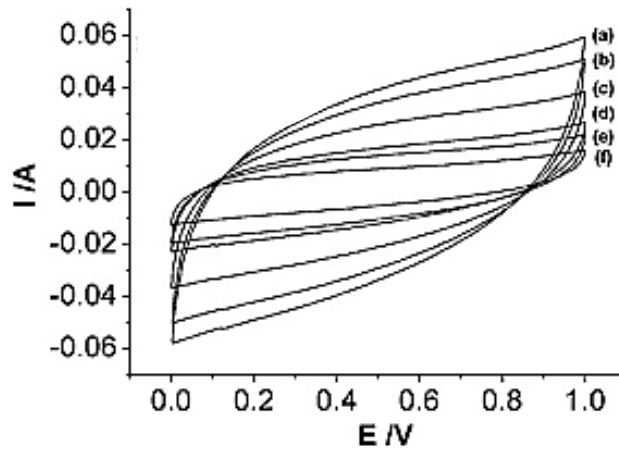


**Figure 2.5:** Cyclic voltammograms of the fabricated carbon-carbon symmetric supercapacitor using  $\text{LiClO}_4$  doped CS/starch blend electrolyte at scan rates. (a)  $50 \text{ mV s}^{-1}$ , (b)  $25 \text{ mV s}^{-1}$ , (c)  $20 \text{ mV s}^{-1}$ , (d)  $15 \text{ mV s}^{-1}$ , (e)  $10 \text{ mV s}^{-1}$ , and (f)  $5 \text{ mV s}^{-1}$  (Sudhakar and Selvakumar, 2012).

Ramasamy and co-workers (2014) fabricated EDLC composed of polyvinylpyrrolidone and sodium sulphate aqueous gel electrolyte with activated carbon electrode. Cyclic voltammetry technique (CV) was used to confirm the cell reversibility (solvated and de-solvated ions), symmetric of ion kinetics (double layer formation). The CVs were carried out at  $22^\circ \text{C}$  in a potential range from 1.5 V to 2.0 V. The cyclic voltammetry of the EDLC at  $10 \text{ mV s}^{-1}$  scan rate results in maximum specific capacitance of  $25.1 \text{ F g}^{-1}$  as shown in Fig. 2.6.

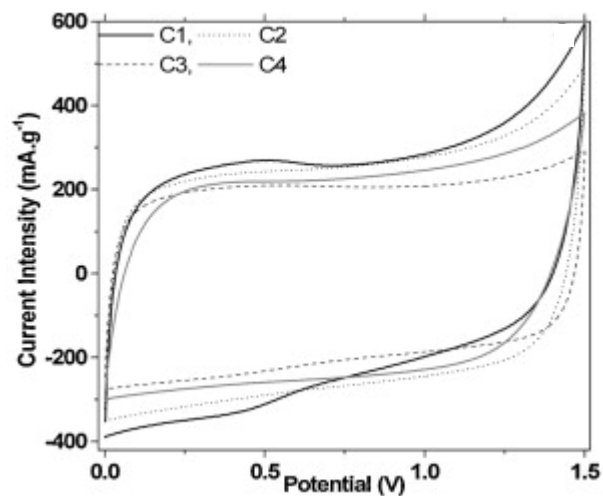


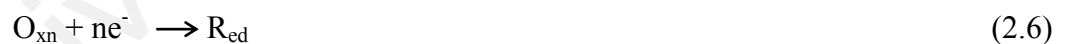
**Figure 2.6:** Cyclic voltammograms of the cells at  $10 \text{ mV s}^{-1}$  (Ramasamy *et al.*, 2014)

### 2.2.2 Redox based electrochemical capacitor

The second type of EC is redox based EC which is also called as pseudocapacitors which arises on electrodes when the application of a potential induces faradaic current from reactions such as electrosorption or from the oxidation-reduction (redox) of electroactive materials. Some examples of the electroactive materials are ruthenium dioxide ( $\text{RuO}_2$ ), iridium dioxide ( $\text{IrO}_2$ ), iron(II,III) oxide ( $\text{Fe}_3\text{O}_4$ ), manganese dioxide ( $\text{MnO}_2$ ), cobalt (II,III) oxide ( $\text{Co}_3\text{O}_4$ ), as well as electronically conducting polymers have been extensively studied (Simon & Gogotsi, 2008; Zhang *et al.*, 2009). The electrosorption process occurs when chemisorption of electron donating anion ( $A^-$ ) such as chloride ( $\text{Cl}^-$ ), bromide ( $\text{Br}^-$ ), iodide ( $\text{I}^-$ ), or thiocyanate ( $\text{CNS}^-$ ) takes place in a process such as:



In Eq. 2.5,  $M$  is the metal ion and  $A$  is anion. Such an electrosorption reaction of  $A^-$  anions at the surface of an electrode, and the quantity  $\delta e^-$  are related to the so called electrosorption valence. Rather than a static separation of charge across a finite distance, an exchange of charge across the double layer results in oxidation-reduction reactions:



where  $\text{O}_{\text{xn}}$  and  $\text{R}_{\text{ed}}$  refer to oxidation and reduction reaction, the charge  $ne^-$  exchanged in this reaction and the energy storage is indirect and analogous to that of a battery (Zhang *et al.*, 2009).

Wen *et al.* (2004) investigated the role of cations of the electrolyte for the pseudocapacitive behavior of metal oxide electrodes  $\text{MnO}_2$ . They reported that capacitances in aprotic solvents were drastically decreased to the smaller values than

that in aqueous neutral solutions. Thus the contribution of the proton to the pseudocapacitive process is not negligible. The charge storage mechanism of  $\text{MnO}_2$  electrode is concluded to involve a fast redox reaction through both potassium ion exchange,  $\text{MnO}_2 + \delta\text{K}^+ + \delta e^- \leftrightarrow \text{MnO}_{2-\delta}(\text{OK})_\delta$  and proton exchange,  $\text{MnO}_2 + \delta\text{H}^+ + \delta e^- \leftrightarrow \text{MnO}_{2-\delta}(\text{OH})_\delta$ . The metal oxide supercapacitors are charged by chemisorption of cation of the electrolyte, proton or the alkaline ion depending on the availability.

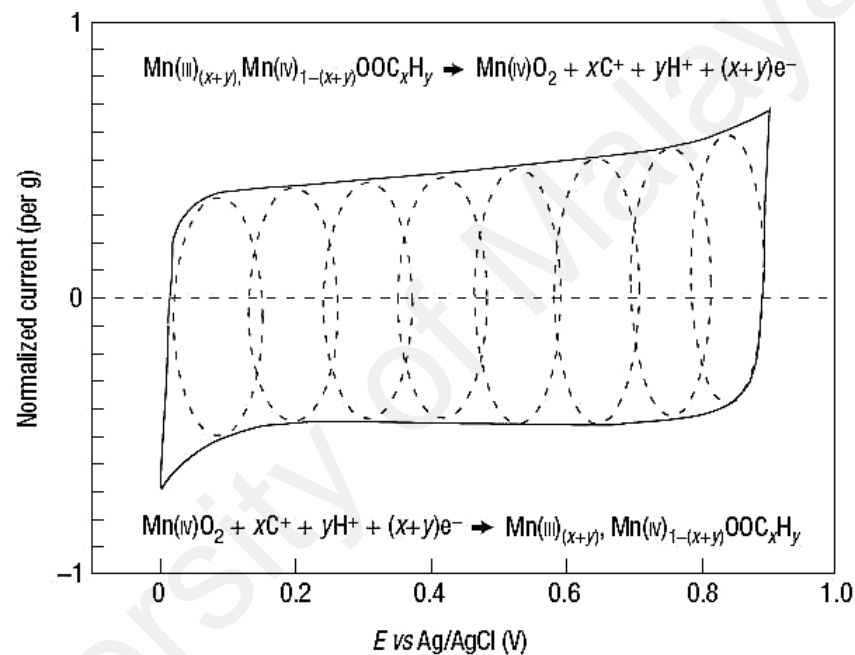


**Figure 2.7:** This schematic of cyclic voltammetry for manganese dioxide,  $\text{MnO}_2$  electrode cell in mild aqueous electrolyte (0.1 M  $\text{K}_2\text{SO}_4$ ). The upper part is related to the oxidation from Mn(III) to Mn(IV) and the lower part refers to the reduction Mn(IV) to Mn(III) (Simon & Gogotsi, 2008).

Since redox reactions are used, pseudocapacitors are similar to batteries, often suffer from a lack of stability during cycling. Fig. 2.7 shows a cyclic voltammetry for electrode cell composed of manganese dioxide,  $\text{MnO}_2$  in mild aqueous electrolyte (0.1 M potassium sulphate,  $\text{K}_2\text{SO}_4$ ) with the successive multiple surface redox reactions leading to the pseudo-capacitive charge storage mechanism (Simon & Gogotsi, 2008). Hence, the differences between EDLC and pseudocapacitor are compared and tabulated in Table 2.2 (Zhang *et al.*, 2009).

**Table 2.2:** Comparison of EDLC and pseudocapacitor (Zhang *et al.*, 2009).

EDLC	Pseudocapacitor
Non-faradaic	Involves faradaic processes
20-50 $\mu\text{F cm}^{-2}$	2000 $\mu\text{F cm}^{-2}$ for single state process, 200 – 500 $\mu\text{F cm}^{-2}$ for multi-state, overlapping processes
Capacitance fairly constant with potential, except through the potential of zero charge	Capacitance fairly constant with potential for ruthenium dioxide ( $\text{RuO}_2$ ); for single-state process, exhibit marked maximum
Highly reversible charging-discharging	Can exhibit several maxima for overlapping, multi-state processes, as for hydrogen, (H) at platinum (Pt); Quite reversible but has intrinsic electrode-kinetic rate limitation
Has restricted voltage range (contrast to conventional capacitor)	Has restricted voltage range
Exhibits mirror-image voltammograms	Exhibits mirror-image voltammograms

Nickel based materials have been intensively investigated and considered as good potential electrode materials for pseudocapacitors due to their high theoretical specific capacity values, high chemical and thermal stability, ready availability, environmentally benign nature and lower cost (Feng *et al.*, 2014). The deposition of conformal  $\text{Ni}(\text{OH})_2$  onto the CVD grown dense carbon nanotube (CNT) bundles on nickel foam results a remarkably high  $C_s$  value of 3300  $\text{F g}^{-1}$  at 1  $\text{mV s}^{-1}$ , and a lower capacity loss at a high charge/discharge current of 10  $\text{A g}^{-1}$  (about 33% of the  $C_s$  value at 2  $\text{A g}^{-1}$ ) as shown in Fig. 2.8.

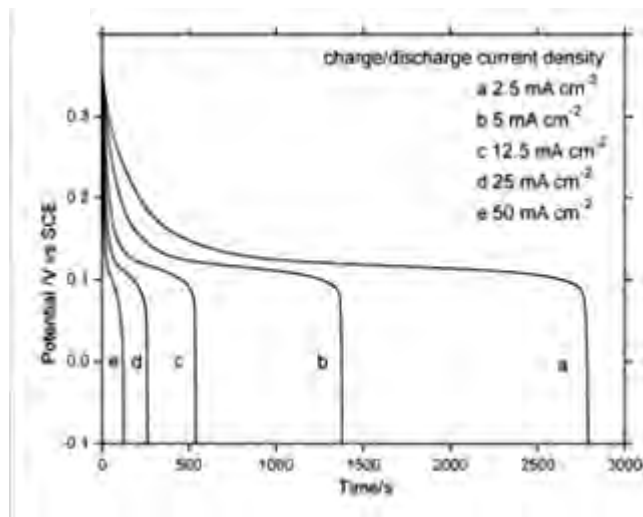


**Figure 2.8:** Charge-discharge profile of Ni(OH)<sub>2</sub> on dense CNT at different discharging current densities (Feng *et al.*, 2014).

### 2.2.3 Hybrid electrochemical capacitors

Hybrid EC offers an attractive alternative to pseudocapacitors and EDLC as in this type of capacitor, the electrodes are composed of an asymmetrical configuration. The electrodes are comprised of a double layer carbon material and a pseudocapacitance material. The pseudocapacitance electrodes accumulate charge through faradic electrochemical process (redox reaction), which can increase the specific capacitance of the capacitor, improve specific energy and power densities, and extend the working voltage. Currently, two different approaches to hybrid EC have emerged:

- (i) pseudo-capacitive metal oxides with a capacitive carbon electrode
- (ii) lithium-insertion electrodes with capacitive carbon electrode.

In this type of EC, the faradaic electrodes led to an increase in the energy density at the cost of cycle-ability (for balanced positive and negative electrode capacities). This is the main drawback of the hybrid EC as compared with EDLC, since it is important to

deflect transforming a good capacitor into a mainstream battery (Simon & Gogotsi, 2008; Zhang *et al.*, 2009).

In this work, electrical double layer capacitor (EDLC) has been chosen as the charge storage device utilizing solid polymer electrolyte which also acts as the separator. Polymer electrolyte will be discussed in Section 2.3, and the ionic conductivity improvement methods will be dealt with in Section 2.4. The characterization of the selected polymer electrolyte will be reviewed in Section 2.5 whereas the characterization of the fabricated EDLC will be further elaborated in Section 2.6.

### **2.3 Polymer electrolyte**

Polymer electrolyte can be defined as any polymer-based structure with significant ionic conductivity. The solid character of polymers is generally related to the molecular weight of the polymer (Sequeira & Santos, 2010). Subsequently the low molecular weight polymers are often liquid which reflects that the polymer character can be in the range from liquids to very hard and rigid materials. Di Noto and co-workers (2011) illustrate polymer electrolytes as macromolecular systems capable of dissolving suitable salts. The salts then will provide the ionic conductivity to the material.

The first proposition was made by Armand in 1979. This proposition has triggered an enormous amount of research worldwide (Sequeira & Santos, 2010; Di Noto *et al.*, 2011). Independent studies have explored the structure – morphology –

conductivity relationship of these materials. These studies concluded that there is a link between the amorphous phase and the ion conductivity. Polymer electrolyte materials will exhibit to a greater or lesser extent the following properties (Sequeira & Santos, 2010):

- adequate ionic conductivity for practical purposes,
- low electronic conductivity,
- good mechanical properties,
- chemical, electrochemical and photochemical stability,
- ease of processing.

Sequeira and Santos (2010) used 'dry' polymer electrolyte term to define a single phase, non-crystalline material containing dissolved salt with the ions of the salt being mobile. Meanwhile, plasticized polymers are referred to polymers that are single phase and contain organic additives which have the effect of softening the polymer. Consequently, these plasticized polymers have higher conductivity compared to 'dry' polymers due to greater freedom for molecular motion. Gel polymer electrolytes are solvent doped and made up of two-phase composition where both anions and cations are mobile at the molecular level (Sequeira & Santos, 2010).

### 2.3.1 *Liquid electrolyte*

A study on physicochemical and electrochemical properties of lithium bis(fluorosulfonyl)imide (LiFSI) and its non-aqueous liquid electrolytes as conducting salt for application in lithium-ion batteries has been done by Han *et al.* (2011). LiFSI was selected because it exhibits far superior stability towards hydrolysis than lithium hexafluorophosphate (LiPF<sub>6</sub>) since it does not release hydrogen fluoride (HF).

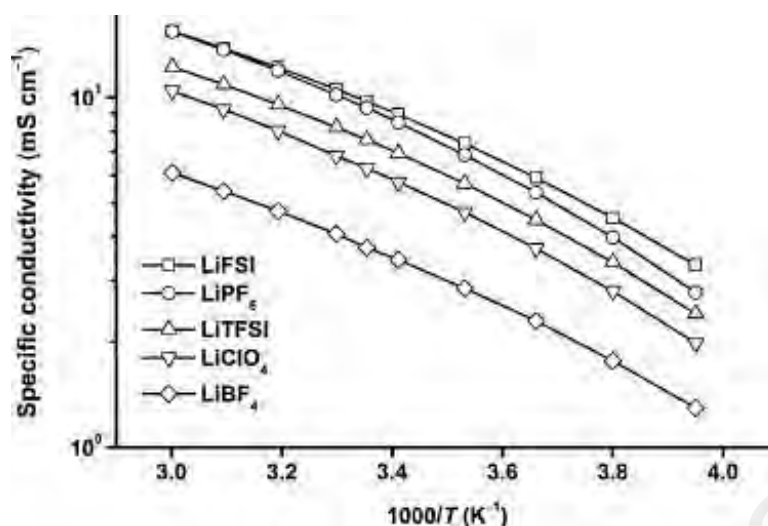


**Figure 2.9:** Arrhenius plots of specific conductivity of 1.0 M lithium bis(fluorosulfonyl)imide (LiFSI), lithium hexafluorophosphate (LiPF<sub>6</sub>), lithium bis(trifluoromethane sulfonyl) imide (LiTFSI), lithium perchlorate (LiClO<sub>4</sub>), and lithium tetrafluoroborate (LiBF<sub>4</sub>) in a mixture of ethylene carbonate (EC)/ethyl methyl carbonate (EMC) with ratio of 3:7 (v/v) (Han *et al.*, 2011).

In addition, LiFSI does not corrode aluminium (Al) due to absence of chloride (Cl<sup>-</sup>) in it. The ionic conductivity study on LiFSI and other salts; lithium hexafluorophosphate (LiPF<sub>6</sub>), lithium bis(trifluoromethane sulfonyl) imide (LiTFSI), lithium perchlorate (LiClO<sub>4</sub>), and lithium tetrafluoroborate (LiBF<sub>4</sub>) was shown in Fig. 2.9. Liquid electrolyte composed of LiFSI exhibits the highest conductivity even at -20 °C.

The toluene effect of adding organic solvent on the impedance properties of sulfur cathode (composed of sulfur, acetylene black and polyvinylidene fluoride (PVdF)) and lithium metal anode in a Li/S cells with liquid electrolytes were studied by Choi *et al.* (2008). The impedance spectra of Li/S cells operated with liquid electrolyte contained lithium trifluoromethanesulfonate (LiCF<sub>3</sub>SO<sub>3</sub>) in tetra(ethylene glycol) dimethyl ether (TEGDME) with different amounts of toluene as additive were evaluated (Fig. 2.10). The bulk resistance of the electrolyte ( $R_b$ ) was measured in the range

between 32 - 56  $\Omega$ . It was stated that electrolytes with toluene have higher redox currents resulting from increased ion mobility and ionic conductivity.

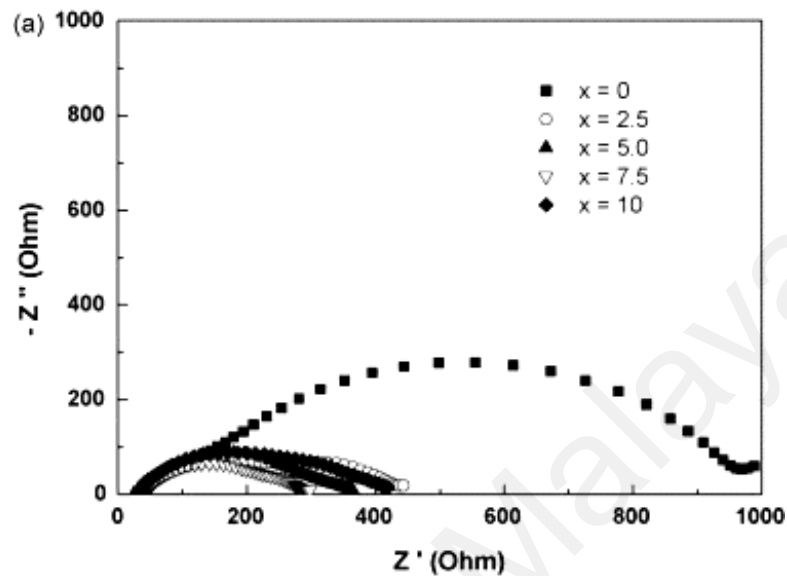


**Figure 2.10:** Electrode/electrolyte interfacial resistance of Li/S cells with 1 M trifluoromethanesulfonate ( $\text{LiCF}_3\text{SO}_3$ ) in tetra(ethylene glycol) dimethyl ether (TEGDME) electrolyte containing  $x\%$  of toluene additive. Frequency range: 2 MHz–100 mHz (Choi *et al.*, 2008).

Even though liquid electrolytes exhibit an attractive prospect in conductivity, it also posed significant safety and environmental concerns since it can cause leakage. In recent years considerable efforts have been devoted to increase the ionic conductivity and improve the mechanical properties of solid polymer electrolyte (SPE) (Leones *et al.*, 2012). Hence, the next section will discuss some examples of SPE and their application in current technologies.

### 2.3.2 Solid polymer electrolyte

The depletion of sources of oil and natural gas has prompted the large interest in polymer based ionic conducting materials such as starch, chitosan, cellulose derivative,

gelatin and natural rubber. These naturally occurring polymers are called biopolymers are able to contribute to the reduction in the emission of industrial gases and generation of greenhouse gases. Besides the use of biopolymers reduces the environmental impact due to the disposal and storage and long-term degradation of synthetic polymers. Biopolymers also show good properties such as biodegradability, low production cost, good physical and chemical properties and good performance as solid polymer electrolyte (SPE). The studies on biopolymers take into consideration the low production cost due to great variety and low prices of raw materials (Pawlicka & Donoso, 2010).

#### 2.3.2.1 Cellulose based electrolytes

Cellulose is the most abundant biopolymer which can be extracted inexpensively from plants, some animals, fungi, algae and bacteria and it is known for its broad modifying capacity and formation of versatile semicrystalline fiber morphologies (Asghar *et al.*, 2012). The structure, morphology and crystallinity of the native cellulose can be modified to enhance its physical and chemical. Cellulose nanocrystals, whiskers and microfibrils have been explored as reinforcements in SPEs and have successfully produced electrolyte material with good mechanical properties (Azizi Samir *et al.*, 2005; Lindman *et al.*, 2010).

Modified cellulose has been synthesized by Machado *et al.* (2005) by reacting cellulose with ethylene oxide to produce hydroxyethylcellulose. The amorphousness of hydroxyethylcellulose (HEC) electrolyte with [O]/[Li] of 6 and room temperature conductivity of  $1.07 \times 10^{-5} \text{ S cm}^{-1}$  has been enhanced with glycerol.

Another work on modified cellulose has been done by composing a quaternary system of poly ethylene glycol (PEG) or tetraethylene glycol dimethyl ether (TEGDME) with polyethylene oxide (PEO), networked cellulose (NC) and lithium perchlorate ( $\text{LiClO}_4$ ) as the doping salt (Lalia *et al.*, 2014). In this work, cellulose was dissolved in sulphuric acid and regenerated in ethanol in order to produce a suspension of network cellulose (NC). The highest conductivity of the system was of the order  $10^{-4} \text{ S cm}^{-1}$  at room temperature.

#### 2.3.2.2 Gelatin based electrolytes

Gelatin consists of proteins (85–92%), mineral salts and water and originated from pig skin, bovine hides, pig and cattle bones and fish (Gomez-Guillén *et al.*, 2009). Gelatin is produced by partial hydrolysis of collagen (Duconseille *et al.*, 2014). Collagen and gelatin do not have exactly the same structure, composition and properties. During the gelatin-making process, proteins are extracted from skin and bone by acid or alkaline baths and thermal pre-treatments. A thermal process is then used to separate proteins from the rest of the raw material.

Leones *et al.* (2012) reported the characteristics of polymer electrolytes using gelatin matrix doped with europium triflate ( $\text{Eu}(\text{CF}_3\text{SO}_3)_3$ ) and different ionic liquids; 1-ethyl-3-methylimidazolium ethylsulfate,  $(\text{C}_2\text{mim})(\text{C}_2\text{SO}_4)$ , 1-ethyl-3-methylimidazolium acetate,  $(\text{C}_2\text{mim})(\text{OAc})$  and trimethyl-ethanolammonium acetate,  $(\text{Ch})(\text{OAc})$ . The maximum conductivity of  $1.18 \times 10^{-4} \text{ S cm}^{-1}$  in this electrolyte system is based on 1-ethyl-3-methylimidazolium acetate,  $(\text{C}_2\text{mim})(\text{OAc})$  at 303 K. Fig. 2.11 shows the x-ray diffraction patterns obtained from the gelatin-based electrolytes at room temperature. The electrolytes were amorphous.

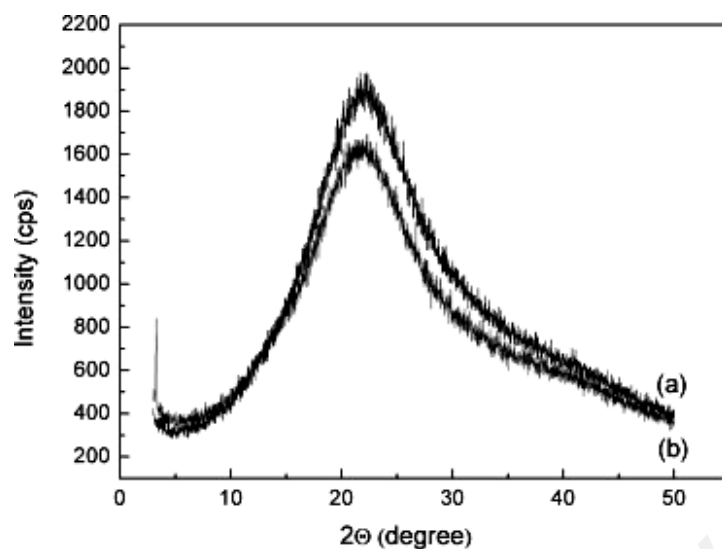


**Figure 2.11:** X-ray diffraction of (a) gelatin with ionic liquid 1-ethyl-3-methylimidazolium acetate ( $C_2mim$ )(OAc) and (b) gelatin with ionic liquid 1-ethyl-3-methylimidazolium acetate ( $C_2mim$ )(OAc) and fixed amount of 0.1 g europium triflate ( $Eu(CF_3SO_3)_3$ ) (Leones *et al.*, 2012).

A series of gelatin/poly (vinyl) alcohol copolymer (Gel/PVA) with different entrapped carotene (Carot) concentration into the films has been investigated. The films were irradiated with gamma rays ( $\gamma$ -rays) at dose levels of 10, 50, 100, 150 and 250 kGy (Lotfy & Fawzy, 2014). The highest conductivity value of  $6.54 \times 10^{-8} \text{ S cm}^{-1}$  was achieved for the Gel/PVA copolymer added with 15 mg/ mL carotene but without gamma radiation. The authors reported that the electrical conductivity of PVA/Gel/Carot films was increased two to three orders of magnitude due to carotene doping, and decreased one order of magnitude on gamma radiation since gamma radiation led to more crosslinking than chain scission causing an increase in the thermal stability of the films and a decrease in the conductivity of the copolymer films.

### 2.3.2.3 Chitosan based electrolytes

Chitosan is the deacetylated product of chitin hydrolysis treatment in alkaline solution as described by Thor and Henderson in 1940 (Muzzarelli, 1978). The chemical

structure of chitosan is similar to cellulose, with linear  $\beta$ -(1 $\rightarrow$ 4) glycosidic linkages combining 2-acetamido-*D*-glucose (*N*-acetyl-*D*-glucosamine) and 2-amino-*D*-glucose (*D*-glucosamine) units as shown in Fig. 2.12 (Shukla *et al.*, 2013). Chitin is found in exoskeletons, peritropic membranes and the cocoons of insects and crustacean animals i.e. crabs and shrimps. It is ubiquitous in fungi and varies in crystallinity and degree of covalent bonding to other wall components i.e. mainly glucans. The solubility of chitin is remarkably poor due to its high degree of crystallinity that can be attributed to hydrogen bonds mainly between O of acetamido (carboxamide) group at C-2 and H of adjacent polymer chain with low chemical reactivity (Muzzarelli, 1978; Ravi Kumar, 2000; Shukla *et al.*, 2013).

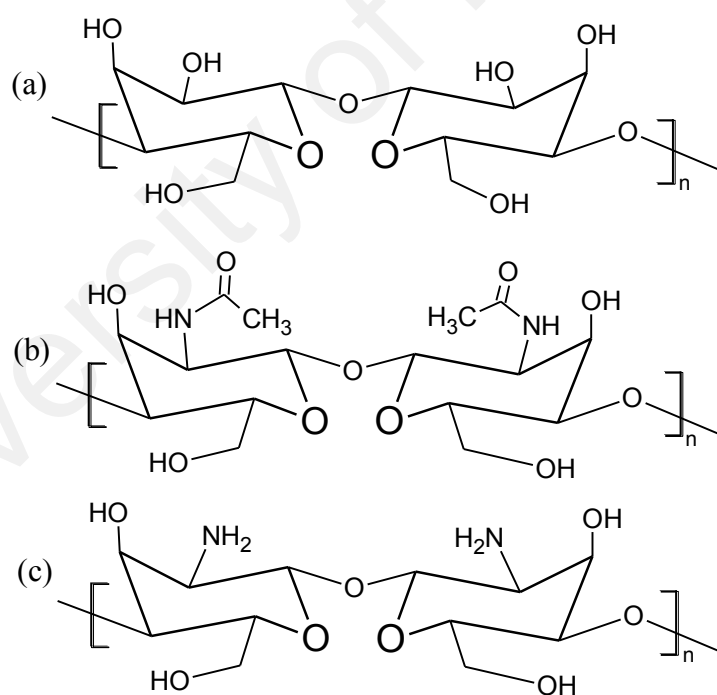


**Figure 2.12:** Structure of (a) cellulose, (b) chitin, and (c) chitosan (redrawn from Shukla *et al.*, 2013).

The main objective in hydrolysis treatment of chitin in alkaline solution is to remove acetate moiety (-NCH<sub>3</sub>CO) from chitin. The alkali removes the protein and deacetylates chitin simultaneously. The processing of crustacean shells mainly involves

the removal of proteins and the dissolution of calcium carbonate which is present in crab shells in high concentrations. In the case of chitosan, the extent of this deacetylation reaction of chitin is determined by the property degree of deacetylation (DD). Hence, the ability of chitosan to dissolve in dilute acids are attributed by DD. The DD is the ratio (usually expressed in percent) of the amount (in moles) of *D*-glucosamine units to the total *D*-glucosamine and *N*-acetyl-*D*-glucosamine units (Dimzon, 2013). For example 70% deacetylated chitosan can be produced by deacetylation process in 40% sodium hydroxide at 120°C for 1–3 hours. (Muzzarelli, 1978; Ravi Kumar, 2000; Shukla *et al.*, 2013). Chitin and chitosan have gained tremendous interest due to their properties as non-toxic, biocompatible and biodegradable polymers.

It is known that chitosan does not have the same degree of hydrogen bonding in as chitin, but chitosan remains insoluble in water and organic solvents due to the abundance of hydroxyl group (Grant *et al.*, 1989). However, the protonation of the amine group in chitosan when treated with dilute organic acid (i.e. acetic, formic, succinic, and lactic acids at pH below 6.5) results in chitosan solubilisation and it has been established that the casting procedure and acid chosen as solvent can affect the crystallinity. Therefore, the applications of chitin and chitosan are limited due to less solubility in water and organic solvent (Mourya & Inamdar, 2008; Sajomsang, 2010).

In order to improve the solubility, physicochemical and biological properties, several chemical modifications of chitosan have been reported. Some examples of modification processes of chitosan are *N*-Acylchitosans, *N*-Carboxyalkyl/(aryl) chitosans and thiolated chitosan (Mourya & Inamdar, 2008). Chitosan and its derivatives have been receiving significant scientific interests have become one of the

hottest topics in recent decades, especially for its food, medical and pharmaceutical applications, including nutrient and drug delivery and tissue engineering (Luo & Wang, 2014).

Grant *et al.* (1989) discussed the importance of chitosan modification by substitution with side chain that can result in structural orientation changes of the chains and solubility of the polymers in water and organic solvents. Chitosan has also been modified by phthaloylation reaction which enabling phthaloyl chitosan solubilization in organic solvents, since the addition of bulky phthaloyl group eliminates hydrogen from the amino group thus preventing hydrogen bonding (Kurita, 2001).

Chitosan is also unique characteristic since it is the only polysaccharide that possesses a high density of positive charges, due to the protonation of amino groups on its backbone when dissolved in acidic medium (Luo & Wang, 2014). The primary amino group of chitosan is partially protonated in weakly acidic aqueous solution and at pH 4.0; the protonation is complete (Il'ina & Varlamov, 2005):



Thus, the molecules of chitosan are present as cationic polyelectrolyte in acidic solution which enables the interactions with negatively charged molecules (anions and polyanions). Polyelectrolyte is defined as a class of macromolecular compound spontaneously acquiring a large number of elementary charges distributed along the molecular chain when dissolved in a suitable polar solvent (Dakhara & Anajwala, 2010). In addition, the polyelectrolyte form of chitosan can interact with polyanions of various nature to form polyelectrolyte complexes which involves electrostatic and dipole-dipole interaction as well as hydrogen and hydrophobic bonds.

The polyelectrolyte complexes do not utilize any chemical covalent cross-linker and are widely used as carriers of drugs, non-viral vectors of transferred gene, biospecific sorbent, films and gels, DNA-binding, enzyme immobilization, tissue engineering and biosensor (Il'ina & Varlamov, 2005; Luo & Wang, 2014). Several examples using chitosan as the polymer host for electrolyte preparation are listed in Table 2.3.

**Table 2.3:** Some works on chitosan based polymer electrolyte.

Polymer electrolytes	Conductivity, $\sigma$ (S cm <sup>-1</sup> )	Reference
Chitosan + 1 % acetic acid + 40 wt. % ammonium nitrate (NH <sub>4</sub> NO <sub>3</sub> ) + 70 wt. % ethylene carbonate (EC)	9.93 x10 <sup>-3</sup>	Ng & Mohamad, 2006
9.1 wt. % chitosan sulphate + 1 % acetic acid	1.4 x10 <sup>-2</sup>	Xiang <i>et al.</i> , 2009
Hexanoyl chitosan + lithium triflate (LiCF <sub>3</sub> SO <sub>3</sub> ) + diethyl carbonate (DEC):ethylene carbonate (EC) 25:75 (wt. %)	4.26 x10 <sup>-5</sup>	Winie <i>et al.</i> , 2009
Chitosan/organophosphorylated titania submicrospheres (immersed in 2 M H <sub>2</sub> SO <sub>4</sub> )	1.14 × 10 <sup>-2</sup>	Wu <i>et al.</i> , 2010
Chitosan/poly(aminopropyltriethoxysilane) + 1 M lithium perchlorate (LiClO <sub>4</sub> ) in molar ratio 0.6:1	5.5 x10 <sup>-6</sup>	Fuentes <i>et al.</i> , 2013
Carboxymethyl chitosan + 3% acetic acid	3.08 x10 <sup>-6</sup>	Mobarak <i>et al.</i> , 2013
Chitosan + 1 % acetic acid + 10 wt. % silver triflate (Ag CF <sub>3</sub> SO <sub>3</sub> )	1.50 x10 <sup>-8</sup>	Aziz & Abidin, 2014

In this work, chitosan has been used as polymer host with oxalic acid, (COOH)<sub>2</sub> as proton donor. Chitosan has very low electrical conductivity due to the hydrogen atoms in the chitosan monomer are being strongly bonded and cannot be mobilized under the action of an electric field (Khiar *et al.*, 2006). To make chitosan a proton conductor, chitosan was dissolved in oxalic acid and the membrane was prepared by solution casting method. The dispersed H<sup>+</sup> and (COOH)COO<sup>-</sup> (oxalate) ions in the

chitosan solvent can be mobilized on application of an electric field. Since the  $H^+$  ions are more mobile than the oxalate ions the membrane becomes a proton conductor. Hence, since the conductivity is increased upon the addition of a proton donor, it should then be possible to produce a more ionically conducting film by increasing the hydrogen donor concentration. Numerous works have been harnessed to produce chitosan based polymer electrolytes as can be seen in Table 2.3.

#### **2.4 Improvement of polymer electrolyte properties**

To enhance the conductivity, several approaches were suggested in the literature, including the use of blend polymers, the addition of a ceramic filler, plasticizer and even radiation. Compared to other methods, plasticization is the simplest, lowest cost and most effective way to improve the conductivity of a SPE. The plasticization of polymer electrolyte has been proven to increase the conductivity values of the electrolyte as reported by Osman *et al.* (2001). In their work, ethylene carbonate (EC) has been added into a chitosan-lithium triflate ( $LiCF_3SO_3$ ) system. They also studied the effect of plasticizer addition on the dielectric constant ( $\epsilon_r$ ) and observed that upon the addition of EC, the dielectric constant of the electrolyte was also increased. This indicates that the plasticizer increased salt dissolution.

Ali *et al.* (2012) reported that propylene carbonate (PC) assisted salt dissociation in chitosan acetate-ammonium iodide ( $NH_4I$ ) electrolyte. This results in increased number of free mobile ions that led to the increase in conductivity. The plasticizer has great influence on the physical and electrical properties of polymer electrolytes and the plasticizer is also able to penetrate into the polymer chains and increase polymer chain

flexibility that can result in improved ionic conductivity. The crystallinity of the electrolyte was also further reduced with addition of the plasticizer.

The effectiveness of glycerol in biodegradable blend films of chitosan/starch is most likely due to its small size which allows it to be more readily inserted between the polymer chains. This can be seen upon the addition of plasticizer into the polymer blend, the conductivity value increased by four orders of magnitude. The compatibility of glycerol in the polymer blend also resulted in crystallinity reduction (Sudhakar & Selvakumar, 2012).

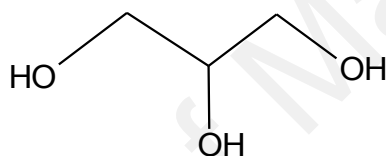


**Figure 2.13:** Chemical structure of glycerol.

In this work, the effect on conductivity of the chitosan based solid polymer electrolyte was studied with glycerol as plasticizer. Glycerol with its chemical structure shown in Fig. 2.13 was selected since it can improve conductivity due to presence of hydroxyl groups (Sudhakar & Selvakumar, 2012). Polyol plasticizers such like sorbitol, glycerol and polyethylene glycol (PEG) are small molecules that able to intersperse and intercalate among and between polymer chains, disrupting hydrogen bonding and spreading the chains apart, which not only increases flexibility, but also water vapor and gas permeabilities (Bourtoom, 2008).

## 2.5 Ionic conductivity characterization

The ionic conductivity of the polymer electrolyte can be obtained from the bulk impedance of the sample that can be determined by using electrochemical impedance spectroscopy (EIS). The ionic conductivity of polymer electrolytes is due to the transport of cations and anions in a polymer matrix (Johansson *et al.*, 1996). It is known that the segmental motion of the polymer host promoted the ionic mobility and, therefore, ionic conductivity is mainly localized to the amorphous phase. The ionic conductivity,  $\sigma$  of polymer electrolytes is given by the product of the concentration of ionic charge carriers and their mobility:

$$\sigma = \sum_i n_i \chi_i q_i \quad (2.8)$$

where  $n_i$  is the number density of ionic charge carriers,  $\chi_i$  is the ionic mobility and  $q_i$  is the ionic charge. The measured impedance of polymer electrolytes usually generated Nyquist plots with a depressed semicircle or a depressed semicircle with a tilted spike (Arof *et al.*, 2014). Nyquist plot of chitosan acetate-lithium triflate with different amounts of plasticizer ethylene carbonate is shown in Fig. 2.14 (Osman *et al.*, 2001). An equivalent circuit composed of a constant phase element (or 'leaky capacitor') in parallel with a resistor.

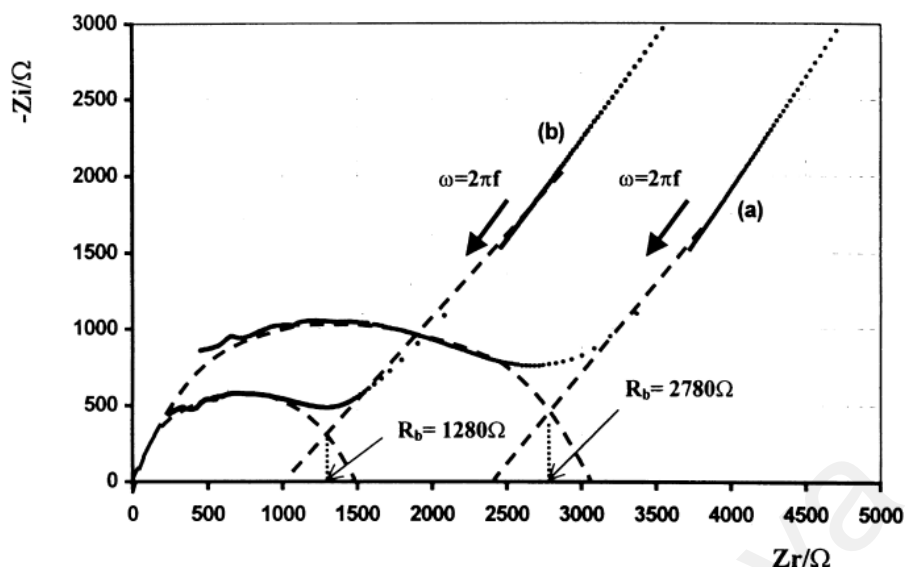


**Figure 2.14:** Nyquist plots for chitosan acetate-lithium triflate ( $\text{LiCF}_3\text{SO}_3$ ) containing (a) 0.1 g EC (b) 0.3 g EC. Bulk resistance,  $R_b$  is taken at the intersection of the depressed semicircle and the tilted spike (Osman *et al.*, 2001).

The ionic conductivity in polymer electrolyte can be enhanced by increasing the temperature. This may be explained due to accelerated hopping into neighboring uncomplexed sites that resulted in increased mobility and hence conductivity or in terms of segmental motion that results in an increase in the free volume of the electrolyte that could assist the motion of ionic charge to hop from one site to another or providing a pathway for ions to move. In addition, the segmental movement of the polymer facilitates the transitional ionic motion (Baskaran *et al.*, 2004; Osman *et al.*, 2001). The ionic conductivity temperature studies can be defined by several models, however only two of them will be discussed in this dissertation:

### 2.5.1 Arrhenius model

If the logarithm of conductivity versus reciprocal of temperature behaves linearly, the relationship is Arrhenian as shown in Fig. 2.15. The Arrhenius model is described by:

$$\sigma = \sigma_0 \exp\left(\frac{-E_A}{k_B T}\right) \quad (2.13)$$

where  $E_A$  is activation energy,  $k_B$  is Boltzmann constant and  $\sigma_0$  is pre-exponential factor. By using the value of the slope and Eq. (2.13), the activation energy,  $E_A$  can be calculated.

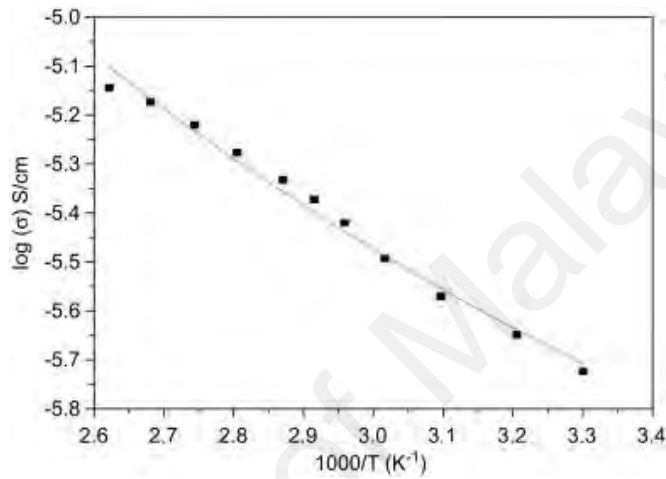


**Figure 2.15:** Log ( $\sigma$ ) vs.  $1000/T$  plot for the polymer electrolyte film (PVA+15 wt% LiClO<sub>4</sub>) + 15 wt. % 1-ethyl-3-methylimidazolium ethylsulfate (Saroj & Singh, 2012).

### 2.5.2 Vogel-Tamman-Fulcher model

The curved  $\log \sigma$  versus  $1000/T$  plots indicates that the ionic conduction obeys the Vogel-Tamman-Fulcher (VTF) relation, which describes the transport properties in a viscous matrix. The VTF relation supports the idea that the ions move through the plasticizer-rich phase and represented by:

$$\sigma = AT^{-1/2} \exp\left[-\frac{E_A}{k_B(T-T_0)}\right] \quad (2.14)$$

where  $A$  is a fitting constant proportional to the number of charge carriers,  $E_A$  is a second fitting constant akin to an activation energy,  $k_B$  is the Boltzmann constant

and  $T_0$  is the equilibrium glass transition temperature at which the “free” volume disappears or at which configuration free entropy becomes zero (i.e., molecular motions cease) (Baskaran *et al.*, 2004).

Baskaran and co-workers (2004) reported the variation of ionic conductivity,  $\sigma$  with reciprocal temperature for poly(vinyl acetate)-lithium perchlorate (PVAc-LiClO<sub>4</sub>) based polymer electrolytes with different amounts of the plasticizer *N,N*-dimethylformamide (DMF) is shown in Fig. 2.16.

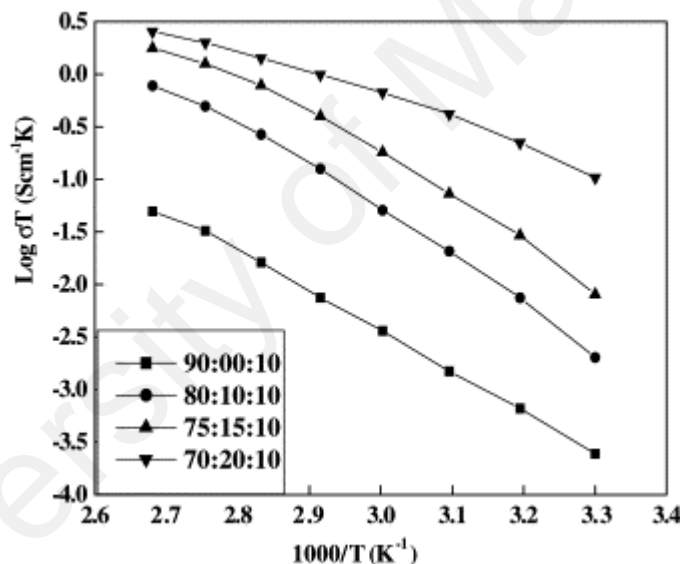


**Figure 2.16:** Arrhenius plot for PVAc-DMF-LiClO<sub>4</sub> of various compositions (Baskaran *et al.*, 2004).

The curve plots have been observed in ionically conducting polymers and have been explained invoking the concept of free volume. Although free volume model was originally adopted for explaining viscoelastic properties of polymers, the reasonably good fit of  $\sigma$  to VTF equation over a wide range of temperature demonstrates the close coupling between the conductivity and the polymer chain segment mobility of the electrolytes.

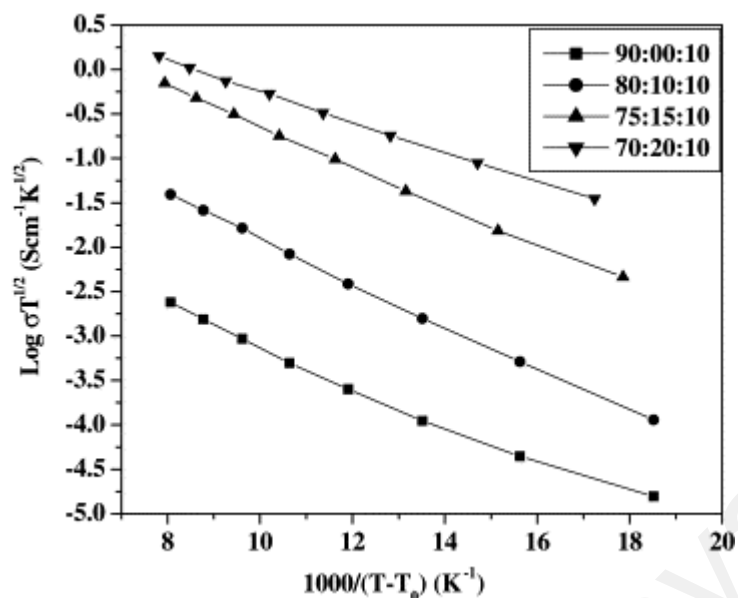


**Figure 2.17:** VTF plots of ionic conductivity for PVAc-DMF-LiClO<sub>4</sub> gel polymer electrolytes of various compositions (Baskaran *et al.*, 2004).

The linear relationship in Fig. 2.17 confirms that the variation in conductivity with temperature follows a VTF relationship. The parameters  $A$  and  $E_A$  determined from the linear plots of  $\ln \sigma T^{1/2}$  versus  $1/(T-T_0)$  are listed in Table 2.4. It is seen that  $A$  values rise significantly with increasing dimethyl formamide (DMF) concentration, which is related to the increase in number of charge carriers. On the other hand,  $E_A$  decreases probably because of a much lower electrolyte viscosity at high plasticizer concentrations which increases the ionic mobility. In PVAc-DMF-LiClO<sub>4</sub> electrolytes, the change in conductivity with temperature has been explained in terms of segmental motion that results in an increase in the free volume of the system that, which also facilitate the mobility of ionic charge. At elevated temperatures, the polymer chains acquire faster internal modes in which bond rotations produce segmental motion. This type of model favours inter-chain and intra-chain ion movements hence, the conductivity of the polymer electrolyte becomes high (Baskaran *et al.*, 2004).

**Table 2.4:** VTF parameters and mechanical properties for poly(vinyl acetamide)-dimethyl formamide-lithium perchlorate (PVAc-DMF-LiClO<sub>4</sub>) electrolyte compositions (Baskaran *et al.*, 2004).

Various PVAc/DMF ratios	A (S cm <sup>-1</sup> K <sup>1/2</sup> )	Activation energy $E_A$ (eV)
90:00:00	0.36	0.049
80:10:00	1.71	0.048
75:15:00	4.29	0.044
70:20:00	4.86	0.033

## 2.6 Electrical double layer capacitor characterization

The performance characteristic on the electrical double layer capacitor (EDLC) can be evaluated by electrical cyclic voltammetry (CV) and galvanostatic charge discharge (GCD) profiles. Cyclic voltammetry (CV) measurements were conducted with an aim of investigating electrochemical properties of carbon materials. Kwon *et al.* (2014) studied the cyclic voltammograms of carbon aerogel (CA), activated carbon aerogel (ACA), and commercial activated carbon (AC) electrodes. As shown in Fig. 2.18(a), CV curves of all carbon materials with a rectangular voltammogram in the voltage range of 0 - 2.5 V at a scan rate of 10 mV/s, indicate the general electrochemical properties of carbon material. Even on increasing scan rate up to 100 mV/s as shown in Fig. 2.18(b), CV curves of carbon aerogel (CA) and activated carbon aerogel (ACA) still maintained the rectangular shape.

The excellent capacitive behaviour of carbon aerogel and activated carbon aerogel at high scan rate implies that their equivalent series resistance (ESR) is very low. However, commercial activated carbon (CA) showed a narrow shaped CV curve, indicating the decrement of specific capacitance. The decrease is thought to be due to

the decrease in capacitance of activated carbon at high scan rate. This is due to its low ion transfer rate in organic electrolyte.

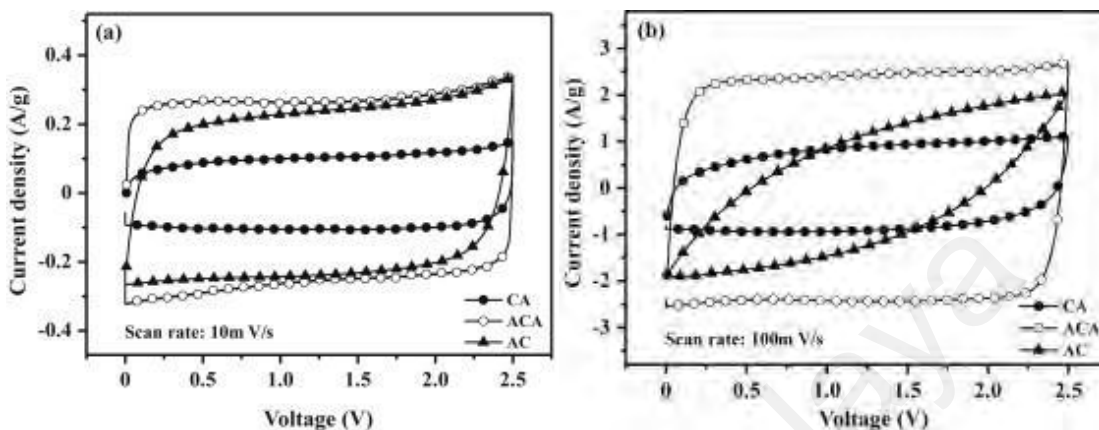


**Figure 2.18:** Cyclic voltammograms of carbon aerogel (CA), activated carbon aerogel (ACA), and commercial activated carbon (AC) electrodes at a scan rate of (a) 10 mV/s and (b) 100 mV/s (Kwon *et al.*, 2014).

Pandey *et al.* (2011) the galvanostatic charge-discharge (GCD) characteristics of the EDLC cells composed of multiwalled carbon nanotube (MWCNT) electrodes and ionic liquid incorporated poly(ethylene oxide) (PEO) based magnesium and lithium ion conducting polymer electrolytes at different current densities. The galvanostatic charge-discharge for EDLC with different types of metal salts have been fabricated as Cell-I and Cell-II can be seen in Fig. 2.19:

Cell-I: MWCNT | PEO<sub>25</sub>·Mg(CF<sub>3</sub>SO<sub>3</sub>)<sub>2</sub> + 40 wt.% EMITf | MWCNT

Cell-II: MWCNT | PEO<sub>25</sub>·LiCF<sub>3</sub>SO<sub>3</sub> + 40 wt.% EMITf | MWCNT

From Fig. 2.19, the discharge characteristics for each current density are almost linear, which confirms the capacitive behavior of both EDLC cells. The initial sudden jump/drop in the voltage while charging and discharging each cell is due to the ohmic loss across the internal resistance ( $R_i$ ), referred as ESR of the cells. The discharge

capacitance ( $C_d$ ) values have been evaluated from the linear part of the discharge characteristics. The values of the capacitance of the EDLC cells at a typical current density of  $200 \mu\text{A cm}^{-2}$  are listed in Table 2.5.

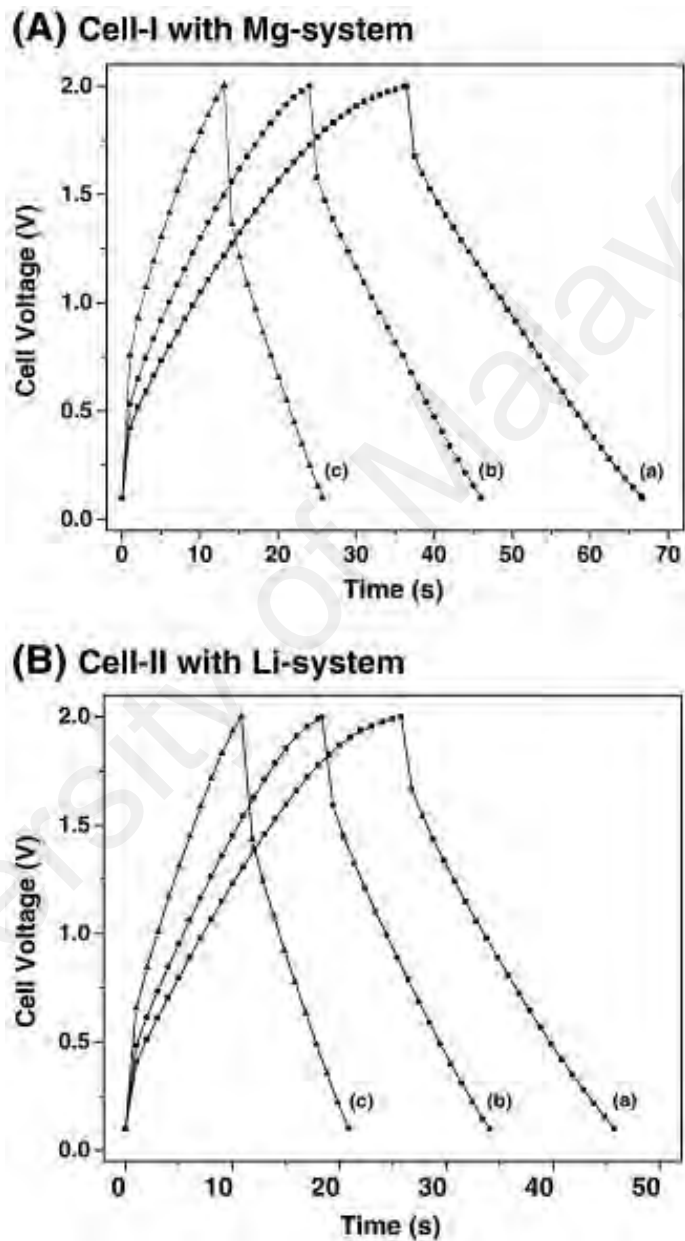


**Figure 2.19:** Charge–discharge characteristics of two EDLC cells at different current densities of (a) 150, (b) 200, and (c)  $300 \mu\text{A cm}^{-2}$  (Pandey *et al.*, 2011).

**Table 2.5:** Typical discharge capacitance of EDLC cells at a current density  $200 \mu\text{A cm}^{-2}$  (Pandey *et al.*, 2011).

	Discharge capacitance, $C_d$ ( $\text{F g}^{-1}$ )
Cell-I (Magnesium based)	2.2
Cell-II (Lithium based)	1.5

## 2.7 Summary

The following points have been emphasized in the literature review:

- The importance of energy has been highlighted as a part our daily life needs and the utilization of electrochemical capacitor as energy storage devices has been greatly elaborated.
- The different nature of electrolytes namely liquid electrolyte and solid polymer electrolyte have been inspected. Some examples of solid polymer electrolyte have been discussed in detail.
- Basic knowledge on the studied materials; chitosan and glycerol in this research has been reviewed along with its electrical properties.
- The characteristics of electrical double layer capacitors have also been discussed in detail.

# CHAPTER 3

## EXPERIMENTAL METHODS

### 3.1 Introduction

Pristine chitosan can dissolve effectively in dilute acidic solutions namely acetic acid, adipic acid, boric acid and salicylic acid compared to chitin. This is due to less hydrogen bonding occurrence between its intra- and inter-polymeric chains (Muzzarelli, 1977). The chitosan based solid polymer electrolytes will be characterized via electrochemical impedance spectroscopy (EIS) to obtain the ionic conductivity and impedance properties of the electrolytes (Huang et al., 2010) and Fourier transform infrared (FTIR) spectroscopy to identify the nature of bonding and different functional groups present in a sample by monitoring the vibrational energy levels of the molecules, which are essentially the fingerprint of different molecules (Rajendran et al., 2007). The crystallinity of the electrolytes will be evaluated using x-ray diffraction (XRD). The optimized electrolyte will be used in the fabrication of electrochemical double layer capacitor (EDLC) and the performance of EDLC will be evaluated.

### 3.2 Materials

Chitosan powder with more than 75 % degree of deacetylation (DD) (and molecular weight,  $M_w$  between 310000 and 375000), oxalic acid and glycerol were purchased from

Aldrich, R&M Chemicals, and Sigma respectively. Oxalic acid was recrystallized in order to eliminate the impurities and kept in drying oven prior to use to minimize the moisture.

The commercial porous carbon (PC) (BET: 2000 m<sup>2</sup>/g) was purchased from Advanced Chemical Supplier (ACS) company. *N*-methyl-2-pyrrolidone (NMP) and poly(vinyl pyrrolidone) (PVP) (M<sub>w</sub> = 40000) were obtained from Aldrich. All materials were obtained commercially.

### **3.3 Sample preparation**

The chitosan based samples in this work was prepared in two stages; namely System I and System II, where chitosan in System I was doped with different percentages of oxalic acid, and in System II, glycerol was added as a plasticizer in the optimized sample in System I to enhance the conductivity of the optimized chitosan – oxalic acid membranes.

#### *3.3.1 Chitosan-oxalic acid system (System I)*

The flow chart of the experimental methods in this work was shown in Fig. 3.1. A specific weight percent of oxalic acid was dissolved into 25 mL of distilled water in a conical flask and the various weight percentages of oxalic acid is as listed in Table 3.1. A fixed amount of chitosan, 0.5 g was then added and the mixtures were stirred overnight at 60 °C in order to ensure complete dissolution of the mixtures. The clear homogeneous solutions were cast in a glass Petri dish and left overnight in a drying oven at 45 °C. The dried membranes were kept in a desiccator for further characterizations.

3.3.2 Flow chart of the experimental methods

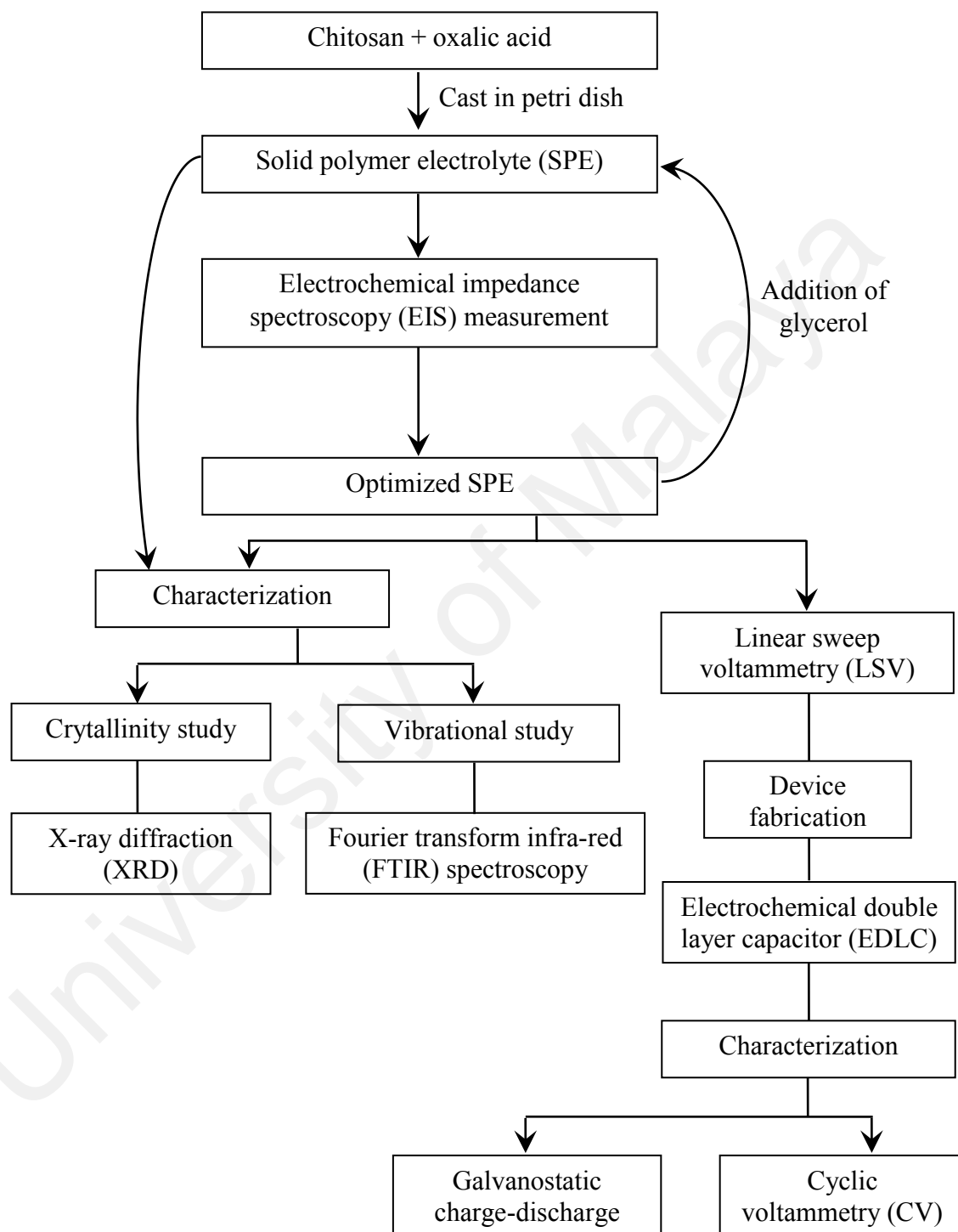


Figure 3.1: Flow chart of the experimental methods.

**Table 3.1:** Various weight percentages of oxalic acid in chitosan membranes.

<b>Oxalic acid (OA) wt. %</b>	<b>Designation</b>
<b>10</b>	OA10
<b>20</b>	OA20
<b>30</b>	OA30
<b>40</b>	OA40
<b>50</b>	OA50

### 3.3.3 Chitosan-oxalic acid-glycerol system (System II)

A fixed amount of oxalic acid (40 wt. % oxalic acid) and chitosan (0.5 g) were dissolved into 25 mL of distilled water in a conical flask. Then various amounts of glycerol as listed in Table 3.2 was added into the solution and the mixtures were stirred overnight at 60 °C in order to ensure complete dissolution of the mixtures. The clear homogeneous solutions were cast in a Petri dish and left overnight in a drying oven at 45 °C. The dried membranes were kept in a desiccator for further characterizations.

**Table 3.2:** The particular weight percent of glycerol in chitosan-oxalic acid membranes.

<b>Glycerol wt. %</b>	<b>Designation</b>
<b>10</b>	OG10
<b>20</b>	OG20
<b>30</b>	OG30
<b>40</b>	OG40
<b>50</b>	OG50
<b>60</b>	OG60

### 3.4 Electrical Impedance Spectroscopy (EIS)

The impedance measurement of the polymer electrolytes was done using HIOKI 3532-01 LCR Hi-Tester interfaced to a computer within the frequency range from 50 Hz to 1M Hz and in the temperature range from 300 to 373 K with 5 K intervals. The sample was clamped between stainless steel blocking electrodes with 2 cm diameter. The electrical conductivity was then calculated using equation:

$$\sigma = \frac{t}{R_b A} \quad (3.1)$$

where  $\zeta$  is the conductivity,  $t$  is the thickness of the electrolyte film,  $A$  is the surface area of contact and  $R_b$  is the bulk electrolyte resistance.  $R_b$  was obtained from the Nyquist plot at the intercept on the real impedance axis. A typical Nyquist plot is shown in Fig. 3.2.

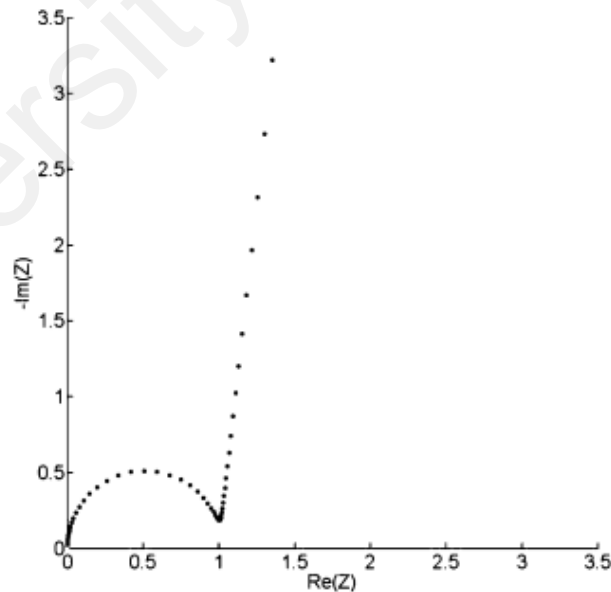


**Figure 3.2:** Typical Nyquist plot of a membrane (Niya & Hoorfar, 2013)

**Table 3.3:** Relationship between the four basic immittance function (MacDonald & Johnson, 2005).

	$M$	$Z$	$A$	$\varepsilon$
$M$	$M$	$\mu Z$	$\mu A^{-1}$	$\varepsilon^{-1}$
$Z$	$\mu^{-1} M$	$Z$	$A^{-1}$	$\mu^{-1} \varepsilon^{-1}$
$A$	$\mu M^{-1}$	$Z^{-1}$	$A$	$\mu \varepsilon$
$\varepsilon$	$M^{-1}$	$\mu^{-1} Z^{-1}$	$\mu^{-1} A$	$\varepsilon$

\* $\mu \equiv j \omega C_c$ , where  $C_c$  is the capacitance of the empty cell.

\*\* $C_c \equiv \varepsilon_0 A_c / l$ , where  $A_c$  is the electrode area,  $\varepsilon_0$  is the dielectric permittivity of free space,  $8.854 \times 10^{-14}$  F cm<sup>-1</sup> and  $l$  is the electrode separation length.

The impedance results can be interpreted in the complex admittance  $A(\omega)$ , complex permittivity  $\varepsilon(\omega)$ , and complex modulus  $M(\omega)$  plots. These four basic response quantities can be denoted by a general term called immittance,  $I(\omega) = I_r + jI_i$ . The relationship between the four basic immittance functions was summarized in Table 3.1. The relationship between dielectric and impedance is given by (Yap *et al.*, 2012):

$$\begin{aligned}
 \varepsilon(\omega) &= \frac{1}{\mu Z(\omega)} \\
 &= \frac{1}{j\omega C_0(Z_r + jZ_i)} \\
 &= \frac{Z_i}{\omega C_0(Z_r^2 + jZ_i^2)} - \frac{jZ_r}{\omega C_0(Z_r^2 + jZ_i^2)}
 \end{aligned} \tag{3.2}$$

Hence, the real ( $\varepsilon_r$ ) and imaginary ( $\varepsilon_i$ ) part of permittivity are:

$$\begin{aligned}
 \varepsilon_r &= \frac{Z_i}{\omega C_0(Z_r^2 + jZ_i^2)} \\
 \varepsilon_i &= \frac{Z_r}{\omega C_0(Z_r^2 + jZ_i^2)}
 \end{aligned} \tag{3.3}$$

The loss tangent, ( $\tan \delta$ ) can be obtained from (Woo *et al.*, 2012):

$$\tan \delta = \frac{\varepsilon_i}{\varepsilon_r} = \frac{Z_r}{Z_i} \quad (3.4)$$

### 3.5 Fourier transform infra-red (FTIR) spectroscopy

Fourier transform infrared (FTIR) data of the materials spans from 4000 to 650  $\text{cm}^{-1}$  using the Thermoscientific Nicolet iS10 operating at a resolution of 4  $\text{cm}^{-1}$ . Each spectrum runs 48 scans in 2 s with correction against the background spectrum of air. FTIR spectroscopy is used to study the interaction between the polymer host and doping elements. The FTIR spectra of chitosan, starch and glycerol is shown in Fig. 3.3 (Liu *et al.*, 2013). The typical region of saccharide bands covers 1180-953  $\text{cm}^{-1}$  which is often considered to comprise vibration modes of C-C and C-O stretching and the bending mode of C-H bonds.

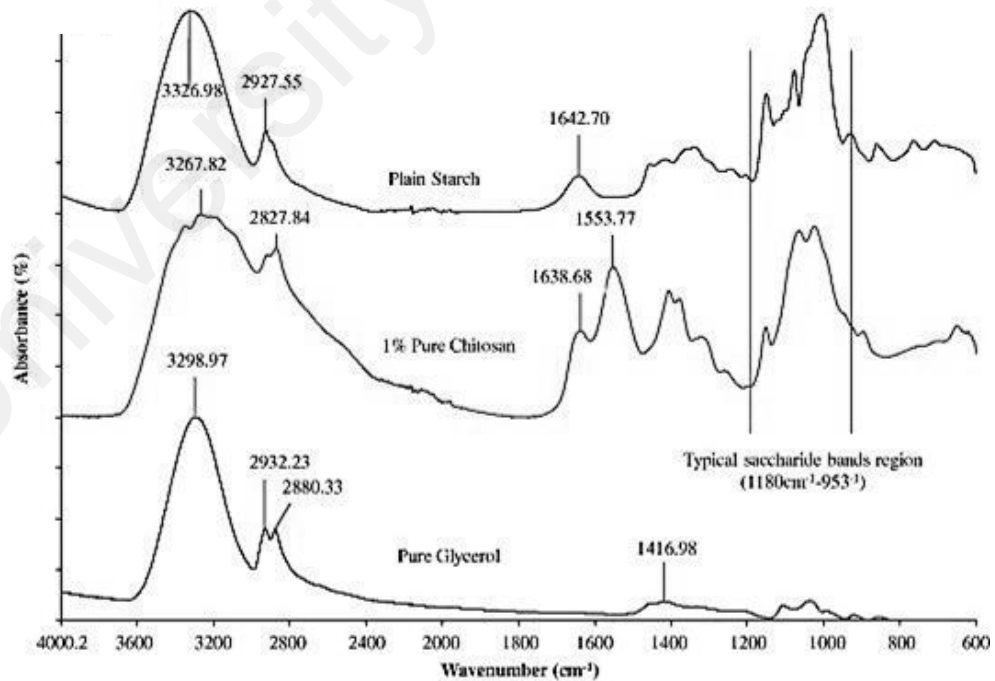


**Figure 3.3:** The FTIR spectra for the prepared samples; plain starch, 1% pure chitosan film and pure glycerol (Liu *et al.*, 2013).

Liu *et al.* (2013) reported four main characteristic absorption bands for pure chitosan film. The first is a broad band ranging from around 3600-3100  $\text{cm}^{-1}$  which is attributed to N-H and OH-O stretching vibration. This band is also, to some extent, contributed by the intermolecular hydrogen bonding of chitosan molecules. Second is the two weak bands located at 2884  $\text{cm}^{-1}$  and 2872  $\text{cm}^{-1}$  are from CH stretching. Third is the amide-I band located around 1640  $\text{cm}^{-1}$ . The deconvolution of selected IR region was made with Gaussian or Lorentzian peaks and the product of deconvolution was fitted to the measured spectra using OMNIC computer software with variation on fixing the line shape, and allowing band parameters such as full width at half maximum (FWHM), area, intensity and band shape to vary without constraints during the iteration (Brooksby & Fawcett, 2001). The deconvolution of  $\text{SCN}^-$  band in the FTIR spectra has been done to quantify ion dissociation and association in the samples containing phthaloylchitosan – 40 wt. %  $\text{NH}_4\text{SCN}$  as shown in Fig 3.4 (Aziz *et al.*, 2012).

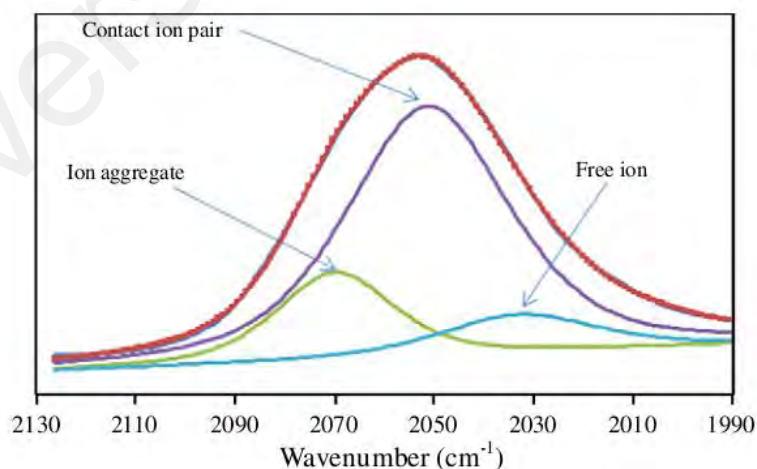


**Figure 3.4:** Deconvolution of  $\text{SCN}^-$  band from 1990  $\text{cm}^{-1}$  to 2103  $\text{cm}^{-1}$  wavenumbers for sample with 40 wt. %  $\text{NH}_4\text{SCN}$  (Aziz *et al.*, 2012).

### 3.6 X-Ray Diffraction (XRD)

X-ray diffraction patterns were recorded on a Bruker model, D8 Advance X-Ray Diffractometer and used a  $Cu-K\alpha$  radiation (wavelength=1.5406 Å) target at 40 kV and 40 mA. Each sample was cut into 2 cm x 1 cm and then placed in the sample holder of the diffractometer. The diffraction angle was varied from 5° to 45° at temperature 25 °C. Typical x-ray patterns of chitosan, starch and chitosan-starch blend films are shown in Fig. 3.5.

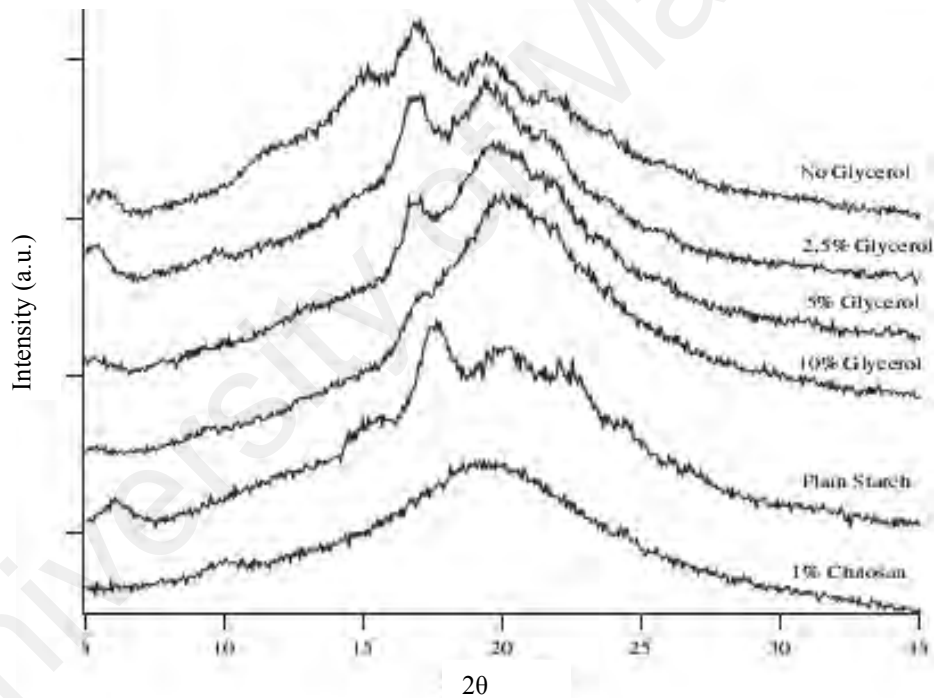


**Figure 3.5:** X-ray patterns for plain starch, pure chitosan and starch-chitosan blend films with different glycerol concentration (Liu *et al.*, 2013).

Figure 3.6 shows XRD pattern and its deconvoluted peaks of chitosan acetate. Two weak crystalline peaks and two halos are observed at  $2\theta$  angles of 11.5°, 22.6° and centre around 23°, 30°, respectively (Hassan *et al.*, 2013).

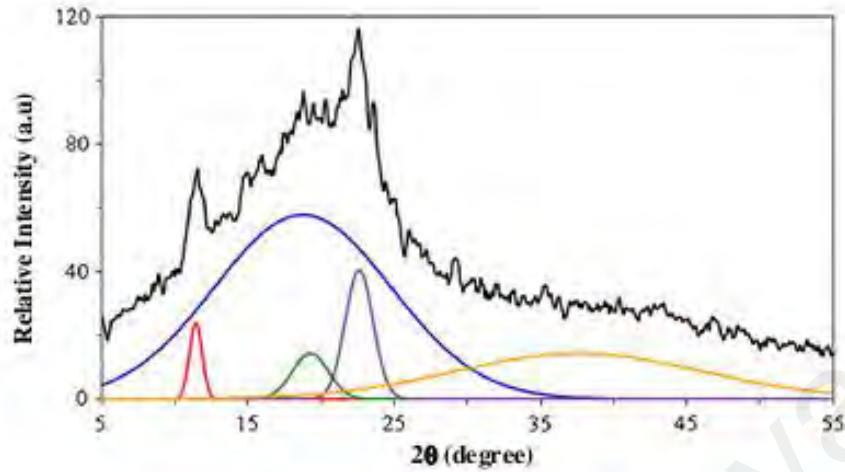


**Figure 3.6:** XRD pattern of chitosan acetate with deconvoluted peaks (Hassan *et al.*, 2013).

The crystalline fractions in the samples were estimated from the ratio of the integrated intensity of peaks associated with crystalline reflections to the total integrated area of the spectrum, i.e.

$$X_c = \frac{I_c}{I_T} \quad (3.5)$$

where  $X_c$  is the crystalline fraction, and  $I_T$  and  $I_c$  are the total and crystalline integrated intensities, respectively.

### 3.7 Electrochemical window stability study

The current-voltage study of the polymer electrolyte has been employed to determine the ability of the polymer electrolyte to withstand the operating voltage of the EDLC system by linear sweep voltammetry (LSV) (Subramania *et al.*, 2006; Saikia *et al.*, 2011). Electrochemical stability with a wide potential range is necessary for

electrochemical devices. The anodic and cathodic voltage response was recorded with an electrochemical working station potentiostat CHI600D. Hence, the LSV measurement was carried out in order to study the decomposition voltage of the electrolyte.

Lian *et al.* (2014) reported the synthesis and unique electrochemical properties of novel oxalate-chelated borate grafted polyvinyl formal based single-ion conductor polymer (SCP) membranes. In their work, poly(vinyl formal) (PVFM) was doped with boric acid ( $\text{H}_3\text{BO}_3$ ), lithium carbonate ( $\text{Li}_2\text{CO}_3$ ), oxalic acid ( $\text{H}_2\text{C}_2\text{O}_4$ ) in fixed ratio of 2.0:1.0:2.0. The molar ratio of -OH in PVFM and B is fixed at 2:0.8, 2:0.9, 2:1.0, 2:1.1 and 2:1.2 to obtain the corresponding single-ion conductor polymer (SCP) samples, which are marked as SCP-0.8, SCP-0.9, SCP-1.0, SCP-1.1 and SCP-1.2, respectively.

Fig. 3.7 shows the voltammogram of samples SCP-0.8, SCP-0.9, SCP-1.0, SCP-1.1 and SCP-1.2. The linear sweep voltammograms (LSV) using Li/GPE/stainless steel cells at room temperature between 2 V and 7 V versus  $\text{Li}/\text{Li}^+$  at a scanning rate of  $5 \text{ mV s}^{-1}$ . No obvious current peak is found through the working electrode from open circuit potential to 5 V all the samples. At applied voltage larger than 5 V, the samples will be oxidized slowly due to the oxidation of plasticizer propylene carbonate (PC). The SCP samples show wide electrochemical stability window, which is accessible to the application in lithium polymer battery for high-voltage lithium ion batteries.

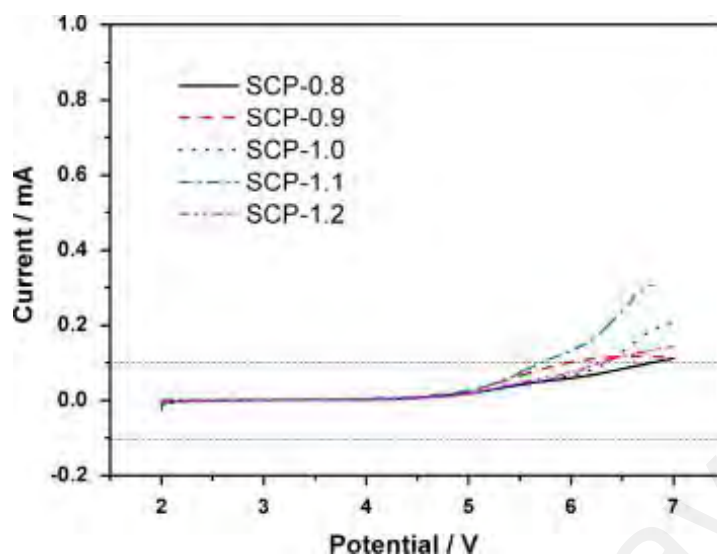


**Figure 3.7:** Linear sweep voltammograms of the single-ion conductor polymer samples at room temperature (Lian *et al.*, 2014).

### 3.8. Electrical double layer capacitor (EDLC)

#### 3.8.1 Electrode preparation

The electrode for EDLC was prepared by mixing porous carbon and poly(vinyl pyrrolidone) (PVP) as binder in ratio 8:1 in 15 mL of *N*-methylpyrrolidone (NMP). The mixture was stirred until homogeneous slurry was obtained. The slurry was then cast onto stainless steel as current collectors using the doctor blade technique and was then left to dry in the drying oven for 4 hours at 45 °C.

#### 3.8.2 Electrical double layer capacitor (EDLC) fabrication

The symmetrical electrode was cut into the size of 1 cm x 1.5 cm and the electrolyte was sandwiched in between the carbon based electrodes as shown in Fig. 3.8.

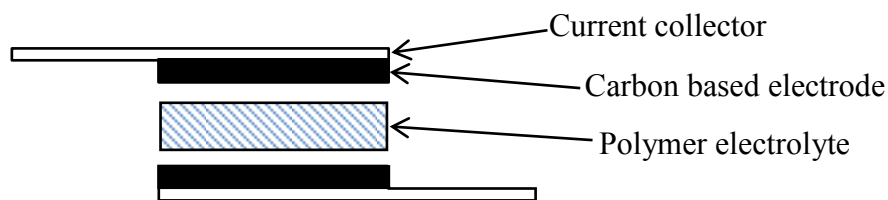


**Figure 3.8:** The design of electrical double layer capacitor (EDLC).

### 3.8.3 Cyclic voltammetry (CV)

Cyclic voltammetry was performed using electrochemical working station potentiostat CHI0006. The performance of EDLC was conducted at scan rate at 1, 3, 5, 7 and 10  $\text{mV s}^{-1}$  between -0.6 to 0.6 V using stainless steel electrodes. Fig. 3.9 shows an example of CV for porous carbon which was prepared by using halloysite (a type of clay mineral) as a template and sucrose as carbon source by means of template method (Liu *et al.*, 2006). CV diagram of EDLC utilizing the porous carbon electrode in 1 M  $\text{H}_2\text{SO}_4$  at different scanning rate in Fig. 3.9 showed almost rectangular curves. When the scanning rate was increased from 20 to 200  $\text{mV s}^{-1}$  the similar shape of the CV curves indicated that the porous carbon possessed good electrochemical stability.

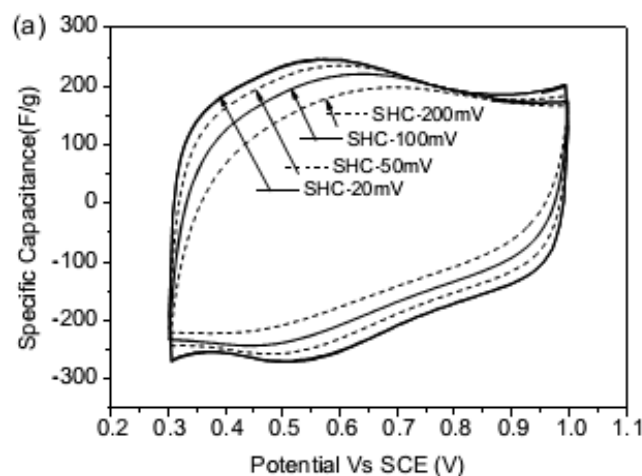


**Figure 3.9:** Cyclic voltammetry (CV) analysis in 1 M  $\text{H}_2\text{SO}_4$  aqueous solution (Liu *et al.*, 2006).

### 3.8.4 Charge-discharge studies of EDLC

The galvanostatic charge-discharge (GCD) characterization of EDLC was carried out to study the effect of current density on EDLC performance using Neware battery cycler. In this work, two tests on the performance of EDLC was investigated firstly by varying several voltage limits at fixed current; and another test was done by fixing the voltage limits while varying the current. Lewandowski and Olejniczak (2007) reported galvanostatic charge-discharge (GCD) curves of the tested capacitor composed of 7.2 mg of activated carbon (in one electrode) with electrolyte 47.7 wt.% *N*-Methyl-*N*-propylpiperidinium bis(trifluoromethanesulphonyl) imide (MePrPipNTf<sub>2</sub>) + 52.3 wt.% of liquid acetonitrile as shown in in Fig. 3.10.

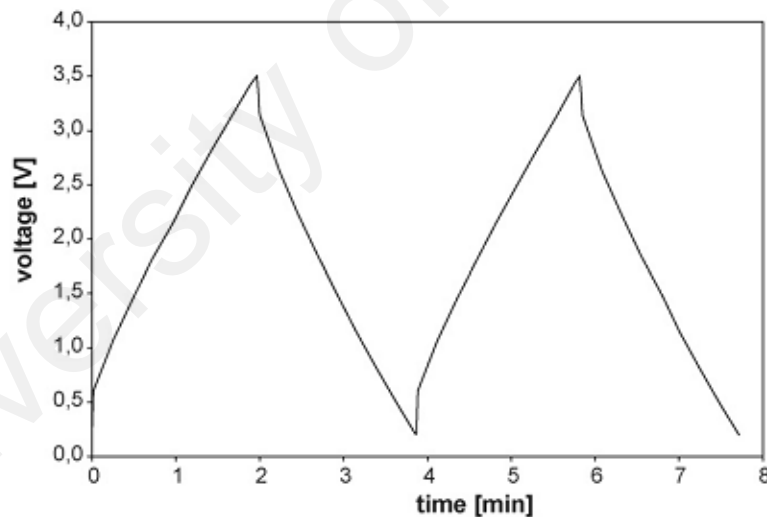


**Figure 3.10:** Current 10 mA, current density 694 A kg<sup>-1</sup> of activated carbon. Curves at cycle 915 and 916 (Lewandowski and Olejniczak, 2007).

The specific capacitance can be calculated from the gradient of the linear portion of the charge and discharge characteristics using equation (Suhaimi *et al.*, 2012):

$$C_s = \frac{i}{m^* \left( \frac{\Delta V}{\Delta t} \right)} \quad (3.6)$$

where  $i$  is the discharge current and  $\Delta V/\Delta t$  is the gradient of the linear curve from discharge curve. In addition, the coulombic efficiency,  $\eta$  can be calculated using equation:

$$\eta = \frac{C_d}{C_c} \times 100 = \frac{t_d}{t_c} \times 100 \quad (3.7)$$

where  $C_d$  and  $C_c$  are the discharge and charge capacitance respectively,  $t_d$  and  $t_c$  represent the time for galvanostatic discharging and charging respectively.

### 3.9 Summary

The experimental method chapter summarizes:

- Preparation methods of chitosan based polymer electrolytes.
- All samples will be characterized using electrochemical impedance spectroscopy (EIS), Fourier transform infrared (FTIR) and x-ray diffraction (XRD).
- The highest conducting electrolyte will be used in the fabrication of electrical double layer capacitor (EDLC). The EDLC preparation and its characterizations have been discussed in details.

## CHAPTER 4

### ELECTRICAL IMPEDANCE SPECTROSCOPY (EIS) STUDIES

#### 4.1 Introduction

Impedance measurement has been used to study the electrochemical systems by applying a small voltage perturbation across the sample (Brett *et al.*, 1993). The small applied voltage is to ensure that the current response is also sinusoidal with the same frequency as the applied voltage but can differ in phase and amplitude from the applied signal. In this chapter, two systems of electrolytes will be prepared namely; System I composed of chitosan–oxalic acid samples whereas System II comprises chitosan–oxalic acid–glycerol samples. The ionic conductivity of the electrolytes will be investigated using electrochemical impedance spectroscopy (EIS) at room and elevated temperatures. The *ac* conduction mechanism of the electrolytes will be studied using Jonscher's universal power law (UPL). The conductivity relaxation time  $\eta$  of the electrolytes can be determined by plotting the dielectric tangent loss ( $\tan \delta$ ) graph.

#### 4.2 Conductivity Studies on Chitosan–Oxalic acid system (System I)

The chemical structure of oxalic acid which has been used in this work is shown in Fig. 4.1. Oxalic acid is a dicarboxylic acid (i.e. two carboxylic acid groups) and named as alkanedioic acids in the International Union of Pure and Applied Chemistry (IUPAC) system (Solomon & Fryhle, 2004). Oxalic acid is a polar substance and can form strong hydrogen bonds with each other and with water which results in appreciable



Thus Eq. 4.2 with respect to Eq. 4.3 and 4.4 can be rewritten as:

$$K_{a1} = \frac{[H_3O^+][COOHCOO^-]}{[COOHCOOH]} \quad (4.5)$$

$$K_{a2} = \frac{[H_3O^+][(2COO^-)]}{[COOHCOOH]} \quad (4.6)$$

where  $K_{a1}$  and  $K_{a2}$  in Eq. 4.5 and 4.6 denote the acidity constant for the first and second dissociation respectively since oxalic acid can undergo dissociation twice due to the presence of two carboxylic acid groups. Since the concentration of the hypothetical acid is the denominator in Eq. 4.5 and 4.6 and the concentrations of the dissociated ions are in the numerator, a large value of  $K_a$  means that the acid is a strong acid and a small value of  $K_a$  means that the acid is weak. The acidity constant is usually expressed as its negative logarithm,  $pK_a$ ;

$$pK_a = -\log K_a \quad (4.7)$$

Since the acidity constant,  $K_a$  is inversely related to  $pK_a$ , the acid will be a strong acid if the  $pK_a$  value is small. If  $K_a$  is greater than 10, the acid will be completely dissociated in water (Solomon & Fryhle, 2004). In addition, the acidity constants of oxalic acid  $pK_{a1}$  and  $pK_{a2}$  are 1.2 and 4.2 respectively which equal  $63.10 \times 10^{-3}$  and  $6.31 \times 10^{-5}$  for  $K_{a1}$  and  $K_{a2}$  respectively. Hence, oxalic acid is a weak acid since the  $K_a$  value is not greater than 10. The acidity strength of oxalic acid can be explained by two effects; namely resonance effects and inductive effects.

The acidity of dicarboxylic acid was attributed primarily to resonance stabilization of the dicarboxylate ions. The principle of resonance theory states that molecules or ions are stabilized by resonance when the molecule or ion can be represented by two or more equivalent resonance structures. Two resonance structures

of oxalic acid ((a) and (c)) and two for its anion ((b) and (d)) can be seen in Fig. 4.2. It can be assumed that resonance stabilization of anion is greater because the resonance structures are equivalent and no separation of opposite charges occurs in them (i.e. the opposite charge separation requires energy). The greater stabilization of oxalate ion lower the free energy of the anion, hence decreases the free-energy change (Gibbs free-energy change) required for the ionization (Solomon & Fryhle, 2004).

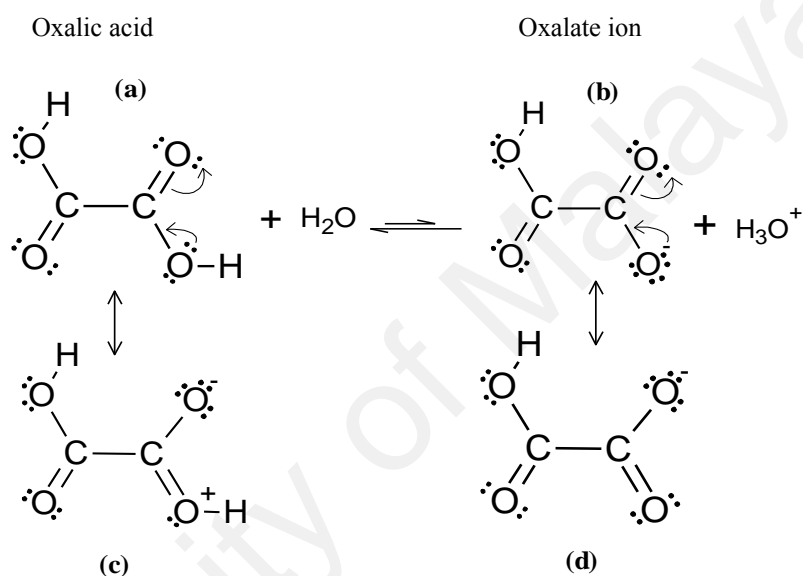


**Figure 4.2:** Resonance structures for oxalic acid ((a) and (c)) along with oxalate ion ((b) and (d)) for its first dissociation reaction (redrawn from Solomon & Fryhle, 2004).

The second effect affecting the acidity in oxalic acid is inductive effects of the carbonyl groups as can be seen in Fig. 4.3. The O–H bond of hydroxyl groups in oxalic acid are highly polarized by the greater electronegativity of the oxygen atoms in the carbonyl group along with their electron-attracting inductive effect. Consequently, the carbon atoms in oxalic acid bear large positive charges ( $\delta^+$ ) which adding the electron-attracting inductive effect to that of the oxygen atoms of the hydroxyl groups attached to them. This combined effects results in greater positive charges on the protons in oxalic acid hence explaining the separation of proton atoms readily. In addition, the inductive

effects of the oxygen atoms of carbonyl groups able to stabilize the oxalate ion by dispersing the negative charges when the protons dissociate (Solomon & Fryhle, 2004).

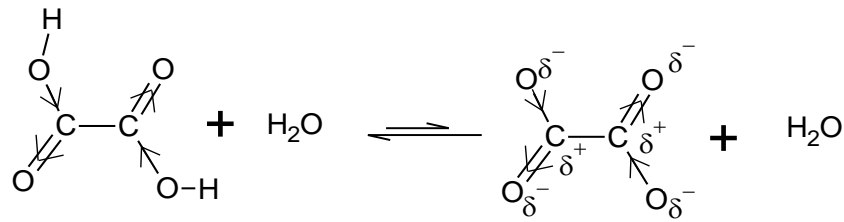
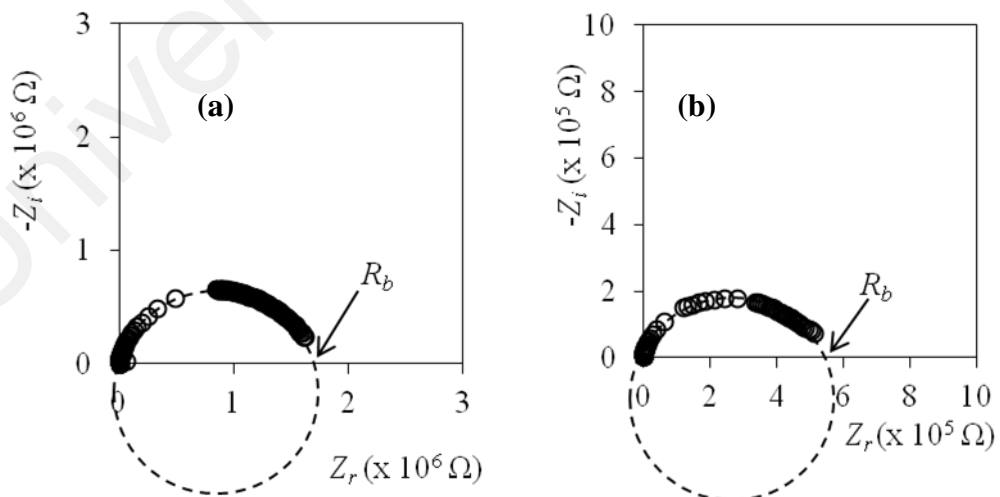


**Figure 4.3:** Inductive effects in oxalic acid (redrawn from Solomon & Fryhle, 2004).

The Nyquist plots in Fig. 4.4 show how the bulk resistance,  $R_b$  of the sample is obtained. The bulk resistance will be used to calculate the ionic conductivity of the electrolyte. The depressed semicircle that occurs at high frequency in the Nyquist plot in Fig. 4.4 is due to the grain-interior of the sample which indicated the presence of bulk effect of the electrolytes and the tilted spike at low frequency results from blocking electrode/electrolyte polarization (Cui *et al.*, 2008).



'Figure 4.4, continued'

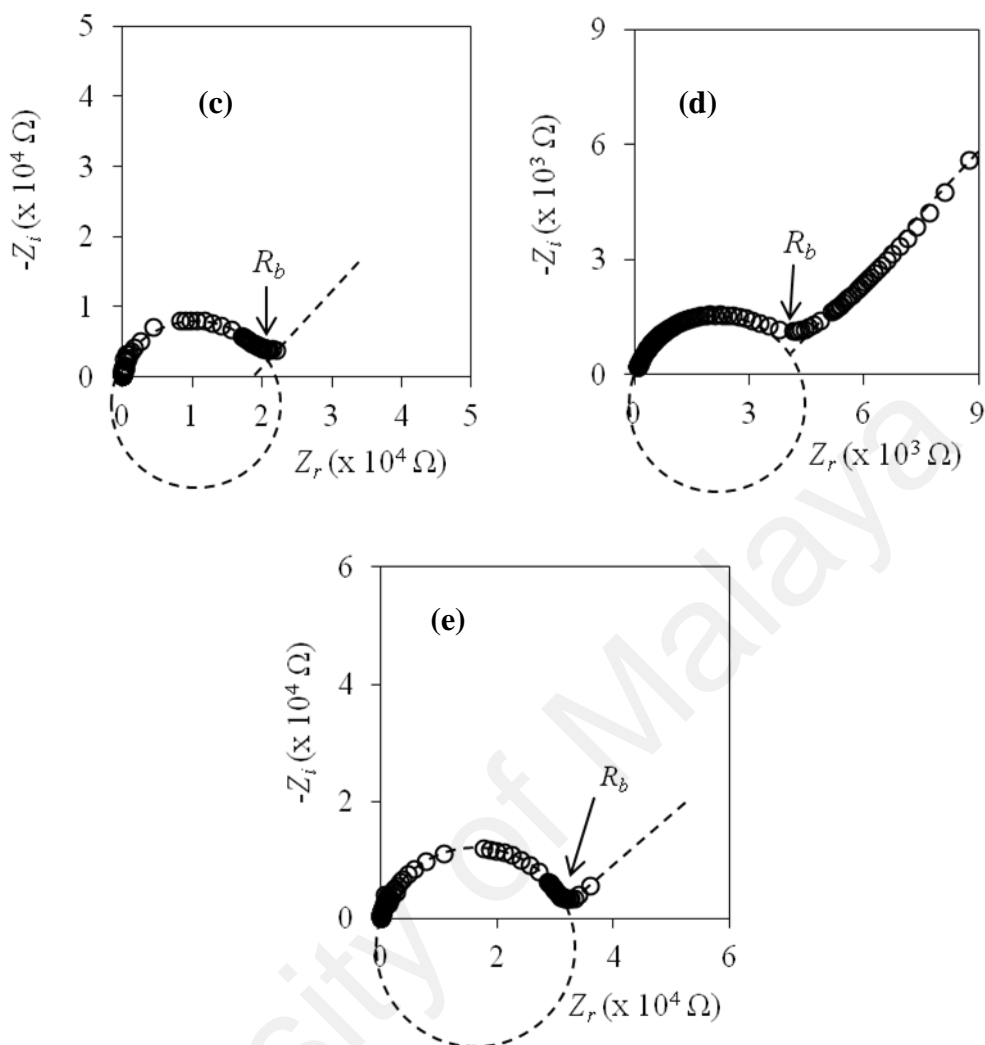


**Figure 4.4:** Nyquist plots of samples containing different wt. % of oxalic acid (a) 10 (OA10) (b) 20 (OA20) (c) 30 (OA30) (d) 40 (OA40) and (e) 50 (OA50).

The ionic conductivity value at room temperature (300 K) from the Nyquist plots in Fig. 4.4 was plotted against oxalic acid content and is shown in Fig. 4.5. It can be observed that the conductivity increased with oxalic acid content and maximizes at 40 wt. %. The enhancement of conductivity with increasing amount of oxalic acid is due to the increasing number of protons. The OA40 membrane has the maximum room temperature conductivity of  $4.95 \times 10^{-7} \text{ S cm}^{-1}$ , which is better than the maximum conductivity value reported for poly(vinylidene fluoride-hexafluoropropyl)-oxalic acid

system (Missan *et al.*, 2006). The ionic conductivity and  $R_b$  values at room temperature for the sample membranes are listed in Table 4.1.

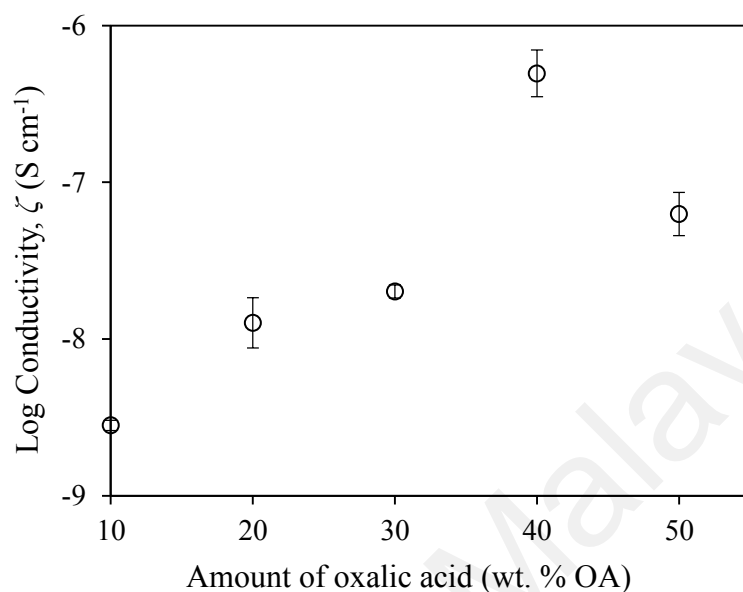


**Figure 4.5:** Graph of ionic conductivity of membranes for various OA contents at room temperature (300 K) with error bars.

**Table 4.1:** Different weight percentage (wt. %) of oxalic acid used to prepare chitosan membranes and the thickness, bulk resistance and ionic conductivity values of all membranes at room temperature (300 K) with efficient area of 3.14 cm.

Oxalic acid (OA) wt. %	Sample designation	Thickness, $t$ (cm)	Bulk resistance, $R_b$ ( $\Omega$ )	Conductivity, $\zeta_{dc}$ (S cm <sup>-1</sup> ) at room temperature
10	OA10	0.02	$1.81 \times 10^6$	$2.81 \times 10^{-9}$
20	OA20	0.02	$5.31 \times 10^5$	$1.27 \times 10^{-8}$
30	OA30	0.01	$2.22 \times 10^5$	$2.01 \times 10^{-8}$
40	OA40	0.01	$4.56 \times 10^3$	$4.95 \times 10^{-7}$
50	OA50	0.01	$3.12 \times 10^4$	$6.26 \times 10^{-8}$

The dissolution of oxalic acid in water produces two moles each of  $H^+$  and  $COO^-$  which help the dissolution of chitosan powder since chitosan needs a slightly acidic medium to dissolve. The re-association of  $H^+$  and  $COO^-$  from oxalic acid to form  $COOH$  might be the reason for the conductivity decrement when the OA content was increased to 50 wt. %. This might be due to the high reactivity property of oxalic acid

since it has a low dissociation constant value,  $pK_a$  (for proton dissociation in OA the  $pK_a$  value is 1.2).

The high amount of  $H^+$  can re-associate with  $COO^-$  ion (oxalate ion) to form oxalic acid again since Eq. (4.3) favours the reaction to proceed to the left hand side due to the incomplete dissociation of weak acid. Oxalic acid is considered to be weak as the calculated value of  $K_a$  is smaller than 10 (Solomon & Fryhle, 2004). This results in the low amount of free  $H^+$ , thus reducing the availability of  $H^+$  for proton conduction in the sample OA50. The conductivity value is optimized at 40 wt. % of OA since OA40 membrane shows the highest conductivity value compared to those of other OA concentrations and this implies that OA40 contains the highest amount of protons for ionic conductivity at room temperature.

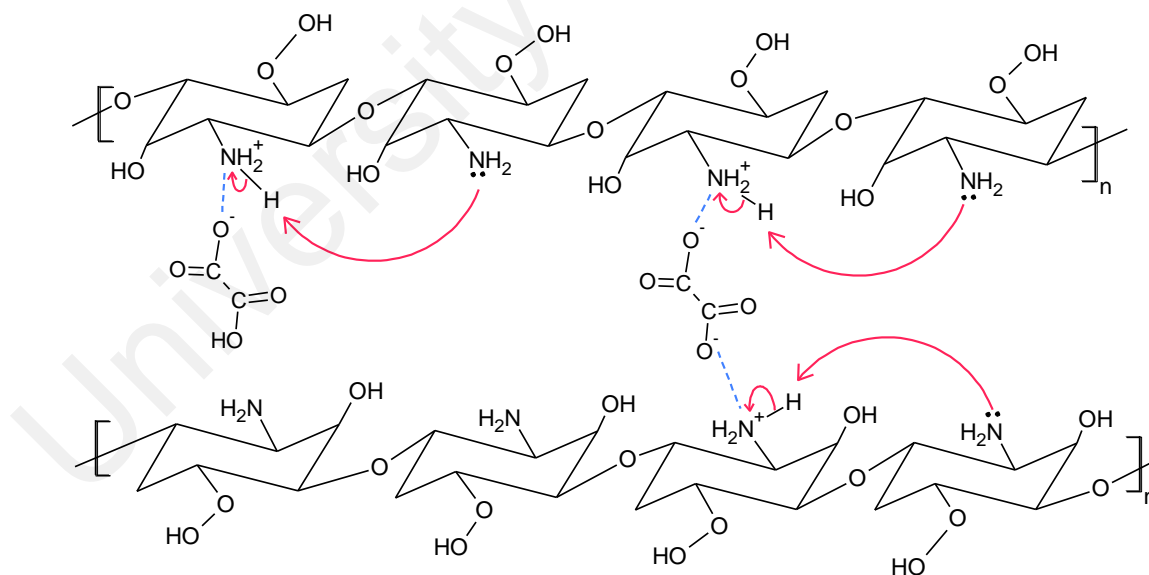


**Figure 4.6:** Possible conduction mechanism in chitosan-oxalic acid system.

The conduction mechanism in chitosan-oxalic acid system is best depicted in Fig. 4.6. In the schematic diagram, the curly arrow shows transport of proton. The

oxygen atom in the water molecule will form hydrogen bond with the hydrogen atom of the hydroxyl group in oxalic acid. The inductive effect in oxalic acid releases two protons ( $H^+$ ). These protons will attach to water molecule hence forming hydroxonium ion ( $H_3O^+$ ). Upon oxalic acid dissociation, oxalate ion and two hydroxonium ions will be produced. The hydroxonium ion will then protonate the amine group in the chitosan. The oxalate ion can crosslink two protonated amine groups ( $R-NH_3^+$ ) from two different chitosan chains due to coulombic electrostatic interaction (Selvasekarapandian *et al.*, 2006). By assuming the protonated amine  $R-NH_3^+$  of chitosan has similar tetrahedral structure as in ammonium ion  $NH_4^+$ , one of the hydrogen is weakly bonded to N (Hashmi *et al.*, 1990). The weakly bonded hydrogen will dissociate under the influence of electrical field (Hashmi *et al.*, 1990; Buraidah *et al.*, 2009). This led to proton  $H^+$  transport in solid chitosan-oxalic acid electrolytes. The movement of proton is shown by the curly arrow in Fig. 4.6.

#### 4.2.1 Temperature dependence of conductivity

The corresponding Nyquist plots for the highest conducting sample, OA40 at various temperatures are shown in Fig. 4.7. The bulk resistance,  $R_b$  value and the semi-circle region were observed to be reduced as the temperature increased. Moreover, the spikes become more significant with temperature increment. These indicate that the sample membrane OA40 is thermally active with ion migration contributing to as temperature increases (Krishnakumar & Shanmugam, 2012).

The temperature dependence of conductivity exhibited by the highest RT conducting sample membrane, OA40, is shown in Fig. 4.8 in the form of  $\log \zeta$  versus  $1000/T$ . The conductivity values at the measured temperatures are listed in Table 4.2. It

can be observed that the plots, in the temperature range 300 K to 348 K obey the Arrhenius expression given by:

$$\sigma = \sigma_0 \exp\left(\frac{-E_A}{k_B T}\right) \quad (4.8)$$

where  $\zeta_0$  is the pre-exponential factor,  $E_a$  is the activation energy of ionic conduction,  $k_B$  is the Boltzmann constant and  $T$  is the temperature in Kelvin (K).

The linear relation implied that there is no phase transition in the polymer matrix or the domain formed by OA addition (Selvasekarapandian *et al.*, 2005). This can be interpreted as no dynamic conformational change occurring in the polymer matrix. The calculated activation energy,  $E_A$ , is 0.61 eV with regression value  $R^2$  0.988 indicating that the points lie in an almost perfect straight line.

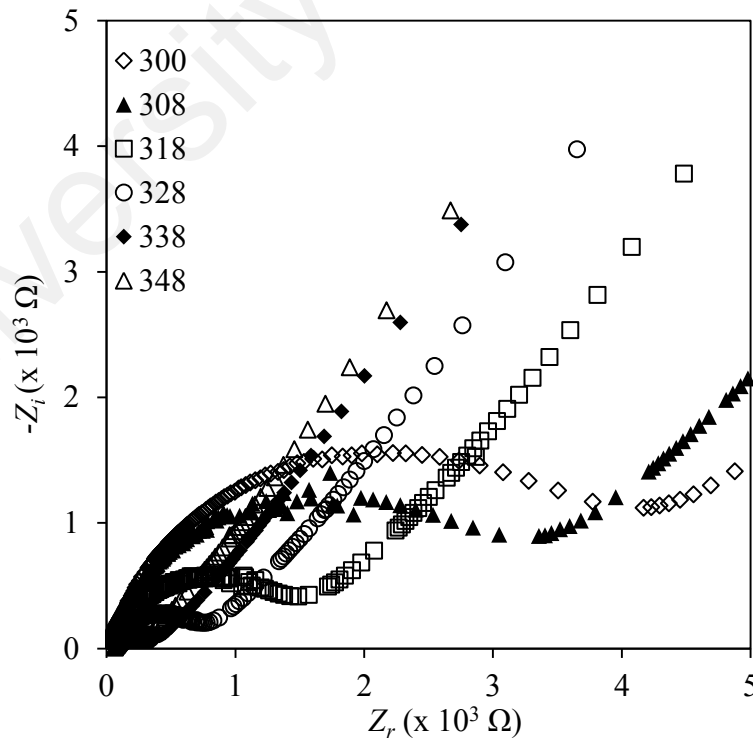


**Figure 4.7:** Nyquist plots for OA40 sample at elevated temperatures.

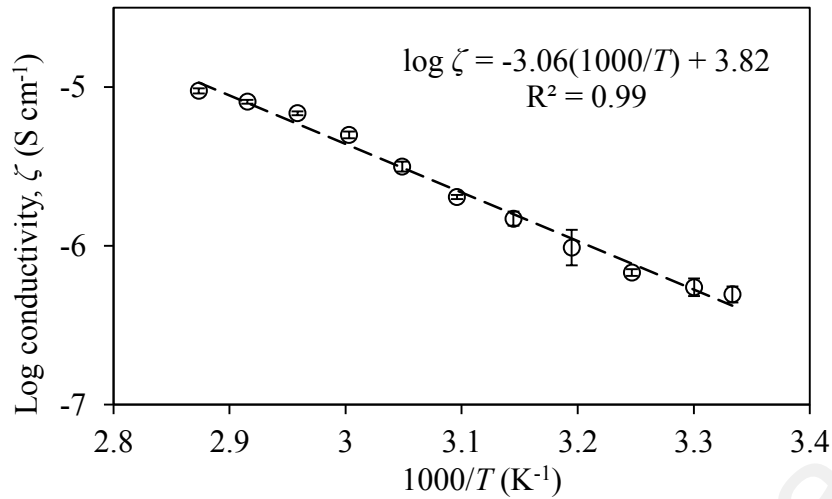


**Figure 4.8:** Plot of  $\log \zeta_{dc}$  vs.  $10^3/T$  (K<sup>-1</sup>) for OA 40 membrane with error bars.

The conduction in chitosan–oxalic acid sample membranes is contributed by the motion of protons (H<sup>+</sup>) from one protonated site to another amine site (see Fig. 4.6). During thermal application, the polymer chain acquires faster internal modes which results in bond vibration, favouring inter-chain and intra-chain ion hopping movements and local structure relaxations that increased the conductivity of the polymer electrolyte (Selvasekarapandian *et al.*, 2005; Sudhakar and Selvakumar, 2012).

**Table 4.2:** Ionic conductivity values of OA40 at various temperatures with area and bulk resistance  $R_b$ .

Temperature	Area (cm <sup>2</sup> )	Bulk resistance, $R_b$ (Ω)	Conductivity, $\zeta_{dc}$ (S cm <sup>-1</sup> )
300	3.14	4.56 x10 <sup>3</sup>	4.95 x10 <sup>-7</sup>
303	3.14	5.21 x10 <sup>3</sup>	5.50 x10 <sup>-7</sup>
308	3.14	4.21 x10 <sup>3</sup>	6.80 x10 <sup>-7</sup>
313	3.14	2.93 x10 <sup>3</sup>	9.77 x10 <sup>-7</sup>
318	3.14	1.93 x10 <sup>3</sup>	1.48 x10 <sup>-6</sup>
323	3.14	1.40 x10 <sup>3</sup>	2.04 x10 <sup>-6</sup>
328	3.14	9.18 x10 <sup>2</sup>	3.12 x10 <sup>-6</sup>
333	3.14	5.72 x10 <sup>2</sup>	5.01 x10 <sup>-6</sup>
338	3.14	4.18 x10 <sup>2</sup>	6.85 x10 <sup>-6</sup>
343	3.14	3.54 x10 <sup>2</sup>	8.10 x10 <sup>-6</sup>
348	3.14	3.02 10 <sup>2</sup>	9.48 x10 <sup>-6</sup>

In this chitosan–oxalic acid system, H<sup>+</sup> can hop from one protonated site to another amine group (NH<sub>2</sub>) since the polymer chains of chitosan in the electrolyte are able to make the bond vibration (Ng and Mohamad, 2008; Krishnakumar and Shanmugam, 2012). Increased in conductivity with temperature indicates the increase in mobility of the protons. According to Krishnakumar and Shanmugam (2012) the proton have gained kinetic energy and able to hop from a protonated amine site (NH<sub>3</sub><sup>+</sup>) to an unprotonated site (NH<sub>2</sub>).

#### 4.2.2 AC conductivity studies on System I

The *ac* impedance technique can be used to obtain the specific *dc* conductivity of the electrolytes. Figure 4.9(a) shows the variations of *ac* conductivity with frequency for samples with different OA contents. Figure 4.9(b) shows the variations of *ac* conductivity with frequency for the OA40 sample at different temperatures. The *ac* conductivity at different frequencies was calculated using equation:

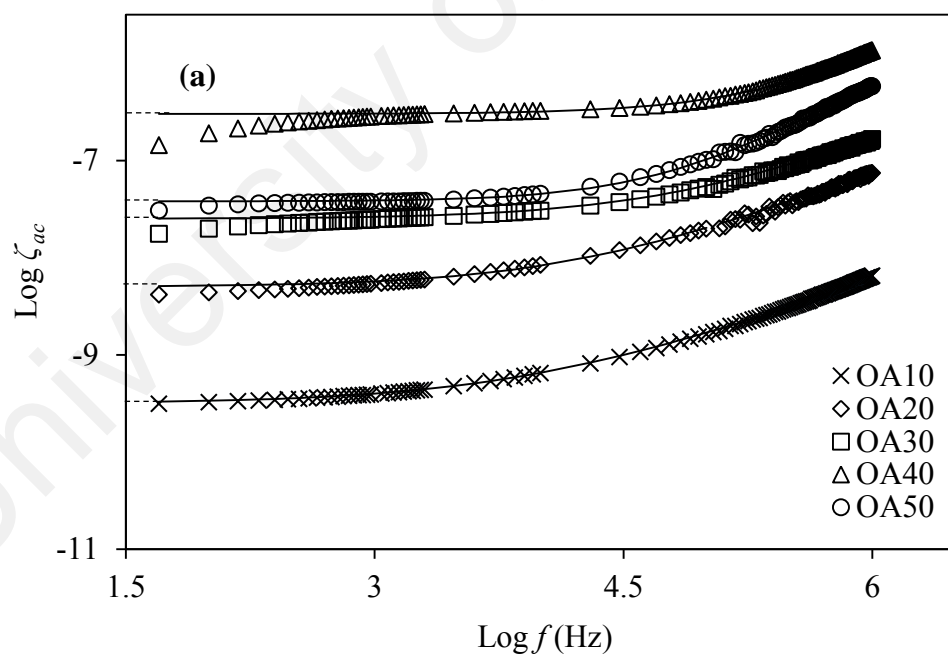
$$\sigma_{ac} = \frac{Z_r}{(Z_r^2 + Z_i^2)} \frac{t}{A} \quad (4.9)$$

where  $Z_r$  is the real part of the impedance,  $Z_i$  is the imaginary part of the impedance,  $t$  is the thickness of the sample (cm) and  $A$  is the cross-sectional area of the membranes (cm<sup>2</sup>). In both figures, the graphs consist of frequency dependent regions and frequency independent regions that are important characteristics for ion conducting membranes (Cheruku *et al.*, 2012).

It can be observed that the edge of the plateaus (the frequency independent regions) in Fig. 4.9(a) is shifted to higher frequencies as oxalic acid content is increased. The conductivity value obtained from extrapolating the plateau region is not much

different to the experimental values determined from the Nyquist plots. Thus it can be inferred that direct current conductivity,  $\zeta_{dc}$  can be evaluated from the extrapolation of the frequency independent plateau to the vertical axes.

The frequency dependent regions at very low frequencies in both figures correspond to electrode polarization. From the *ac* conductivity at various temperatures in Fig. 4.9(b), it can be observed that the plateaus shifted from lower to higher frequency regions as temperature is increased indicating that the conductivity increases with increasing temperature. The low conductivity values at low frequency (at lower temperature) regions are related to the accumulation of ions due to the slow periodic changes of the electric field (Chopra *et al.*, 2003, & Khiar *et al.*, 2006).



‘Figure 4.9, continued’

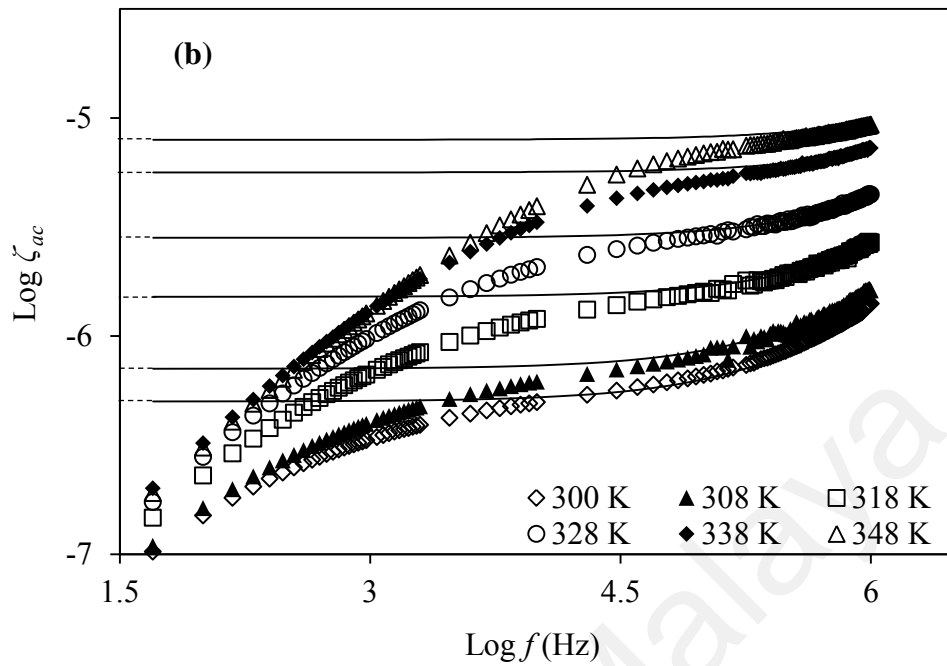


**Figure 4.9:** Fit to equation (4.10) of the real part of conductivity vs. frequency for (a) sample membranes with different oxalic acid contents at room temperature, 300 K, and (b) sample membrane OA40 at various temperatures (dotted line represent the extrapolation).

The variation of *ac* conductivity with frequency obeys the Jonscher’s universal power law (UPL) and is given by:

$$\sigma(\omega) = \sigma_{dc} + A\omega^s \quad (4.10)$$

where  $\zeta_{dc}$  is the frequency independent plateau,  $A$  is a temperature dependent term and  $s$  is the frequency exponent with value in the range  $0 < s < 1$ . The values obtained for  $\zeta_{dc}$ ,  $A$  and  $s$  by fitting Eq. (4.10) are tabulated in Table 4.3.

**Table 4.3:** Comparison of parameters obtained from fit of the experimental data to Eq. 8 for (a) sample membranes with different oxalic acid content at room temperature, 300 K and (b) sample membrane OA40 at various temperatures.

(a)	Membrane	$\zeta_{dc}$	$A$	$s$
	OA10	$3.16 \times 10^{-10}$	$4.00 \times 10^{-13}$	0.61
	OA20	$5.01 \times 10^{-9}$	$2.00 \times 10^{-12}$	0.67
	OA30	$2.51 \times 10^{-8}$	$3.00 \times 10^{-12}$	0.69
	OA40	$3.02 \times 10^{-7}$	$1.00 \times 10^{-12}$	0.88
	OA50	$3.80 \times 10^{-8}$	$1.00 \times 10^{-12}$	0.84
(b)	Temperature (K)	$\zeta_{dc}$	$A$	$s$
	300	$3.02 \times 10^{-7}$	$2.00 \times 10^{-12}$	0.84
	308	$6.17 \times 10^{-7}$	$2.00 \times 10^{-12}$	0.86
	318	$1.32 \times 10^{-6}$	$2.20 \times 10^{-12}$	0.88
	328	$2.34 \times 10^{-6}$	$2.00 \times 10^{-12}$	0.88
	338	$5.01 \times 10^{-6}$	$2.00 \times 10^{-12}$	0.90

The value of  $\zeta_{dc}$  shows the maximum value for OA40 at room temperature and the value increases with temperature. Sample OA40 in the temperature range 300 K to 348 K displays that the fittings  $s$  values approached 1 which can be observed in Fig. 4.10(b). It can be seen that values of  $s$  of OA40 are almost constant with increasing temperature. This behaviour of  $s$  indicates that quantum-mechanical tunnelling (QMT) model accounts for the ac conduction mechanism in OA40 sample since the values of  $s$  are independent of temperature (Matsuura *et al.*, 1996; Ravi Kumar & Veeraiah, 1998; Majid & Arof, 2007). QMT defines that the polarons (in this work they are made up of protons and their stress fields) are able to tunnel through the potential barrier that exists between two possible complexation sites.

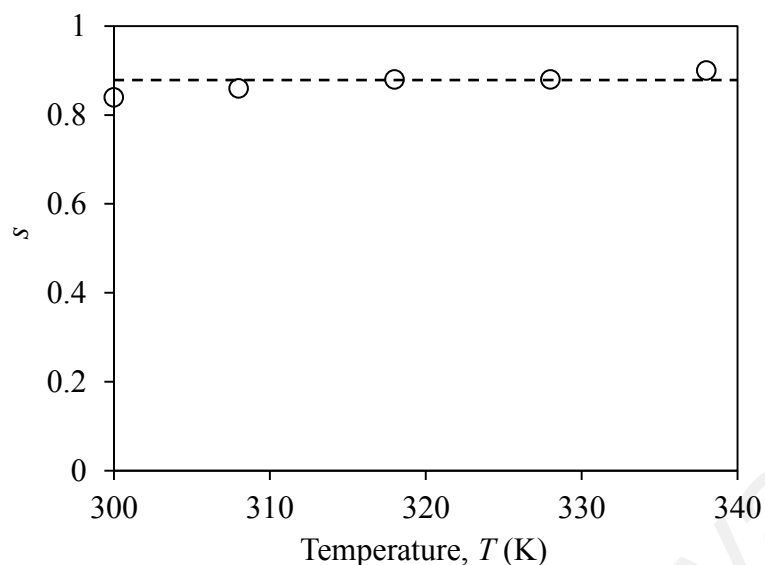


**Figure 4.10:** Variation of exponent  $s$  versus temperature for OA40.

#### 4.2.3 Electrical Analyses on System I

A study on dielectric constant value of both systems was carried out in order to measure the stored charge (Winie & Arof, 2004). The real part of complex dielectric function permittivity,  $\epsilon_r$  of chitosan based sample decreases non-linearity with the increase of frequency which can be seen in both Fig. 4.11 and 4.12. In addition, the gradual decrease in  $\epsilon_r$  values at high frequencies confirms the contribution of polymeric molecular polarization and ionic conduction processes to the dielectric dispersion, whereas the large increase in  $\epsilon_r$  with decreases of frequency is owing to the electrode polarization (Choudhary & Sengwa, 2011). Since the charge is made up of protons ( $H^+$ ), the increase in dielectric constant at high frequency region for different amounts of oxalic acid in Fig. 4.11 represents the increase in the number of  $H^+$ . The effect of temperature on dielectric constant of OA40 can be seen in Fig. 4.12. The increment of dielectric constant with temperature results in the increasing number of  $H^+$  which due to the greater dissociation at higher temperature. This implies that conductivity is thermally assisted (Winie & Arof, 2004).

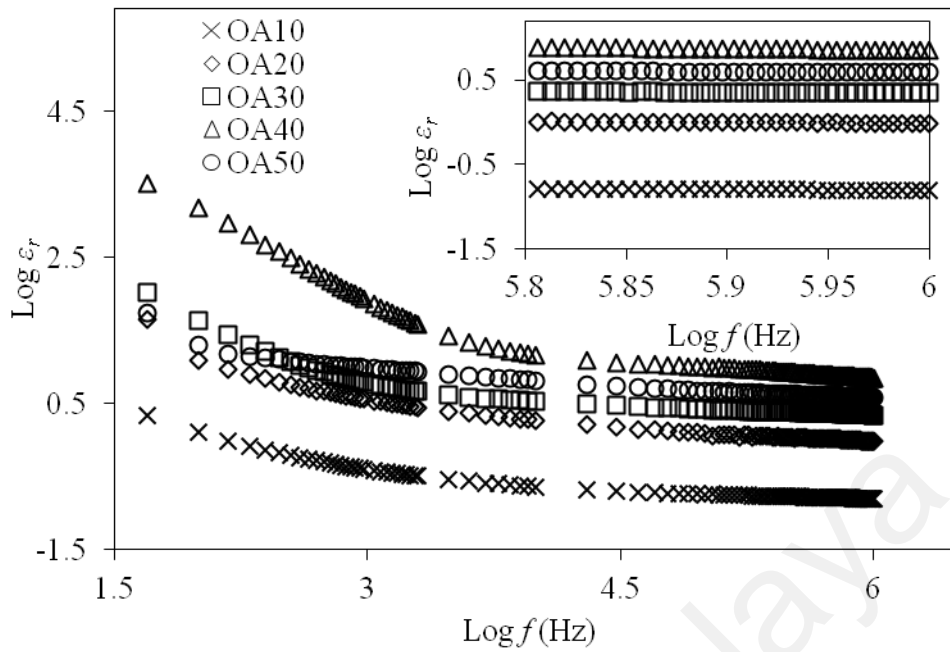


**Figure 4.11:** The dielectric constant,  $\epsilon_r$  for samples with different amount of OA versus  $\log f$  at room temperature, 300 K (the inset shows the enlarged plot at high frequencies).

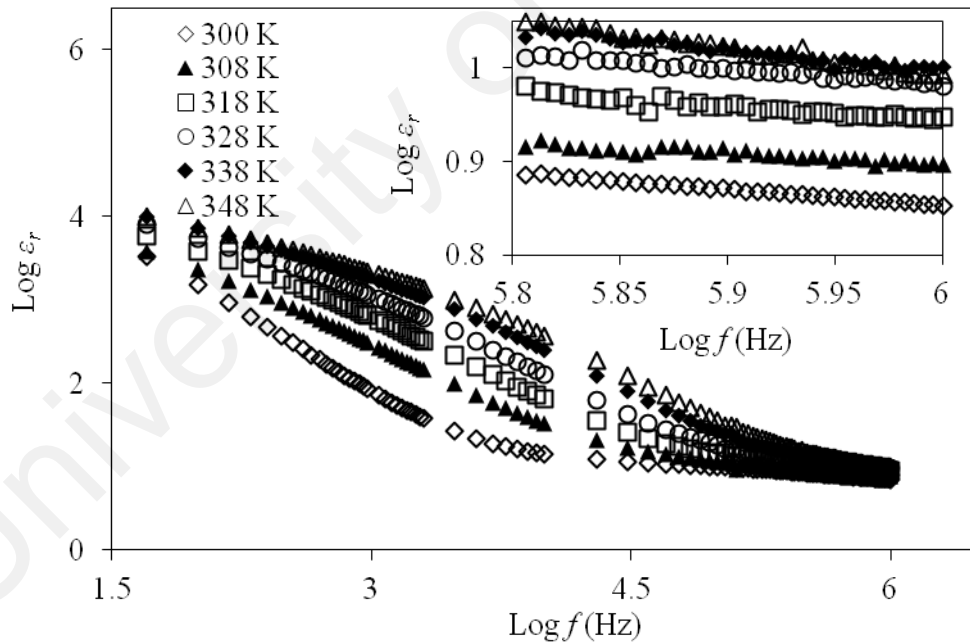


**Figure 4.12:** The dielectric constant,  $\epsilon_r$  of 40 wt. % OA (OA40) sample versus  $\log f$  at various temperatures (the inset shows the enlarged plot at high frequencies).

The dielectric constant can be estimated at higher frequency as it become frequency independent above  $10^5$  Hz. Both figures show high value of  $\epsilon_r$  at low frequencies which were attributed to the accumulation of the ions (Reicha *et al.*, 1991;

Singh *et al.*, 1998). The dielectric constant values in ascending order are 0.16, 1.00, 2.28, 4.00, and 7.44 for OA10, OA20, OA30, OA50 and OA40 respectively. The reduction of dielectric constant of sample with OA50 was likely caused by the increasing amount of ions that undergo re-association. Temperature dependence of dielectric constant for sample OA40 sample shows an increasing value of dielectric constant up to 338 K and dropped slightly at 348 K due to the higher charge carrier density which also induced ion re-association. The conductivity values and the dielectric constant relationship can be summarized in Fig. 4.13, as we can see that sample OA40 exhibits the highest dielectric constant values with respect to the ionic conductivity values. The phenomenon of polarization effect increases with respect to temperature can be seen in Fig. 4.14. The dielectric constant,  $\epsilon_r$  value seems to be constant at higher temperatures and this can be implied that the dissociation of the salt has reached its maximum (Reicha *et al.*, 1991; Singh *et al.*, 1998).

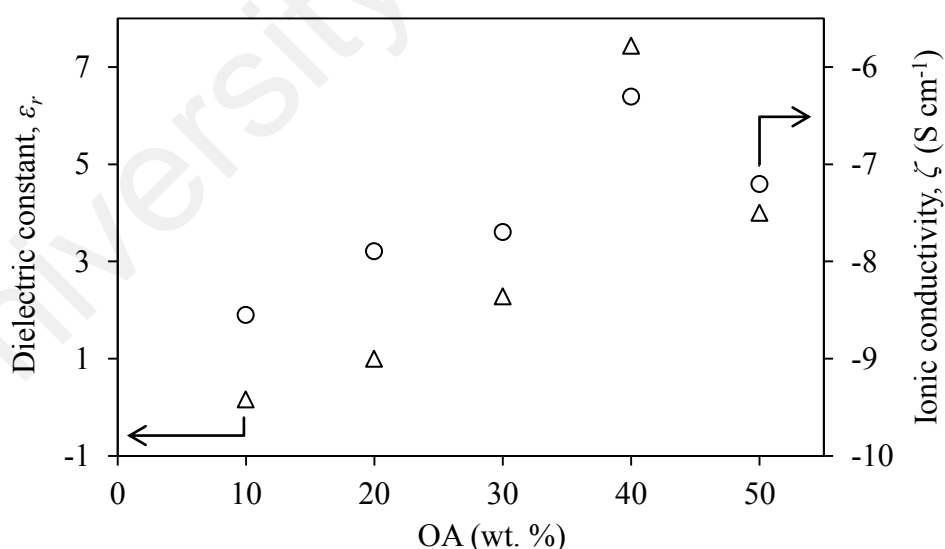


**Figure 4.13:** Oxalic acid dependence of dielectric constant,  $\epsilon_r$  and ionic conductivity at room temperature, 300 K.

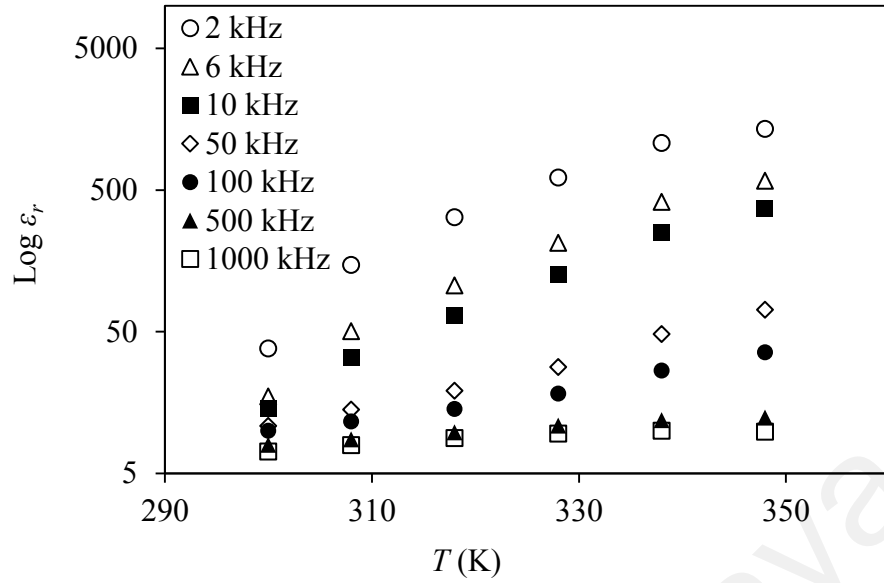


**Figure 4.14:** Temperature dependence of dielectric constant,  $\epsilon_r$  for OA40 at selected frequencies.

A plot of  $\tan \delta$  as a function of frequency can determine the relaxation parameter of the sample membranes which is useful to investigate the dipole relaxation in polymer electrolytes (Aziz *et al.*, 2012). The dielectric loss tangent ( $\tan \delta$ ) can be calculated using the following equation:

$$\tan \delta = \frac{\epsilon''}{\epsilon'} = \frac{Z'}{Z''} \quad (4.11)$$

The ratio of energy loss to energy stored in Eq. 4.11 is called dissipation factor. The variation of loss tangent as a function of frequency for chitosan incorporated with various concentrations of oxalic acid at room temperature is presented in Fig. 4.15. The variation of  $\tan \delta$  for the highest conducting sample OA40 at elevated temperatures is shown in Fig. 4.16.

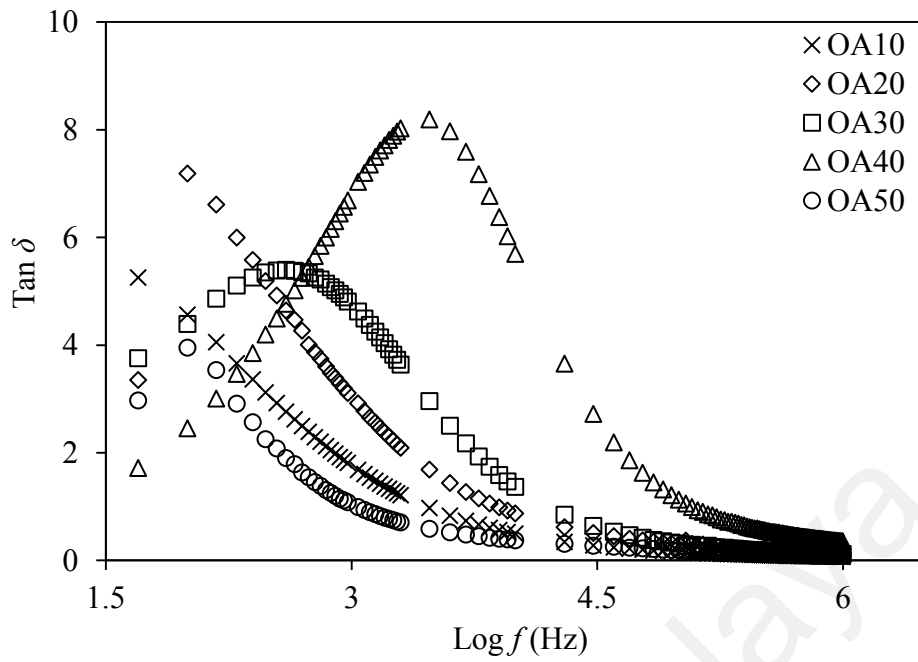


**Figure 4.15:** Variation of  $\tan \delta$  with frequency for samples with different amount of OA at room temperature, 300 K.

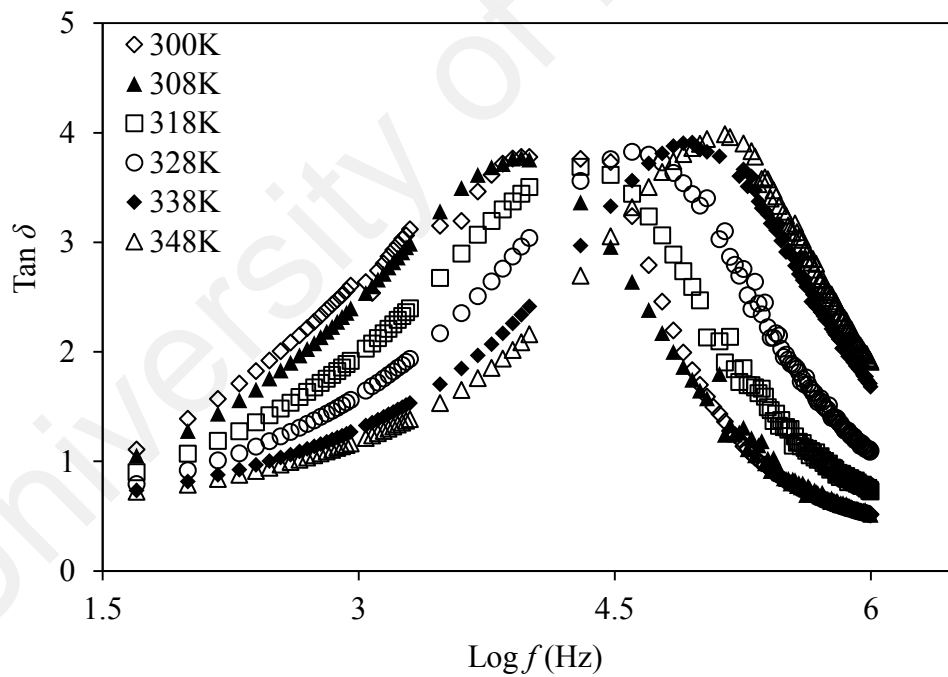


**Figure 4.16:** Variation of  $\tan \delta$  with frequency for OA40 sample at elevated temperatures.

Woo *et al.* (2012) and Chopra *et al.* (2003) stated that at low frequencies,  $\tan \delta$  increases with frequency because the active component (ohmic) is more dominant than the reactive component (capacitive) until a maximum in  $\tan \delta$  is reached. As the

operating frequency approached 1 MHz,  $\tan \delta$  decreases with frequency because the ohmic portion is independent of frequency and the reactive component grows in proportion to the frequency (Woo *et al.*, 2012; Chopra *et al.* 2003). The appearance of a resonance peak with increasing frequency was observed in both Fig. 4.15 and Fig. 4.16. The loss peak in Fig. 4.15 is shifted towards higher frequency with increasing oxalic acid contents until 40 wt. % OA at 3 kHz thereby reducing the relaxation time. The  $\tan \delta$  peaks in Fig. 4.16 are observed to shift towards higher frequency (as the operating frequency approaches 138 kHz) with increasing temperature imply that the relaxation time is reduced with increasing temperature. The temperature dependence of relaxation time  $\tau$  suggests thermally activated behaviour described by Arrhenius equation given by:

$$\sigma = \sigma_0 \exp\left(\frac{-E_B}{k_B T}\right) \quad (4.13)$$

where  $\eta_0$  is the pre-exponential factor,  $E_B$  is the activation energy for relaxation,  $k_B$  is the Boltzmann constant and  $T$  is the absolute temperature.

By taking Debye equation in an ideal case, and assuming the static dielectric constant and high frequency dielectric constant is almost the same, the relaxation time,  $\eta$  can be calculated from the frequency,  $f_{max}$  corresponding to the peak according to Eq. 4.12 (Woo *et al.*, 2012):

$$2\pi f_{max} = \frac{1}{\tau} \quad (4.12)$$

where  $\eta$  is the conductivity relaxation time and  $f_{max}$  is the frequency corresponding to maximum of loss tangent peak. The plot of relaxation time as a function of oxalic acid content (wt. %) is shown in Fig. 4.17. The conductivity relaxation time shows the lowest value for sample OA40 which correspond to its highest conductivity value in this

system. It has been stated that the conductivity relaxation time and ionic conductivity have strong correlation i.e., the  $\zeta_{dc}$  increases when  $\eta$  decreases and vice-versa. However the relaxation time increased for sample OA50 due to the possible re-association of  $H^+$  and  $COO^-$  ions of oxalate ions which affecting the amorphousness of the sample. The re-association of  $H^+$  and  $COO^-$  ions results in the formation of hydrogen bond between O at C-3 or O-5 and H of amine group ( $R-NH_2$ ) hence decreasing the amorphousness of the polymeric chain of chitosan.

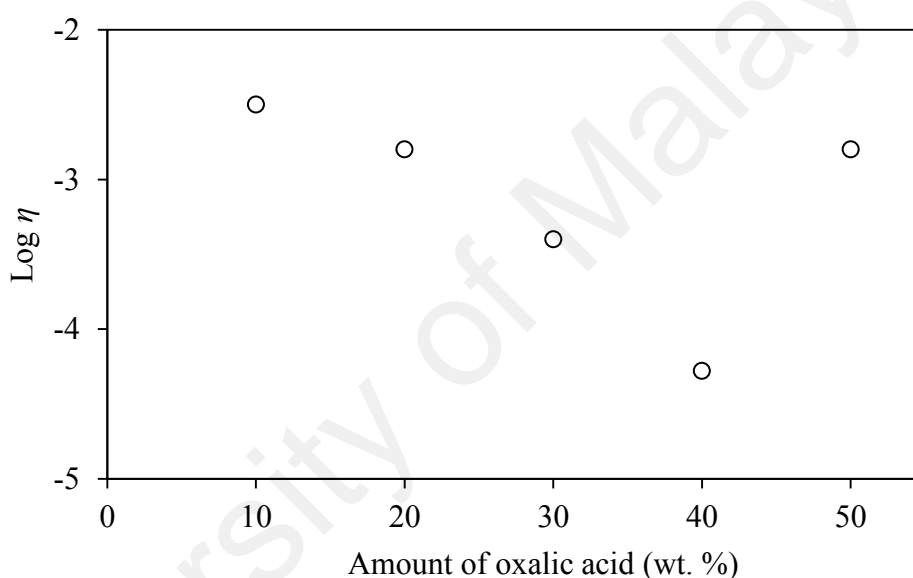


**Figure 4.17:** Log  $\eta$  versus weight percentage of oxalic acid.

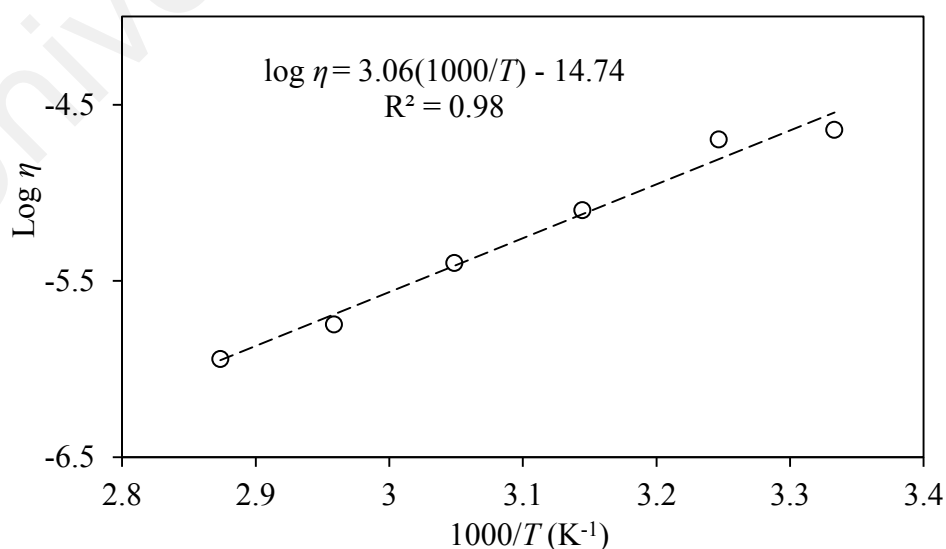


**Figure 4.18:** Variation of log  $\eta$  with temperature for the highest conducting sample OA40 (dotted line depicts that the points lie on a straight line hence obeying Arrhenius expression).

In order to determine the activation energy of OA40 sample, a plot of  $\log \eta$  versus  $1000/T$  was plotted and displayed in Fig. 4.18. The linear relationship suggests that the variation in conductivity with temperature obeys the Arrhenius equation. The activation energy for relaxation  $E_B$  calculated from the fitting of data points is 0.61 eV for sample with 40 wt. % OA (OA40).

### 4.3 Conductivity Studies on Chitosan–Oxalic acid–Glycerol system (System II)

The room temperature ionic conductivity of the freshly prepared samples is obtained by the same technique as mentioned in the Section 4.2 with stainless steel as the blocking electrodes. Plasticization is an ionic conductivity enhancement alternative route with the addition of a suitable chemical compound to the electrolyte.

Conductivity enhancement by 1 to 2 orders of magnitude has been investigated by adding 50 wt. % propylene carbonate, 50 wt. % tetraglyme and 50 wt. % dimethyl formamide into poly(ethylene oxide) samples (MacFarlane *et al.*, 1995; Forsyth *et al.*, 1995). Missan and co-workers (2006) reported the addition of dimethylacetamide as plasticizer to the poly(vinylidene fluoride-co-hexafluoro propylene) based electrolyte has given rise to three orders of magnitude in conductivity. Pawlicka and co-workers reported the conductivity increments by four orders of magnitude in samples of chitosan doped with hydrochloric acid which were plasticized with ethylene glycol and glycerol (Pawlicka *et al.*, 2008). The conductivity of both samples increased from  $9.2 \times 10^{-8} \text{ S cm}^{-1}$  to  $9.5 \times 10^{-4} \text{ S cm}^{-1}$  and  $2.4 \times 10^{-4} \text{ S cm}^{-1}$  with the addition of 59 wt. % glycerol and 68 wt. % ethylene glycol respectively.

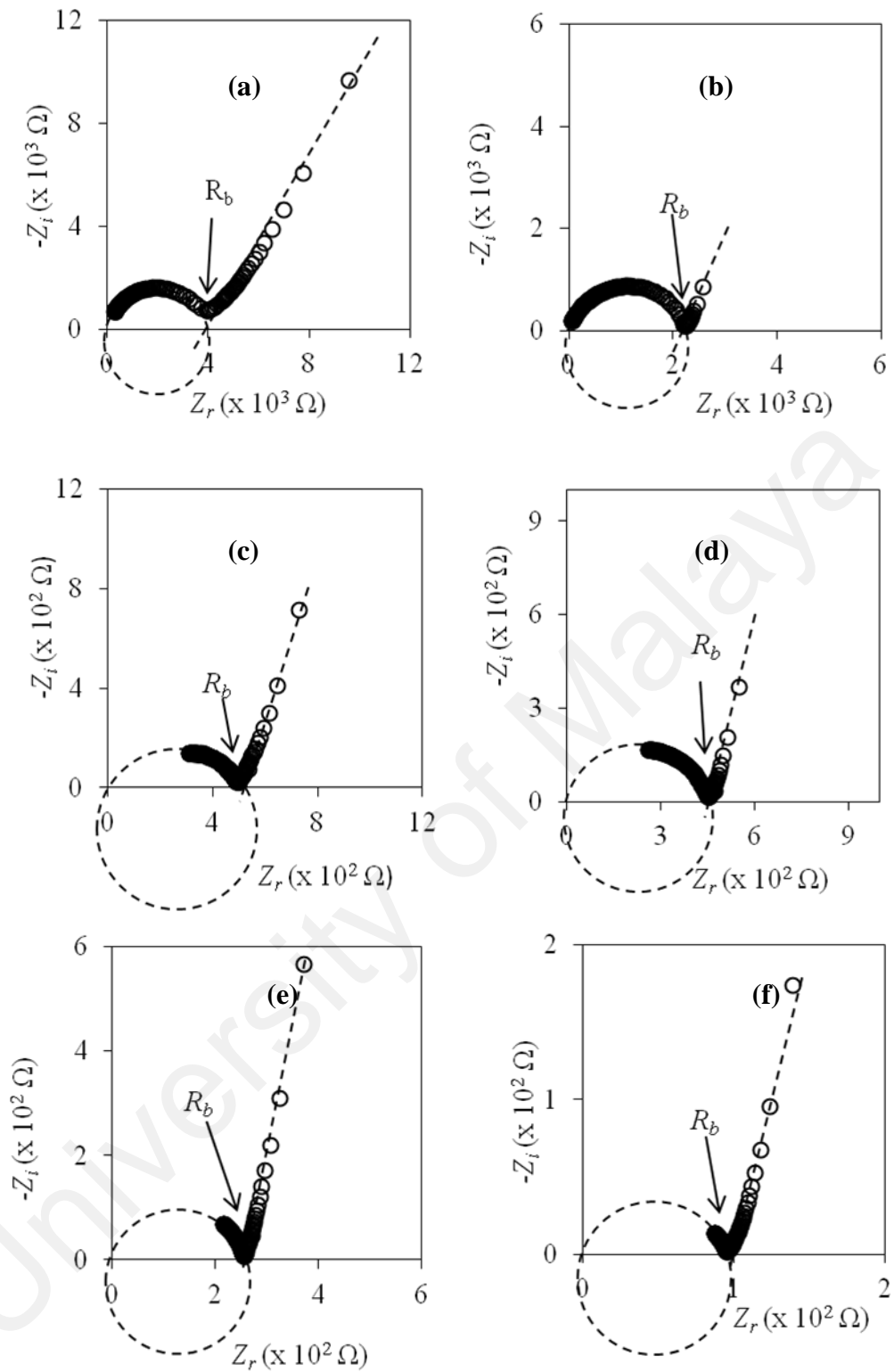


**Figure 4.19:** Nyquist plots of samples containing different wt. % of glycerol (a) 10 (OG10), (b) 20 (OAG0), (c) 30 (OG30), (d) 40 (OG40), (e) 50 (OG50) and (f) 60 (OG60).

The Nyquist plots of chitosan–oxalic acid–glycerol (OG) electrolyte samples with different glycerol concentrations are shown in Fig. 4.19 from the plots the bulk

resistance,  $R_b$  can be determined and used to calculate the ionic conductivity. The minimization of possible charge carrier concentration changes and the time average of the changes during the measurements can be done using a small applied voltage, 10 mV (Arof *et al.*, 2014). The depressed semi-circle can be observed at high frequencies in the Nyquist plot of Fig. 4.19 is due to the grain-interior of the sample that indicates the presence of electrolyte bulk effect and the tilted spike at low frequency that results from blocking electrode/electrolyte polarization (Cui *et al.*, 2008).

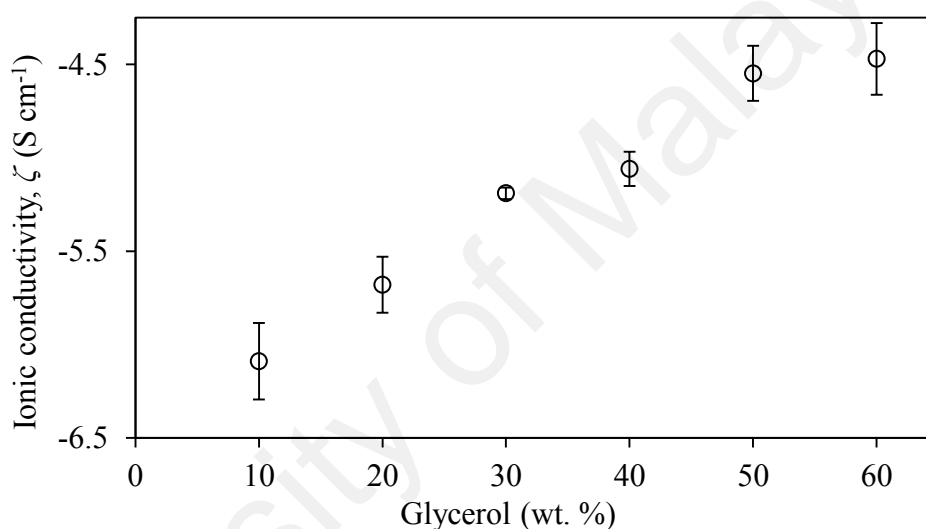


**Figure 4.20:** Graph of ionic conductivity of membranes for various glycerol contents at room temperature (300 K) with error bars.

The ionic conductivity of the plasticized samples at room temperature with different glycerol content is shown in Fig. 4.20. The conductivity increased with glycerol content and maximized at 60 wt. %. Unlike the chitosan–OA system, there is no decrease in conductivity after 60 wt. % glycerol. However the glycerol content is maximized at 60 wt. % due to the poor mechanical properties at higher glycerol content as the samples are no longer free standing film. The  $R_b$  value, thickness, and ionic conductivity value at room temperature for samples with different glycerol content are tabulated in Table 4.4. With the addition of glycerol as plasticizer up to 60 wt. %, the

conductivity of OA40 (the highest conducting chitosan based electrolyte from System I) is increased by almost more than two orders of magnitude from  $4.95 \times 10^{-7} \text{ S cm}^{-1}$  to  $9.12 \times 10^{-5} \text{ S cm}^{-1}$ .

**Table 4.4:** Different weight percentage (wt. %) of glycerol used to prepare chitosan membranes and the thickness, bulk resistance and ionic conductivity values of all membranes at room temperature (300 K) with efficient area of 3.14 cm.

Glycerol (Gly) wt. %	Sample designation	Thickness (cm)	Bulk resistance, $R_b$ ( $\Omega$ )	Ionic conductivity, $\zeta_{dc}$ ( $\text{S cm}^{-1}$ )
10	OG10	0.01	4000	$8.13 \times 10^{-7}$
20	OG20	0.01	2200	$2.09 \times 10^{-6}$
30	OG30	0.01	494	$6.45 \times 10^{-6}$
40	OG40	0.01	437	$8.71 \times 10^{-6}$
50	OG50	0.02	251	$2.82 \times 10^{-5}$
60	OG60	0.02	94	$9.12 \times 10^{-5}$

A schematic diagram as depicted in Fig. 4.21 was drawn in order to understand the interactions that occurred in the sample membranes after the addition of plasticizer. As explained in section 4.2, the ionic conductivity in chitosan-oxalic acid system is caused by the displacement of protons from one site to other vacant sites under the influence of electrical field since one of the protons in the protonated amine ( $\text{NH}_3^+$ ) of chitosan is loosely bonded to N (Hashmi *et al.*, 1990; Buraidah *et al.*, 2009). The curly arrow in the mechanism scheme shows the movement of proton. The negatively charged O of oxalate ion is expected to form coulombic electrostatic interaction with H of the protonated amine ( $\text{NH}_3^+$ ). Addition of glycerol results in conductivity increment as the H of hydroxyl group (OH) in glycerol favours to interact (i.e. hydrogen bonding) with carbonyl group of oxalic acid (Lavorgna *et al.*, 2010). This interaction causes the hydrogen of hydroxyl group in oxalic acid to be released easily as proton  $\text{H}^+$  thus

increases the proton number for ionic conduction in the plasticized sample membranes (System II).

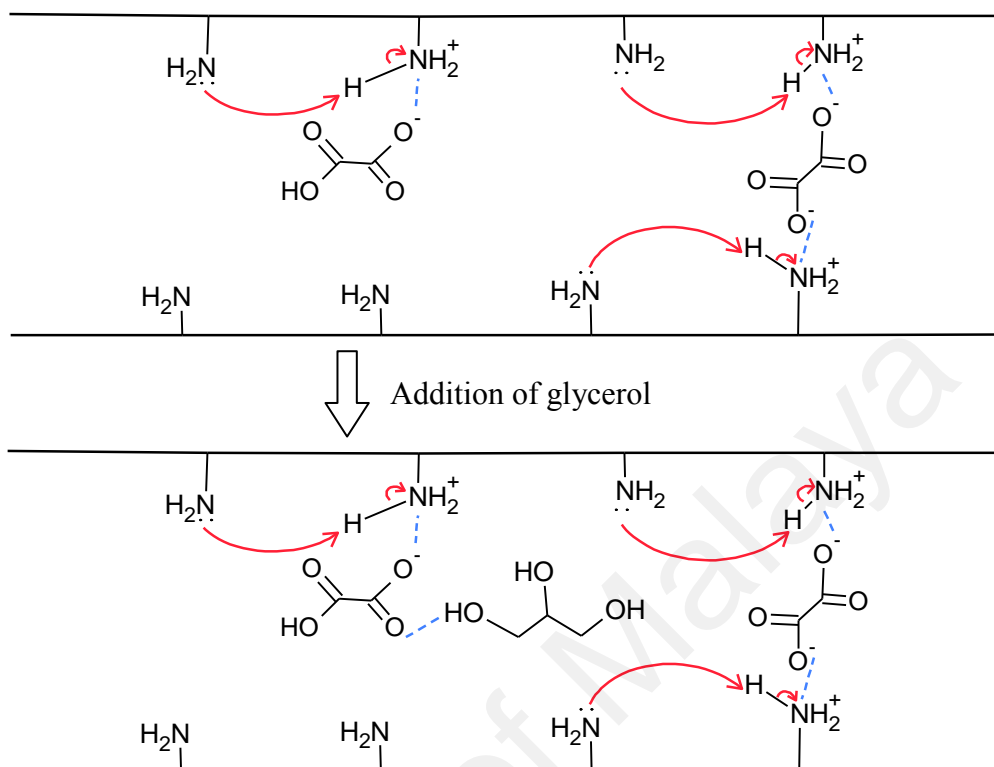


**Figure 4.21:** Possible conduction mechanism in chitosan-oxalic acid-glycerol system.

#### 4.3.1 Temperature dependence of conductivity for System II

Fig. 4.22 shows Nyquist plot for the highest conducting sample, OG60 at elevated temperatures ranged between 300 K and 373 K. The semi-circle region at 300 K was observed to diminish as the temperature increased. The bulk resistance,  $R_b$  which evaluated from the intersection at the real impedance axis  $Z_r$  is also decreased with the increasing temperature. This indicates that the sample membrane OG60 is thermally active and the conductivity value is increasing with the temperature.

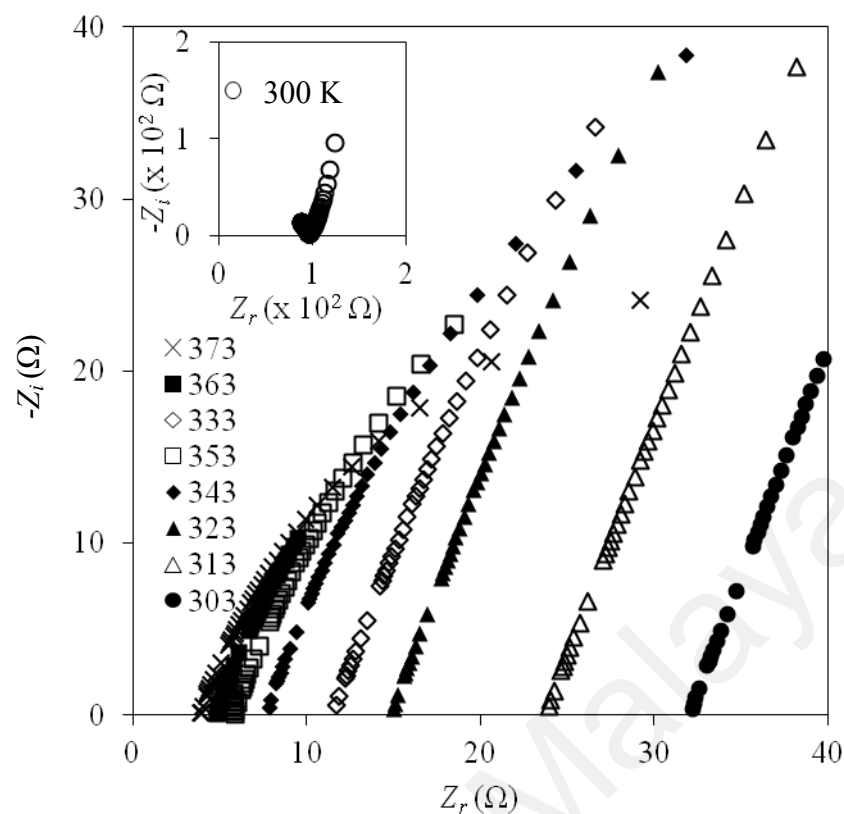


**Figure 4.22:** Nyquist plot for OG60 sample at various temperatures.

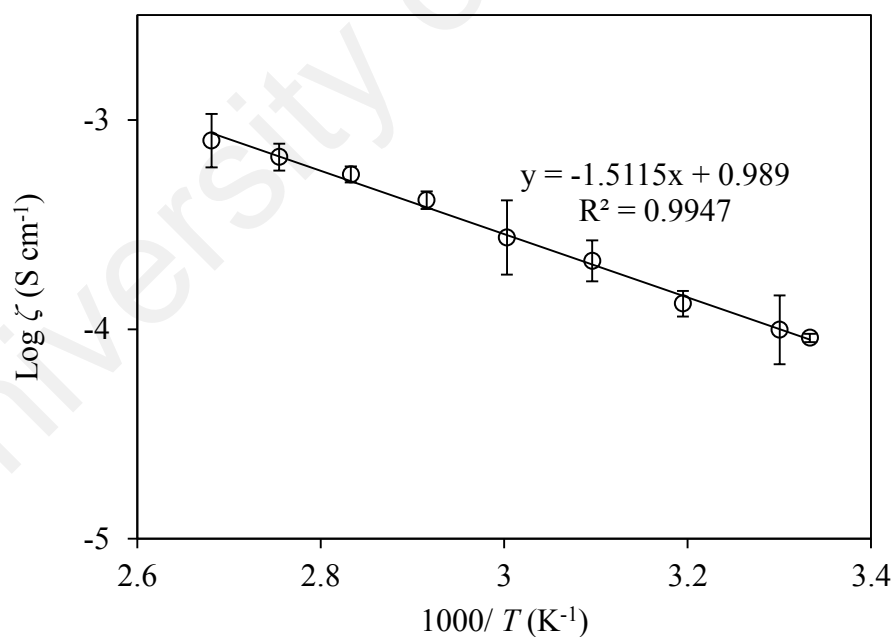


**Figure 4.23:** Plot of  $\log \zeta_{dc}$  vs.  $10^3/T$  ( $K^{-1}$ ) for OG60 membrane with error bars.

The temperature dependence of conductivity exhibited by the highest RT conducting sample membrane OG60 and shown in Fig. 4.23 in the form of  $\log \zeta$  vs.

$1000/T$  obeys the Arrhenius expression. This can be interpreted as no dynamic conformational change occurred in polymer matrix. The conductivity value at each temperature measured is listed in Table 4.5. The calculated activation energy,  $E_A$ , is 0.30 eV with regression value  $R^2$  0.9947 indicating that the points lie in an almost perfect straight line. From Fig. 4.23, the experimental temperature ranged from 300 K to 373 K. This is due to the sample in System II that could withstand higher experimental temperature compared to System I by which the temperature was maximized at 348 K.

**Table 4.5:** Ionic conductivity values of OG60 at various temperature with area and bulk resistance  $R_b$ .

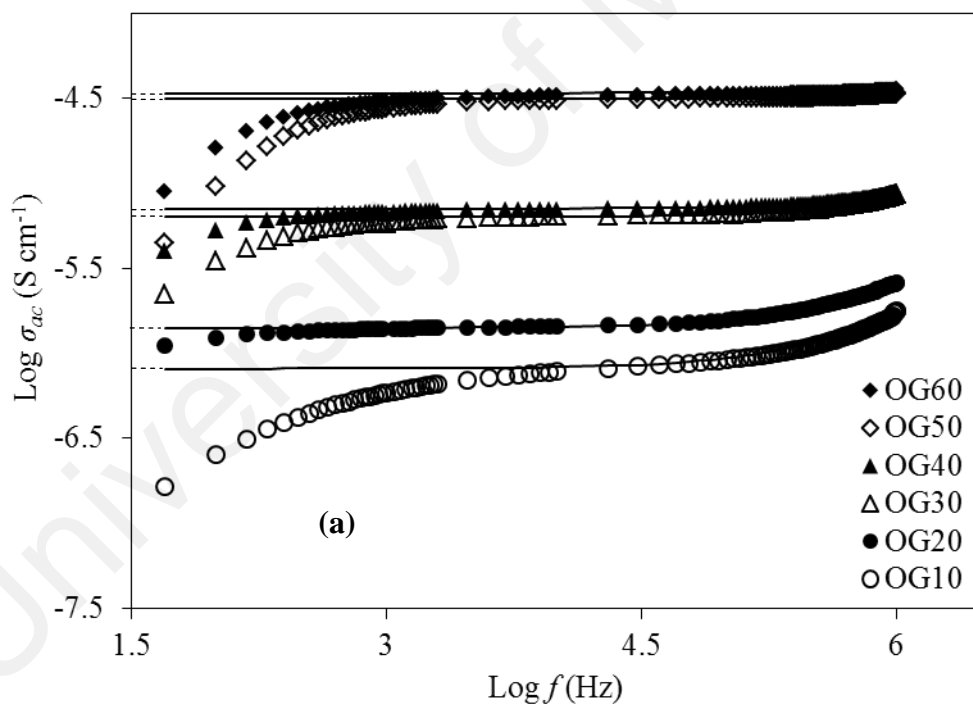
Temperature	Area (cm <sup>2</sup> )	Bulk resistance, $R_b$ ( $\Omega$ )	Conductivity, $\zeta_{dc}$ (S cm <sup>-1</sup> )
300	3.14	94	$9.12 \times 10^{-5}$
303	3.14	32	$9.94 \times 10^{-5}$
313	3.14	24	$1.33 \times 10^{-4}$
323	3.14	15	$2.12 \times 10^{-4}$
333	3.14	12	$2.74 \times 10^{-4}$
343	3.14	8	$4.13 \times 10^{-4}$
353	3.14	6	$5.49 \times 10^{-4}$
363	3.14	5	$6.64 \times 10^{-4}$
373	3.14	4	$7.95 \times 10^{-4}$

During thermal application, the polymer chain acquires faster internal modes which results in bond vibration, favouring hopping inter-chain and intra-chain ion movements and local structure relaxations hence increase the conductivity of the polymer electrolyte (Selvasekarapandian *et al.*, 2005; Sudhakar and Selvakumar, 2012). In this chitosan–oxalic acid-glycerol system,  $H^+$  can hop from one protonated site to another amine group ( $NH_2$ ) since the polymer chains of chitosan in the electrolyte are able to make the bond vibration (Ng and Mohamad, 2008; Krishnakumar and Shanmugam, 2012). This hopping mechanism indicates more protons gained kinetic

energy by thermally activated hopping of ions between trapped/ restricted amine group (NH<sub>2</sub>) sites (Krishnakumar and Shanmugam, 2012).

#### 4.3.2 AC conductivity studies on System II

The variation of *ac* conductivity with frequency for System II has been calculated and fitted to the Jonscher's UPL as given by Eq. 4.9 and Eq. 4.10 respectively. The plots are shown in Fig. 4.24(a) at room temperature whereas Fig. 4.24(b) shows the variations of *ac* conductivity with frequency for the OG60 sample at different temperatures. The values obtained for  $\zeta_{dc}$ , *A* and *s* are tabulated in Table 4.6.



'Figure 4.24, continued'

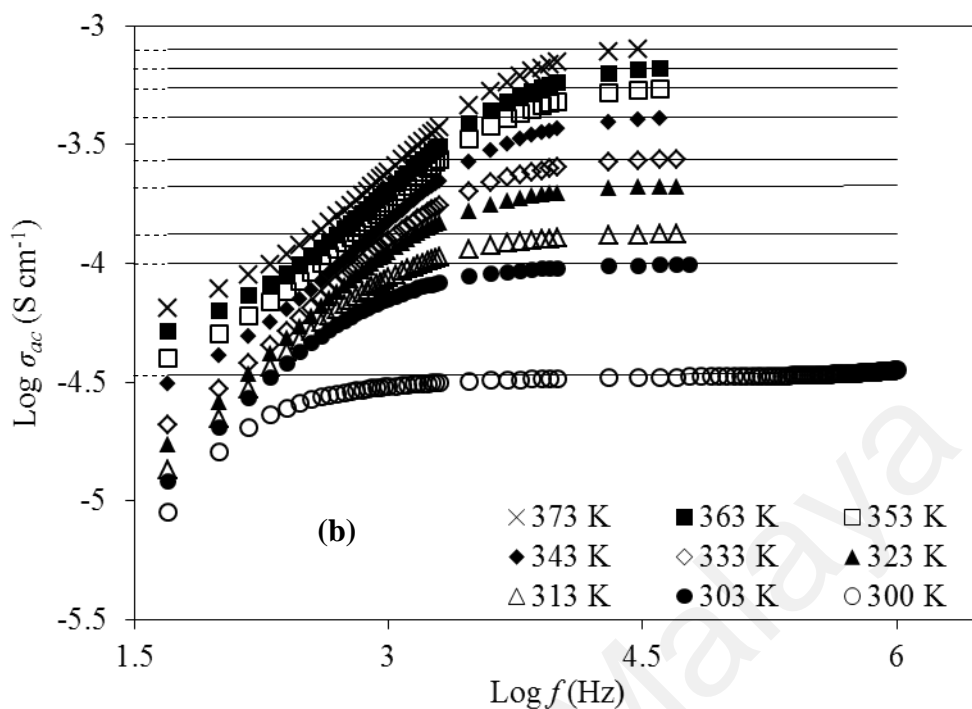


**Figure 4.24:** Fit to Eq. (4.10) of the real part of conductivity against frequency for (a) sample membranes with different oxalic acid contents at room temperature, 300K, and (b) sample membrane OG60 at various temperatures (dotted line represent the extrapolation).

The edge of the plateaus (the frequency independent regions) in Fig. 4.24(a) is observed to shift towards higher frequencies as glycerol content is increased. The frequency dependent regions at lower frequencies in both figures correspond to the electrode polarization. From *ac* conductivity at elevated temperatures in Fig. 4.24(b), the plateaus shifted from lower to higher frequency regions as temperature is increased indicating that the conductivity is a temperature dependent process. The low conductivity values at low frequency (at lower temperature) regions are related to the accumulation of ions at the electrode/electrolyte interface due to the slow periodic changes of the electric field (Chopra *et al.*, 2003; Khiar *et al.*, 2006).

The value of  $\zeta_{dc}$  is maximum for OG60 at room temperature. Sample OG60 in the temperature range 300 K to 373 K displays that the fittings *s* values approached 1 which can be observed in Fig. 4.24(b). It can be seen that values of *s* of OG60 are

constant with increasing temperature. The independence of  $s$  values with increasing temperatures verifies that the quantum-mechanical tunnelling (QMT) model accounts for the *ac* conduction mechanism in OG60 sample (Matsuura *et al.*, 1996; Ravi Kumar & Veeraiah, 1998; Majid & Arof, 2007). QMT defines that the polarons (in this work they are made up of protons and their stress fields) are able to tunnel through the potential barrier that exists between two possible complexation sites.

**Table 4.6:** Comparison of parameters obtained from fit of the experimental data to Eq. 8 for (a) sample membranes with different glycerol content at room temperature, 300 K and (b) sample membrane OG60 at various temperatures.

(a)	Membrane	$\zeta_{dc}$	$A$	$s$
	OG10	$8.13 \times 10^{-7}$	$1.00 \times 10^{-12}$	0.88
	OG20	$2.09 \times 10^{-6}$	$1.05 \times 10^{-12}$	0.89
	OG30	$6.45 \times 10^{-6}$	$1.80 \times 10^{-12}$	0.91
	OG40	$8.71 \times 10^{-6}$	$1.12 \times 10^{-12}$	0.91
	OG50	$2.82 \times 10^{-5}$	$1.60 \times 10^{-12}$	0.91
	OG60	$9.12 \times 10^{-5}$	$2.00 \times 10^{-12}$	0.91
(b)	Temperature (K)	$\zeta_{dc}$	$A$	$s$
	300	$9.12 \times 10^{-5}$	$2.00 \times 10^{-12}$	0.91
	303	$9.94 \times 10^{-5}$	$2.00 \times 10^{-12}$	0.91
	313	$1.33 \times 10^{-4}$	$2.20 \times 10^{-12}$	0.91
	323	$2.12 \times 10^{-4}$	$2.00 \times 10^{-12}$	0.91
	333	$2.74 \times 10^{-4}$	$2.00 \times 10^{-12}$	0.91
	343	$4.13 \times 10^{-4}$	$2.00 \times 10^{-12}$	0.91
	353	$5.49 \times 10^{-4}$	$2.20 \times 10^{-12}$	0.91
	363	$6.64 \times 10^{-4}$	$2.00 \times 10^{-12}$	0.91
	373	$7.95 \times 10^{-4}$	$2.00 \times 10^{-12}$	0.91

#### 4.3.3 Electrical Analyses for System II

The real part of complex dielectric function permittivity,  $\epsilon_r$  of plasticized chitosan based sample decreases non-linearity with the increase of frequency which can be seen in Fig. 4.25. The gradual decrease in  $\epsilon_r$  values at high frequencies confirms the contribution of polymeric molecular polarization and ionic conduction processes to the

dielectric dispersion, whereas the large increase in  $\epsilon_r$  with decreases of frequency is owing to the electrode polarization (Choudhary & Sengwa, 2011). Since the charge is made up of protons ( $H^+$ ), the increase in dielectric constant at high frequency region for different amounts of oxalic acid in Fig. 4.25 represents the increase in the number of  $H^+$ . The dielectric constant can be estimated at higher frequency as it becomes frequency independent above  $10^5$  Hz. The estimated dielectric constant values in ascending order from Fig. 4.25 are 7.99, 9.38, 10.86, 11.96, 13.40 and 18.41 for OG10, OG20, OG30, OG40, OG50 and OG60 respectively.

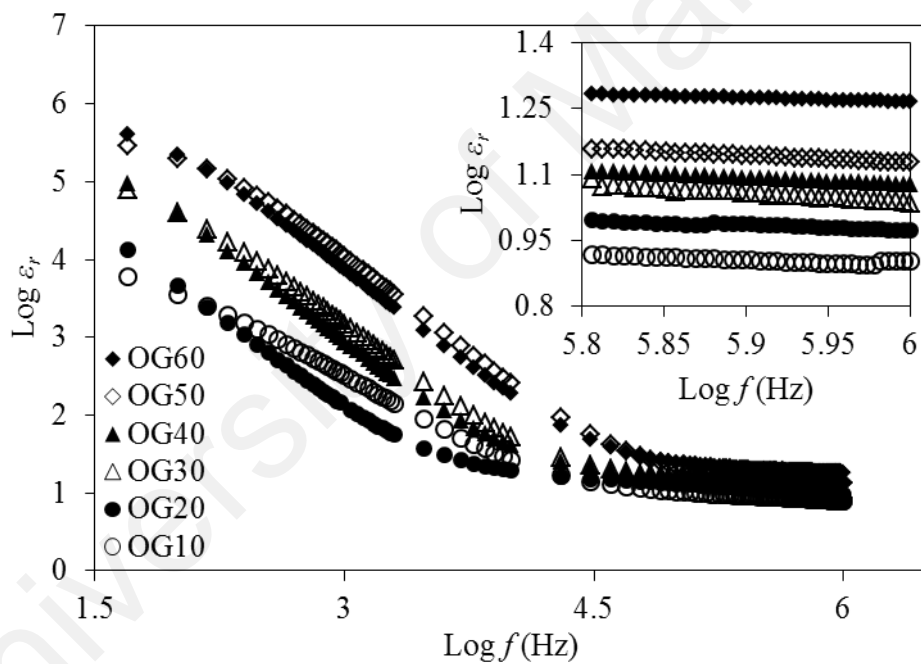


**Figure 4.25:** The dielectric constant,  $\epsilon_r$  for samples with different amount of glycerol versus  $\log f$  at room temperature, 300 K (the inset shows the enlarged plot at high frequencies).

The relationship between conductivity values and dielectric constant can be summarized in Fig. 4.26 with OG60 displaying the highest ionic conductivity at room temperature along with the highest dielectric constant value. Consequently the polarization effect of the highest conducting sample membrane OG60 cannot be examined due to some factors such as the nonlinearity of available resistive standards,

the limitation of the electrical leads, cell geometry, connectors. This limitation affected the impedance data at high frequency as stated by McKubre & Macdonald (2005) and Stewart and co-workers (1993).

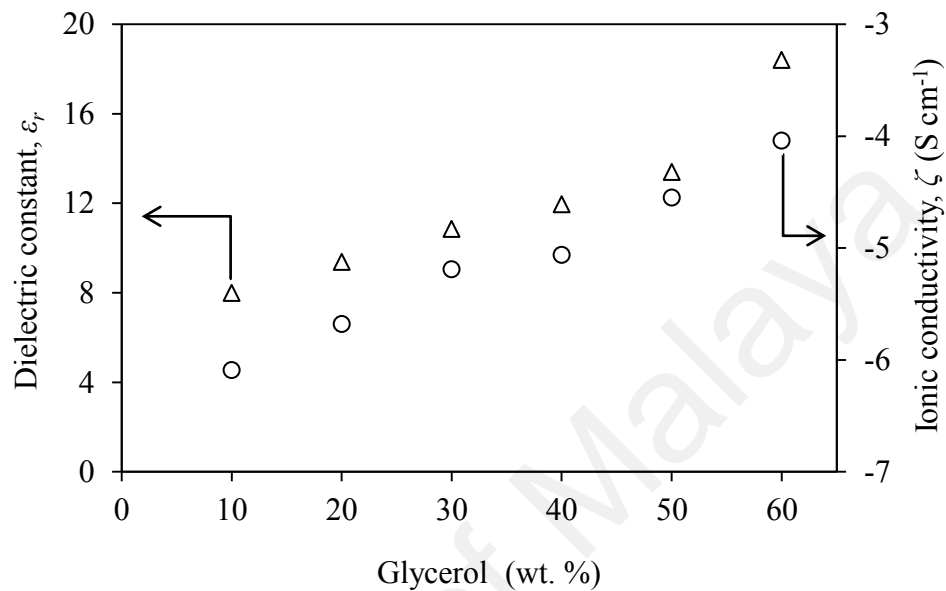


**Figure 4.26:** Glycerol dependence of dielectric constant,  $\epsilon_r$  and ionic conductivity at room temperature, 300 K.

The dipole relaxation in System II is examined by using Eq. 4.11 in order to calculate the dielectric loss tangent ( $\tan \delta$ ). The variation of loss tangent as a function of frequency for chitosan incorporated with various glycerol contents at room temperature is presented in Fig. 4.27. At low frequencies,  $\tan \delta$  increases with frequency because the active component (ohmic) is more dominant than the reactive component (capacitive) (Woo *et al.*, 2012; Chopra *et al.*, 2003). As the operating frequency is approaching 1 MHz, the peaks of  $\tan \delta$  in Fig. 4.27 are observed to decrease with frequency because the ohmic portion is independent of frequency and the reactive component grows in proportion to the frequency. The appearance of resonance peaks with increasing frequency was also observed. The maxima of  $\tan \delta$  in Fig. 4.27 shifts from 3 kHz to 39 kHz as glycerol content is increased indicates the increment in number of charge carriers for conduction which reducing the resistivity of the samples (Majid & Arof,

2007). The shift towards higher frequency verifies the reduction of the relaxation time in OG60.

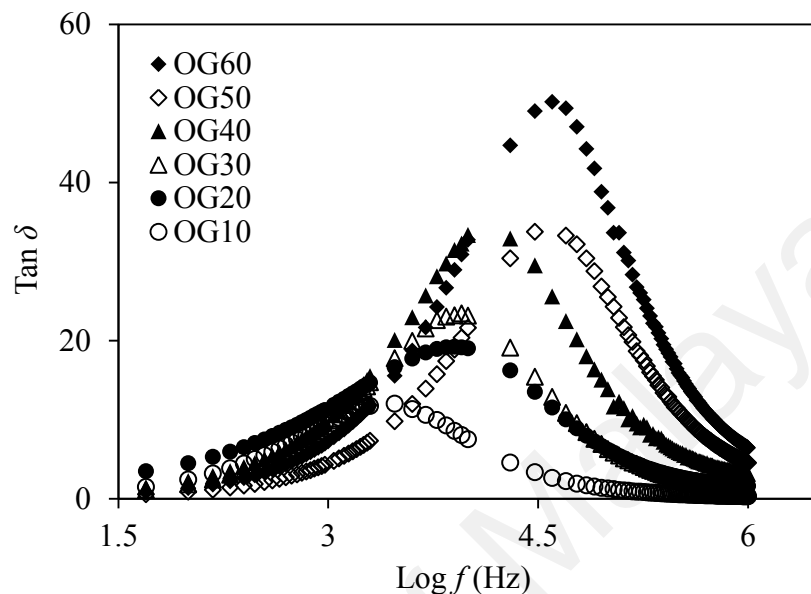


**Figure 4.27:** Variation of  $\tan \delta$  with frequency for sample with different amount of plasticizer glycerol at room temperature, 300 K.

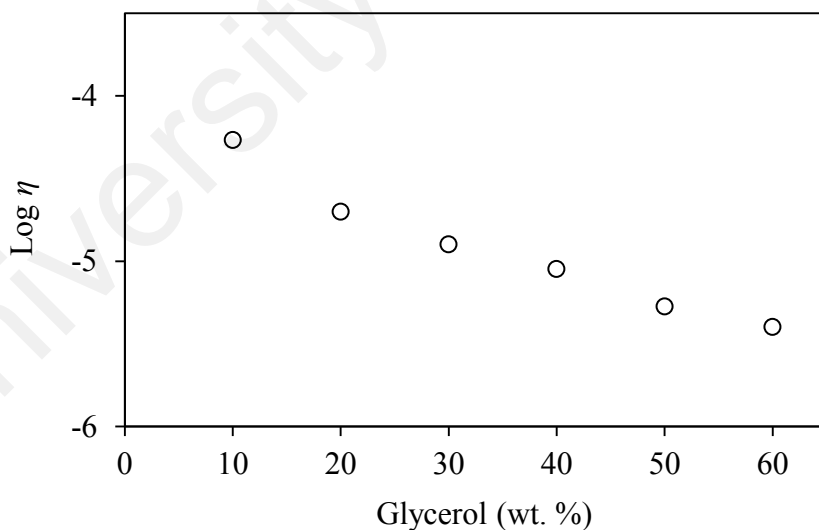


**Figure 4.28:**  $\text{Log } \eta$  versus amount of glycerol (wt. %).

By taking Debye equation in an ideal case, and assuming the static dielectric constant and high frequency dielectric constant is almost the same, the relaxation time,  $\eta$  can be calculated and depicted in Fig. 4.28. The plot of relaxation time  $\eta$  as a

function of glycerol content is shown in Fig. 4.28 with OG60 exhibiting the lowest value of  $3.98 \times 10^{-6}$ . The  $\tan \delta$  peaks are observed to shift towards higher frequency region with increasing amount of glycerol until 60 wt. % with reduction in relaxation time  $\eta$  as shown in Fig. 4.28.

#### 4.4 Summary

The impedance studies on both systems show that:

- The highest conductivity value at room temperature 300 K for System I is  $4.95 \times 10^{-7} \text{ S cm}^{-1}$  (featured by OA40) and the value is increased to maximum of  $9.12 \times 10^{-5} \text{ S cm}^{-1}$  (featured by OG60) when glycerol is introduced as plasticizer in System II. The bulk resistance for OA40 and OG60 are  $4.56 \times 10^3 \text{ } \Omega$  and  $94 \text{ } \Omega$  respectively.
- The activation energy,  $E_A$  for sample OA40 in System I is 0.61 eV and the value decreased to 0.30 eV for the highly plasticized sample OG60 in System II.
- The dielectric constant value of OA40 increased from 7.44 to 18.41 with addition of 60 wt. % of glycerol (OG60).
- Both System I and System II fit the quantum-mechanical tunnelling (QMT) model for the *ac* conduction mechanism.
- The lowest relaxation time  $\eta$  obtained for System I is  $5.27 \times 10^{-5}$  (shown by OA40), whereas OG60 exhibited the lowest value of  $3.98 \times 10^{-6}$  in System II.
- The activation energy for relaxation,  $E_B$  for sample OA40 in System I is calculated to be 0.61 eV.

# CHAPTER 5

## FOURIER TRANSFORM INFRARED SPECTROSCOPY ANALYSES

### 5.1 Introduction

Infrared (IR) spectroscopy provides a simple and fast technique that can give evidence for the presence of various functional groups. IR spectroscopy depends on the interaction of molecules or atoms with electromagnetic radiation. IR radiation causes atoms and groups of atoms of organic compounds to vibrate with increased amplitude about the covalent bonds that connect them. However IR radiation does not have sufficient energy to excite electrons, as in the case when molecules interact with visible, ultraviolet, or higher energy forms of light (Solomon *et al.*, 2004, Banwell & McCash, 1994).

IR radiation region is in between  $3 \times 10^{12}$  and  $3 \times 10^{14}$  Hz and can be specified in frequency related units by wavenumber ( $\bar{\nu}$ ) measured in reciprocal centimeters ( $\text{cm}^{-1}$ ). The wavenumber is the number of cycle of the waves in each centimeter along direction of the light. The FTIR spectrometer utilizes Michelson interferometer which can split the radiation beam from IR source. The combined beams from a mobile mirror and a fixed mirror pass through the sample to the detector and are recorded as a plot of time versus signal intensity, called interferogram. The overlapping wavelengths and the intensities of their respective absorptions are then converted to a spectrum by applying a mathematical operation called Fourier transform.

There are many ways molecules can vibrate which give rise to a dipole change. Two atoms joined by a covalent bond can undergo a stretching vibration whereas three atoms can undergo stretching and bending vibrations. The stretching modes can be symmetric and asymmetric. Meanwhile the bending vibrations can be an in-plane (scissoring) and an out-plane (twisting).

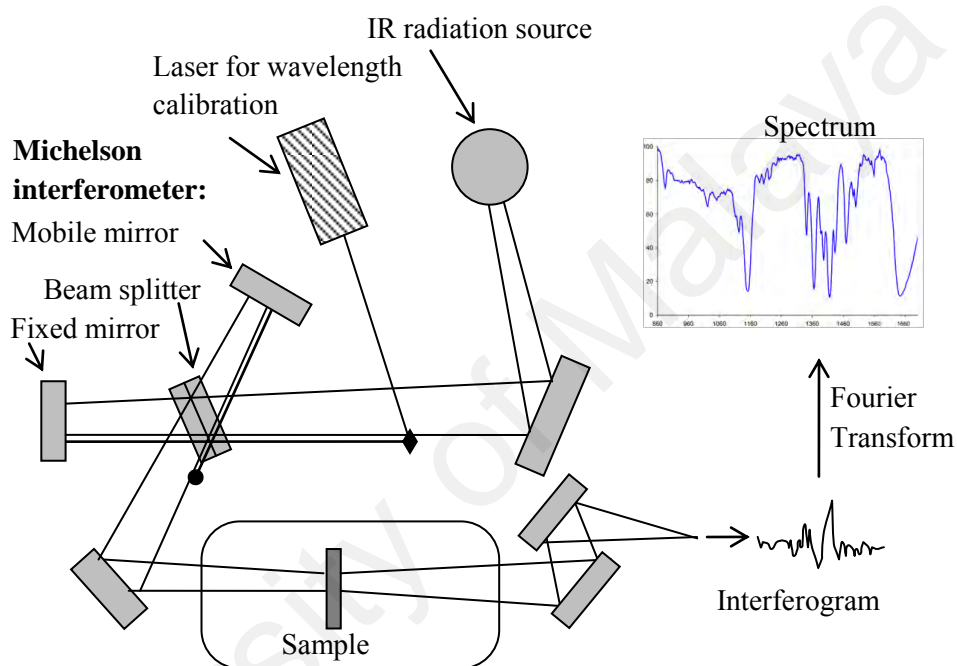


**Figure 5.1:** A schematic diagram of Fourier transform infrared (FTIR).

There are two factors determining the frequency of a stretching vibration in an IR spectrum; the masses of the bonded atoms and the relative stiffness of the bond. The former factor makes the light atoms to vibrate at higher wavenumber than the heavier ones. Hooke's law explained the best for the latter factor which makes the stiffer triple bonds appear at higher wavenumber compared to double bonds and single bonds. The dipole moment of the molecule must change as the vibration occurs in order for a vibration to occur with the absorption of IR energy. As an example, when the four hydrogen atoms in methane ( $\text{CH}_4$ ) vibrate symmetrically, methane does not give rise to

IR spectrum since it does not absorb IR energy. An IR spectrum has been called as a “fingerprint” of a molecule due to the characteristic or exclusive peaks of a particular molecule and the possibility of two different compounds to have the same spectrum is extremely small (Solomon & Fryhle, 2004, & Banwell & McCash, 1994).

The occurrence of an appreciable band shifts in the FTIR spectrum of the compounds with respect to the addition of each component, a distinct chemical interaction (hydrogen bonding or dipolar interaction) exist between the components. On the basis of the harmonic oscillator model, the reduction in force constant  $f$  can be represented by equation (5.1) (Pawlak *et al.*, 2003, Ma *et al.*, 2008):

$$\Delta f = f_b - f_{nb} = \frac{\nu\mu(\nu_b^2 - \nu_{nb}^2)}{4\pi^2} \quad (5.1)$$

where  $\mu = m_1m_2/(m_1 + m_2)$  correspond to the reduced mass of the oscillator,  $m_1, m_2$  being the masses of the two oscillators,  $\nu$  the oscillating frequency and  $f$  the force constant. The subscript  $b$  and  $nb$  denote bonded and non-bonded oscillators respectively. The reduction of force constant caused by some interaction is directly related to the frequency (or wavenumber) shift of stretching vibrations. Thus the lower the peak frequency after shifted, the stronger the interaction. Also the spectrum absorbance is dependent on the strength of the interaction. The vibrational modes and wavenumbers for chitosan, oxalic acid and glycerol are shown in Table 5.1.

**Table 5.1:** The vibrational modes and wavenumbers for chitosan, oxalic acid and glycerol.

Vibrational mode	Wavenumber (cm <sup>-1</sup> )	References
<b>(a) Chitosan</b>		
OH stretching	3456	Solomon & Fryhle (2004), Cui <i>et al.</i> , (2008); Leceta <i>et al.</i> , (2012)
NH <sub>2</sub> stretching	3367 (symmetric) 3315 (asymmetric)	Cui <i>et al.</i> , (2008), Baran (2008); Yalçinkaya <i>et al.</i> (2010)
NH <sub>3</sub> <sup>+</sup>	3200-3000	Gümüšoğlu <i>et al.</i> , 2011
CH stretching	2916 (symmetric) 2867 (symmetric)	Cui <i>et al.</i> (2008), Baran (2008); Yalçinkaya <i>et al.</i> (2010)
Amide I (C=O)	1649-1655	Rittidej <i>et al.</i> (2002), Cui <i>et al.</i> (2008), Baran (2008), Yalçinkaya <i>et al.</i> (2010); Leceta <i>et al.</i> (2012)
NH <sub>3</sub> <sup>+</sup>	1615	Rittidej <i>et al.</i> (2002)
NH <sub>2</sub> deformation	1587	Cui <i>et al.</i> (2008), Baran (2008); Yalçinkaya <i>et al.</i> (2010)
CH <sub>3</sub> deformation (in amide group)	1382 (symmetric)	Cui <i>et al.</i> (2008), Baran (2008); Yalçinkaya <i>et al.</i> (2010)
C–O–C vibration (in glycosidic linkage)	1150-1040	Pawlak <i>et al.</i> (2003), Cui <i>et al.</i> (2008), Baran (2008); Yalçinkaya <i>et al.</i> (2010)
<b>(b) Oxalic acid</b>		
C=O	1714-1730	Pawlak <i>et al.</i> (2003); Boczar <i>et al.</i> (2010)
COO <sup>-</sup> carboxylate band	1556	Rittidej <i>et al.</i> (2002)
OH stretching	1219 (asymmetric)	Boczar <i>et al.</i> (2010)
COOH scissoring	712	Boczar <i>et al.</i> (2010)
<b>(c) Glycerol</b>		
OH stretching	3300	Liu <i>et al.</i> (2013)
C–H stretching	2932 (symmetric) 2880 (asymmetric)	Liu <i>et al.</i> (2013); Gómez-Siurana <i>et al.</i> (2013)
C–H vibration	1416	Liu <i>et al.</i> (2013); Gómez-Siurana <i>et al.</i> (2013)
C–O stretching at C <sub>2</sub>	1117	Leceta <i>et al.</i> (2012); Gómez-Siurana <i>et al.</i> (2013)
C–O stretching at C <sub>1</sub> , C <sub>3</sub>	1045	Leceta <i>et al.</i> (2012)
C–C skeletal vibration	850, 925, 995	Leceta <i>et al.</i> (2012)

## 5.2 FTIR Studies for Chitosan- Oxalic acid system (System I)

FTIR spectra of chitosan, oxalic acid and the polymer electrolyte membranes are shown in Fig. 5.2. Parts of the same spectra on expanded scales are shown in Fig. 5.3 (from 3700 to 3000  $\text{cm}^{-1}$ ) and Fig. 5.4 (1800 to 1400  $\text{cm}^{-1}$ ). For chitosan (Fig. 5.2(a)), the broad peak around 3425 to 3390  $\text{cm}^{-1}$  is assigned to the overlapping of NH and OH stretching bands (Solomon & Fryhle, 2004). The symmetric and asymmetric stretching of C-H can be seen as the doublet peaks at 2929  $\text{cm}^{-1}$  and 2878  $\text{cm}^{-1}$ , the band due to the C=O of carboxamide (acetamido) appears at 1647  $\text{cm}^{-1}$  and N-H amine band appears at 1580  $\text{cm}^{-1}$ . The peaks at 1416  $\text{cm}^{-1}$  is attributed to C-N stretching coupled with N-H plane deformation, at 1376  $\text{cm}^{-1}$  is due to symmetric angular deformation of  $\text{CH}_3$ , at 1320  $\text{cm}^{-1}$  to C-N stretching of the amino group and at 1026  $\text{cm}^{-1}$  to the stretching vibration of C-O-C can also be observed in Fig. 5.2(a) (Pawlak *et al.*, 2003, Cui *et al.*, 2008, Baran, 2008, & Yalçinkaya *et al.*, 2010).

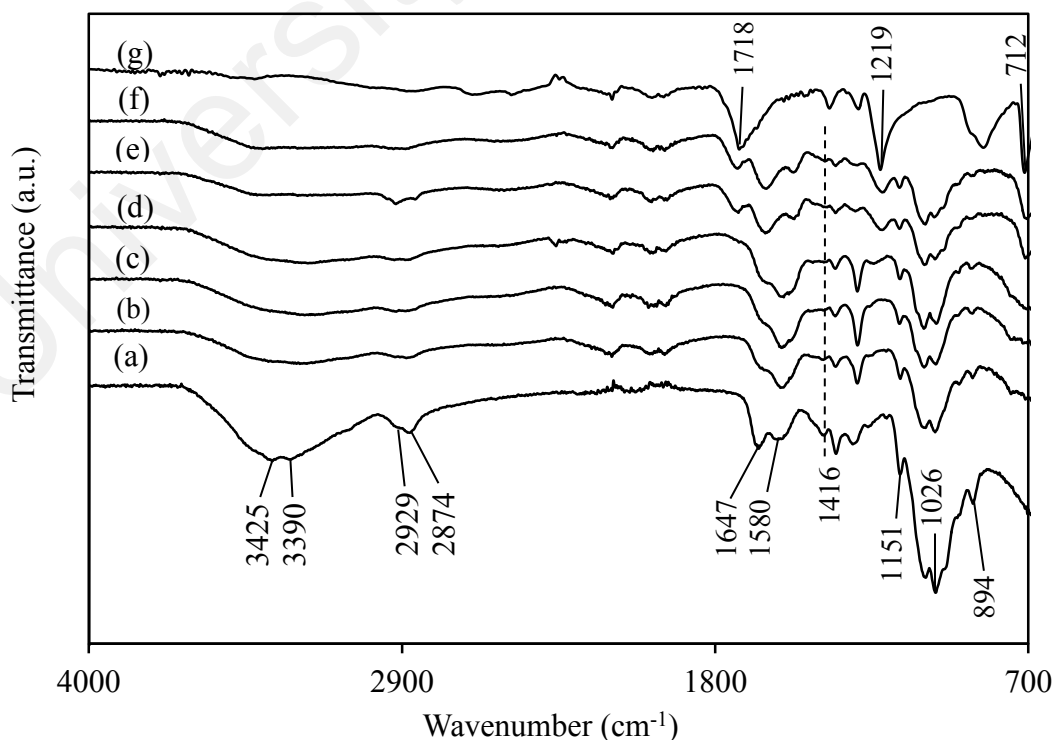


**Figure 5.2:** FT-IR spectra of (a) pure chitosan, (b) OA10, (c) OA20, (d) OA30, (e) OA40, (f) OA50, and (g) pure OA.

The moisture in oxalic acid was eliminated by heating. The FTIR spectrum obtained for oxalic acid is depicted in Fig. 5.2(g). The characteristic bands of oxalic acid appear at  $1718\text{ cm}^{-1}$  for free oxalic acid,  $1219\text{ cm}^{-1}$  for OH asymmetric stretching, and  $712\text{ cm}^{-1}$  for COOH scissoring asymmetric stretching (Boczar *et al.*, 2010). The polymer electrolyte membranes (Fig. 5.2(b-e)) show new peaks at  $\sim 1700\text{ cm}^{-1}$  and  $\sim 1190\text{ cm}^{-1}$  and the peak of N-H at  $1416\text{ cm}^{-1}$  become less intense as the amount of oxalic acid is increased (Cui *et al.*, 2008, Baran, 2008; Yalçinkaya *et al.*, 2010).

The complexation between oxalic acid (OA) and functional group of chitosan results in band shifting. The overlapping of NH and OH stretching bands (Fig. 5.3) were investigated by deconvoluting the infrared absorption between  $3000$  and  $3700\text{ cm}^{-1}$  using the OMNIC software. The characteristic bands between  $1400$  and  $1800\text{ cm}^{-1}$  (Fig. 5.4) were also deconvoluted. The absorbance peaks were fitted to a straight baseline using the Gaussian-Lorentzian function and the area of the deconvoluted bands were calculated.

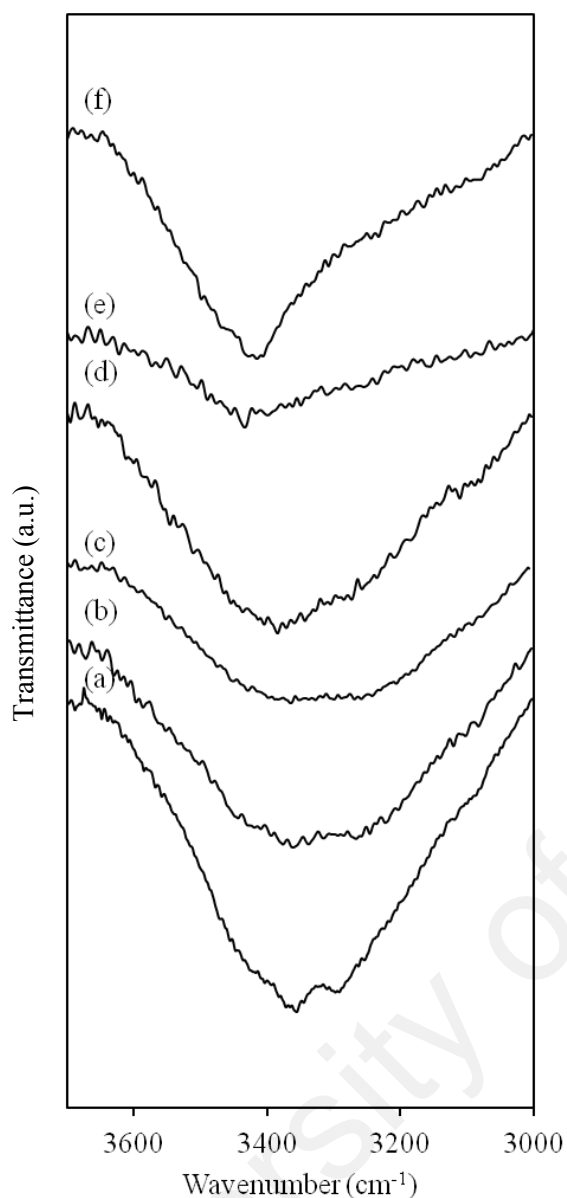


**Figure 5.3:** FTIR spectra in the range between 3700 and 3000  $\text{cm}^{-1}$  for (a) pure chitosan, (b) OA10, (c) OA20, (d) OA30, (e) OA40 and (f) OA50.

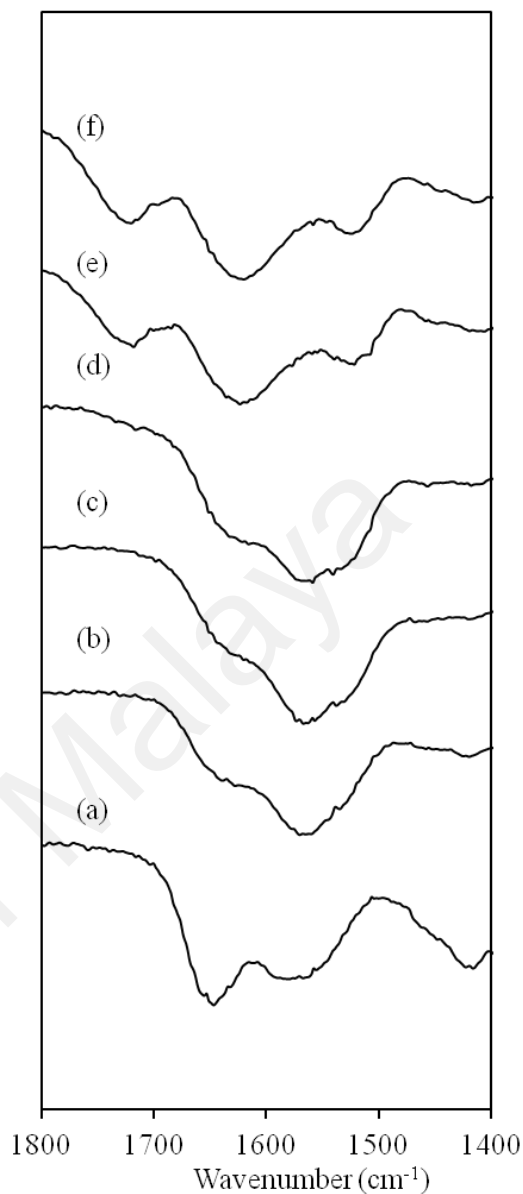


**Figure 5.4:** FTIR spectra in the range between 1800 and 1400  $\text{cm}^{-1}$  for (a) pure chitosan, (b) OA10, (c) OA20, (d) OA30, (e) OA40 and (f) OA50.

### 5.2.1 Deconvolution and band fitting of IR absorptions

The deconvolution for absorption area at higher wavenumber regions of the infrared spectroscopy is important in order to study the effect on hydroxyl and amine group with increasing OA concentration. The absorbance peaks were fitted to a straight baseline using the Gaussian-Lorentzian function and the area of the deconvoluted bands were calculated by using the OMNIC software.

The deconvolution of the characteristic bands between 3700 and 3000  $\text{cm}^{-1}$  are displayed in Fig. 5.6. As one can see in Fig. 5.6(a) the absorption band of free OH for chitosan at 3456  $\text{cm}^{-1}$  is shift upward to  $\sim 3500 \text{ cm}^{-1}$  as OA concentration is increased. The symmetric and asymmetric stretching bands for  $\text{NH}_2$  of chitosan shift to higher region from 3366 and 3250  $\text{cm}^{-1}$  to  $\sim 3414$  and  $\sim 3332 \text{ cm}^{-1}$  respectively. The shift from lower to higher wavenumber indicates that the hydrogen bonding involving N of amine ( $\text{NH}_2$ ) in chitosan becomes less. This is due to the protonation of amine to  $\text{NH}_3^+$  by oxalic acid hence reducing the electronegativity of the lone pair of N of amine ( $\text{NH}_2$ ). This result in diminishing of hydrogen bonding formation hence shifts the wavenumber to higher region.

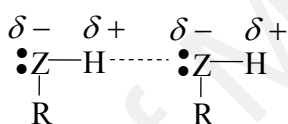


**Figure 5.5:** The scheme of hydrogen bonding occurrence. The Z atom is the electronegative atom such as O, N, & F (Solomon & Fryhle, 2004).

The hydrogen bonding is a strong dipole-dipole attraction that occurs between hydrogen to a strongly electronegative atom (oxygen, nitrogen, fluorine) and non-bonding electron pairs (lone pairs) on other electronegative atoms (Solomon & Fryhle, 2004). The hydrogen bonding interaction is illustrated in Fig. 5.5 and in this work, O and N atoms are represented as Z. The existence of a new peak at  $\sim 3203\text{-}3242 \text{ cm}^{-1}$  in Fig. 5.6(b-f) implies that the protonation of free amine  $\text{NH}_2$  of chitosan to  $\text{NH}_3^+$  (Gümüšoğlu *et al.*, 2011). The absorption band for hydrogen bonded hydroxyl (OH) group of chitosan at  $\sim 3100 \text{ cm}^{-1}$  shifted upward to  $3138 \text{ cm}^{-1}$  and almost diminished implying that the hydrogen bonded OH (of inter and/intramolecular chitosan polymer chain) become less with the increasing amount of oxalic acid (Solomon & Fryhle, 2004; Cui *et al.*, 2008).

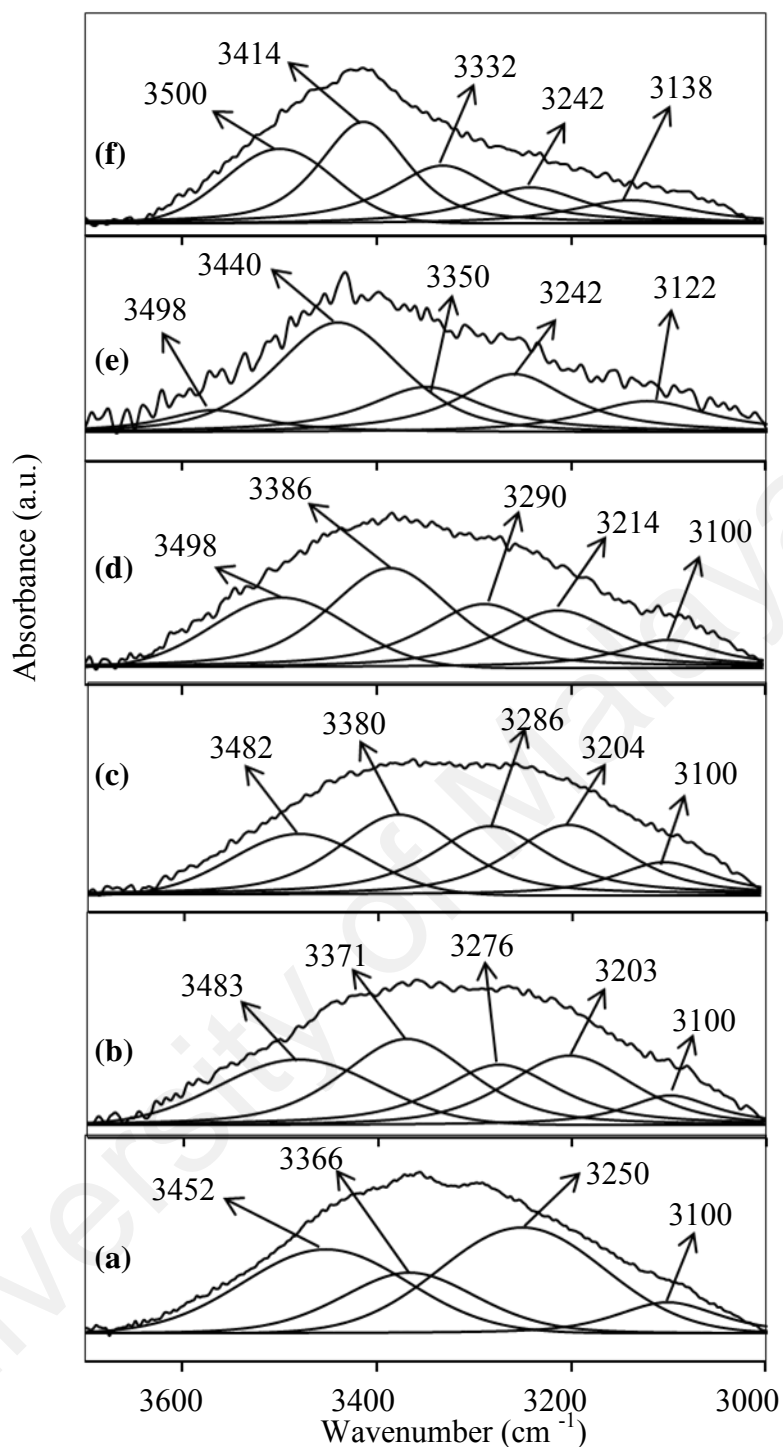


**Figure 5.6:** Deconvolution and band-fitting of IR spectra between 3700 and 3000  $\text{cm}^{-1}$  for (a) chitosan, (b) OA10, (c) OA20, (d) OA30, (e) OA40, (f) OA50.

This situation is likely to happen due to the decrement in number of electronegative atoms (i.e. N of amine) to form hydrogen bonding since amine groups  $\text{NH}_2$  in chitosan are becoming protonated as oxalic acid amount is increasing. The

deconvolution peaks of the characteristic bands between 3700 and 3000  $\text{cm}^{-1}$  from Fig. 5.6 are evaluated and tabulated in Table 5.2.

**Table 5.2:** Deconvolution of IR spectra between 3700 and 3000  $\text{cm}^{-1}$ .

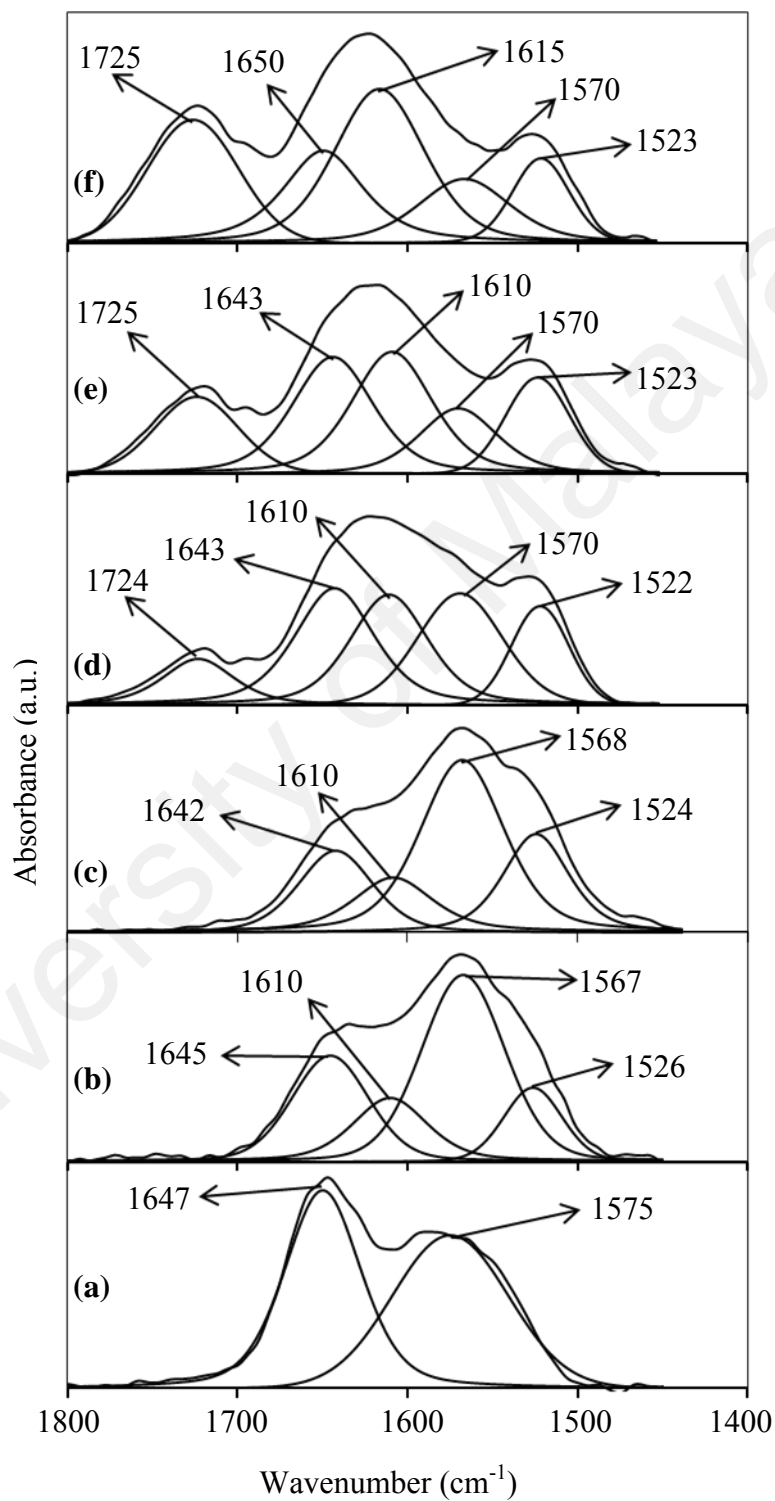
Sample membrane	Absorption band of free OH for chitosan	Symmetric stretching band for $\text{NH}_2$ of chitosan	Symmetric stretching band for $\text{NH}_2$ of chitosan	$\text{NH}_3^+$ (protonated amine $\text{NH}_2$ )*	Hydrogen bonded hydroxyl (OH) group of chitosan
Chitosan powder	3452	3366	3250	-	3100
OA10	3483	3371	3276	3203	3100
OA20	3482	3380	3286	3204	3100
OA30	3498	3386	3290	3214	3100
OA40	3498	3440	3350	3242	3122
OA50	3500	3414	3332	3242	3138

\* According to Gümüsoğlu *et al.*, 2011

The deconvolution of the characteristic bands between 1400 and 1800  $\text{cm}^{-1}$  are displayed in Fig. 5.7. The absorption peaks of  $\text{NH}_2$  bending and the carbonyl stretching carboxamide group are observed to downshift from 1575 to  $\sim 1559$   $\text{cm}^{-1}$  and from 1647 to  $\sim 1640$   $\text{cm}^{-1}$  respectively. Other absorption peaks at 1526  $\text{cm}^{-1}$  for  $\text{COO}^-$  from oxalic acid dissociation,  $\sim 1610$   $\text{cm}^{-1}$  for  $\text{NH}_3^+$ ,  $\sim 1724$   $\text{cm}^{-1}$  for free carboxylic group from oxalic acid are also observed.

These peak assignments are in agreement with those of Yalcinkaya *et al.* (2010) and Ritthidej *et al.* (2002). The deconvolution peaks of the characteristic bands between 1800 and 1400  $\text{cm}^{-1}$  from Fig. 5.7 are evaluated and tabulated in Table 5.3. The areas under the deconvoluted IR absorption peaks of  $\text{NH}_3^+$  and  $\text{NH}_2$  plotted against oxalic acid concentration are shown in Fig. 5.8. The areas are given as percentages with respect to the total area under the parent peak. The membrane with 50 wt. % OA (OA50) shows the highest area for the  $\text{NH}_3^+$  peak, which means that some of the  $\text{NH}_2$  group in chitosan

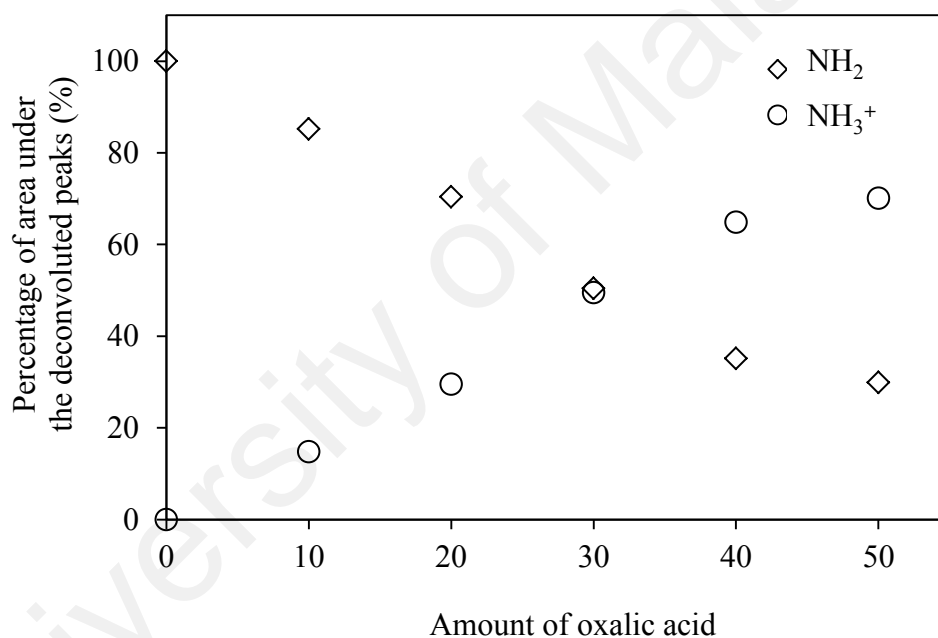
has been protonated. Because of this protonation the area under the  $\text{NH}_3^+$  peak has increased at the expense of the area under the  $\text{NH}_2$  peak.



**Figure 5.7:** Deconvolution and band-fitting of IR spectra between 1800 and 1400  $\text{cm}^{-1}$  for (a) chitosan, (b) OA10, (c) OA20, (d) OA30, (e) OA40, (f) OA50.

**Table 5.3:** Deconvolution of IR spectra between 1800 and 1400  $\text{cm}^{-1}$ .

Sample membrane	Absorption band of free carboxylic group from oxalic acid	Stretching mode for C=O of carboxamide	Absorption band of $\text{NH}_3^+$	Bending mode for $\text{NH}_2$ of chitosan	Absorption band of $\text{COO}^-$ for oxalic acid
Chitosan powder		1647	-	1575	-
OA10	-	1645	1610	1567	1526
OA20	-	1642	1610	1568	1524
OA30	1724	1643	1610	1570	1522
OA40	1725	1643	1643	1570	1523
OA50	1725	1650	1650	1570	1523

**Figure 5.8:** Variation of peak areas of  $\text{NH}_3^+$  and  $\text{NH}_2$  as a function of oxalic acid content.

### 5.3 FTIR Studies for Chitosan-Oxalic acid-Glycerol system (System II)

The most direct method to distinguish the molecular interaction for any system with polyol incorporation is to monitor the band shifts of certain functional groups as the hydrogen bonding changes are great of importance (Liu *et al.*, 2013). The hydrogen

associated functional groups such as –OH and –CH are convinced to be a more reliable indicator to interpret the interaction between glycerol and other functional groups.

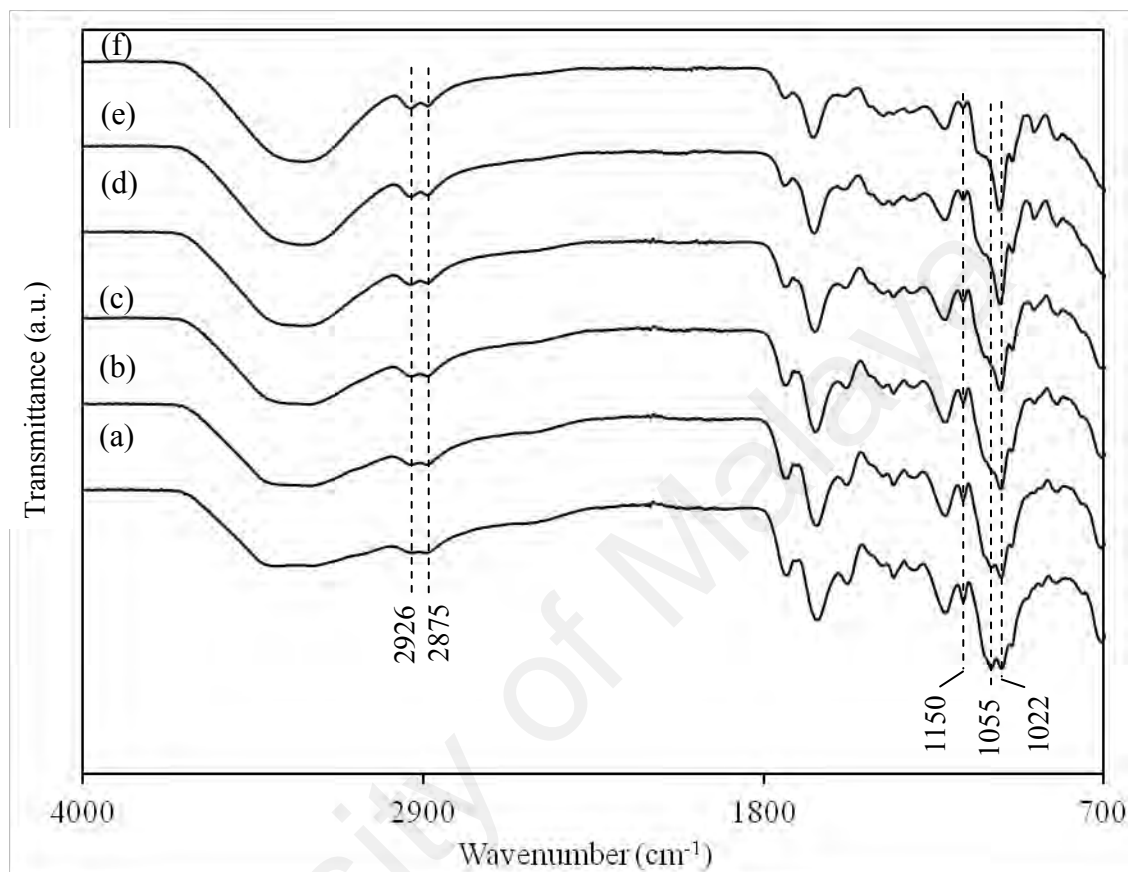


**Figure 5.9:** FT-IR spectra of (a) OG10, (b) OG20, (c) OG30, (d) OG40, (e) OG50, (f) OG60.

The FTIR spectra of the plasticized samples (OG10 to OG60) in Fig. 5.9 shows neither any significant changes nor any new peak occurrence. The visible changes that can be seen are shifts in peaks and decrement in peak intensities. The intensities of the overlapping peaks for NH and OH stretching vibration bands between 3200 and 3500  $\text{cm}^{-1}$  become broader as glycerol content is increased due to the increasing OH number from glycerol (Liu *et al.*, 2013, & Vicentini *et al.*, 2010).

The doublet peaks of symmetric and asymmetric stretching for C–H in chitosan at 2939 and 2882  $\text{cm}^{-1}$  respectively shift to higher wavenumber 2944 and 2890  $\text{cm}^{-1}$ .

The interaction between the plasticizer (glycerol) and C-H group become lesser as glycerol content is increased hence causing the peaks to appear at higher wavelength and become prominent as the force constant increased. This explanation is in agreement with Ma *et al.* (2008) and Pawlak *et al.* (2003).

The characteristic bands between 1800 and 1450  $\text{cm}^{-1}$  are observed to be weak or less intense. The addition of glycerol results in increasing of hydrogen bonding occurrence between OH (of glycerol) and  $\text{NH}_2$ ,  $\text{NH}_3^+$ , C=O of carboxamide group and free oxalic acid (refer to section 5.2).

The hydrogen bonding effect with increasing content of glycerol can also be seen for COC glycosidic linkage band in the range from 1150 to 1040  $\text{cm}^{-1}$ . The absorption peak at 1150  $\text{cm}^{-1}$  becomes less pronounced and the disappearance of peak at 1055  $\text{cm}^{-1}$  suggests interactions between glycosidic linkage and glycerol (Leceta *et al.*, 2012, Pawlak *et al.*, 2003). The absorption peak at 1022  $\text{cm}^{-1}$  becomes more noticeable and shifts to a higher wavenumber 1030  $\text{cm}^{-1}$  as glycerol content is increased.

#### 5.4 Summary

The Fourier transform infrared spectroscopy studies on both systems show that:

- From the deconvolution study on System I, the intensity of  $\text{NH}_3^+$  peak at 1610-1615  $\text{cm}^{-1}$  and  $\text{COO}^-$  peak at 1724  $\text{cm}^{-1}$  increased with amount of oxalic acid.
- The area under the  $\text{NH}_3^+$  peak has increased with the content of oxalic acid whereas the area under the  $\text{NH}_2$  peak is decreasing indicating that the amine group of chitosan is being protonated.

- The interaction between the plasticizer (glycerol) and C–H group results in the shift of the doublet peaks of symmetric and asymmetric stretching for alkyl group in chitosan (C–H) at 2939 and 2882  $\text{cm}^{-1}$  upward to 2944 and 2890  $\text{cm}^{-1}$ .
- In this work, FTIR is an important tool in detecting the functional groups and determining the interactions in electrolyte membranes consisting of chitosan, oxalic acid and plasticizer glycerol. These interactions can be seen from the band shifts as concentration of oxalic acid increased for bending mode for  $\text{NH}_2$  of chitosan from 1575 to 1575  $\text{cm}^{-1}$ , the presence of a new peak for protonated amine  $\text{NH}_3^+$  at  $\sim 1610$ . The prominent changes in the peak intensities of FTIR spectra can be seen for NH and OH stretching vibration between 3200 and 3500  $\text{cm}^{-1}$  as concentration of glycerol increased.

# CHAPTER 6

## X-RAY DIFFRACTION ANALYSES

### 6.1 Introduction

X-ray diffraction (XRD) is the most widely used and least ambiguous method for the precise determination of the positions of atoms in molecules and solids (Shriver *et al.*, 1994). It is also widely used as a means of characterizing materials of all forms (Kumirska *et al.*, 2010). A typical x-ray diffractometer consists of an x-ray source with a fixed wavelength, a goniometer for mounting the sample and an x-ray detector as shown in Fig. 6.1. A crystal is mounted on the goniometer and gradually rotated while being bombarded with x-rays, producing a diffraction pattern of regularly spaced spots known as reflections. The two-dimensional images taken at different rotations are converted into a three dimensional model of the density of electrons within using the mathematical method of Fourier transforms, combined with the chemical data obtained for the sample.

The pioneer crystal studies on chitin and chitosan were reported in 1937 using XRD (Kumirska *et al.*, 2010). The x-ray patterns were obtained by passing the x-ray beam perpendicular and parallel to surface of the chitin sheet. They also examined the diffractograms of chitin fibres, ground chitin, the precipitation from the reaction between chitin and some chemicals; hydrochloric acid, lithium thiocyanate, nitric acid and sodium hydroxide.

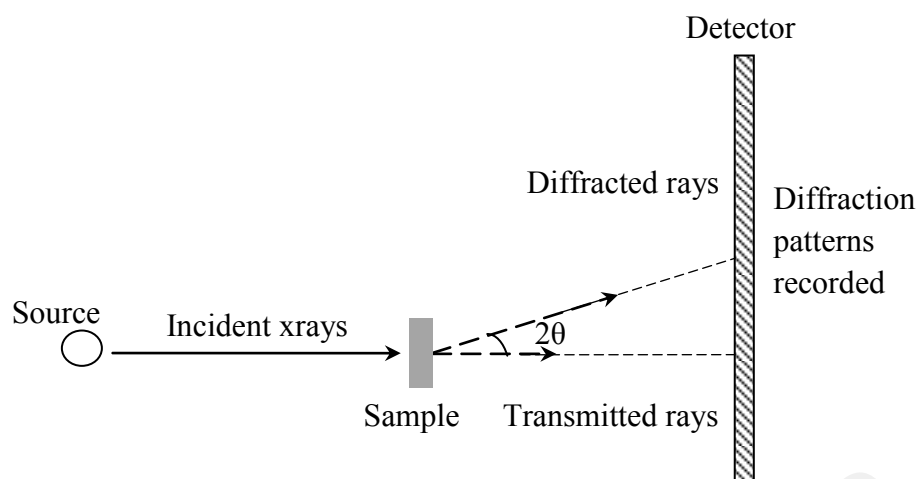


**Figure 6.1:** A schematic diagram of an x-ray diffractometer.

Chitosan was produced by hydrolysis reaction of chitin in sodium hydroxide solution and the investigation of the diffraction patterns was done at interval reaction times (Kumirska *et al.*, 2010). The diffractograms were obtained by passing the x-ray beam perpendicular and parallel to surface of the chitosan sheet. The interference characteristics of chitin disappeared except one; which had shifted slightly. This shows that chitin had undergone major changes in the regularity of spacing in the particular direction after being treated in sodium hydroxide solution. A schematic diagram of an x-ray diffractometer can be seen in Fig. 6.1. The diffraction patterns of chitosan fibre and the addition compounds of chitosan with lithium thiocyanate and sodium hydroxide were also reported. The data suggested that the amide groups were hydrolysed. Present-day x-ray analyses on chitin and chitosan with their derivatives were carried out on an advanced x-ray diffractometer which is were mostly modifications of the ones used by Clark and co-workers (Kumirska *et al.*, 2010).

The properties of chitin and chitosan are depending mostly on molecular weight, polydispersity, degree of deacetylation and crystallinity. The XRD is able to measure the crystallinity degree of chitin and chitosan. In this work, XRD has been used to calculate

the crystallinity degree of chitosan with DD higher than 75 %. The parameters of chitin hydrolysis process in sodium hydroxide solution will determine the deacetylation degree (DD) of chitosan. The longer reaction time will produce chitosan with higher DD value. This chemical modification results in N-deacetylation of amide ( $-\text{NC}=\text{O}$ ) to amine ( $\text{NH}_2$ ). Zhang *et al.* (2005) reported the XRD patterns for chitosan with various DD values as high as 93 %. It is noted that the crystallinity value is decreasing as the DD value increased. The  $d$ -spacing changes in chitin can be seen for chitosan with higher DD values (50–93 %) which indicate the occurrence of expansions of the crystal lattices (compared to those of lower ones) and thus moved to wider diffraction angles. This is due to the less intermolecular bonding in chitosan with higher DD values (Zhang *et al.*, 2005).

In the present work chitosan (polymer host) was incorporated with various amounts of oxalic acid and glycerol (as plasticizer). The relative degree of crystallinity,  $\chi_c$  of each sample membrane can be calculated using the simplicity approach of the two-phase model from XRD pattern using the following equation (Hassan *et al.*, 2013 & Lewandowska *et al.*, 2011):

$$\chi_c = \frac{I_c}{I_c + I_A} \quad (6.1)$$

where  $I_c$  is the crystalline integrated intensity (area under the curve) of the peaks and  $I_A$  is amorphous integrated intensity of the halo.

## 6.2 XRD study for Chitosan–Oxalic acid system (System I)

The XRD patterns of crosslinked chitosan film with different amounts of oxalic acid are shown in Fig. 6.2. Chitosan–oxalic acid salt or chitosan–oxalate can be formed

when chitosan was dissolved in oxalic acid. In order to study the XRD patterns of chitosan powder and the crosslinked membranes, the XRD diffractograms were deconvoluted using non-linear least squares Origin 8.0 software to separate the crystalline peaks from the continuous scattering background. Fitting of multi-peaks using Gaussian distribution was done after carrying out baseline correction for the particular diffractogram.

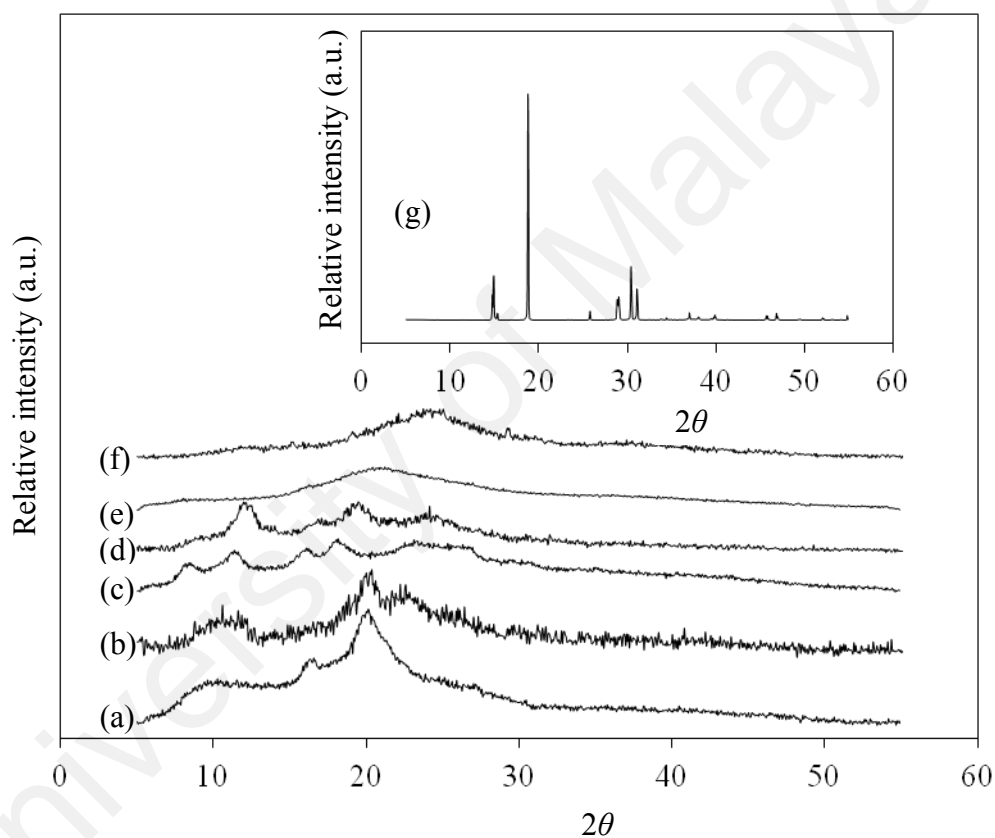


**Figure 6.2:** XRD patterns of (a) chitosan (b) OA10 (c) OA20 (d) OA30 (e) OA40 (f) OA50 (g) pure OA (inset).

XRD has been used to relate the crystallinity with degree of deacetylation (DD) of chitin by Zhang *et al.* (2005). They have reported that a peak of maximum intensity at  $2\theta \sim 9^\circ$  reflection is shifted to a higher angle with the increase of DD. A second intensive peak at  $2\theta \sim 19^\circ$  also diminished with the increase in DD. The positions of the peaks reported by Zhang *et al.* (2005) are in agreement with those reported by Pawlicka

*et al.* (2008). Since the degree of deacetylation of chitosan used in this research is higher than 75%, the crystalline peaks should be observed at higher  $2\theta$  angles when compared to those of the original peaks in chitin.

In our study, for pristine chitosan powder, three sharp peaks and two broad peaks are observed at  $2\theta$  angles of  $9.7^\circ$ ,  $16.4^\circ$  and  $20.2^\circ$  and  $19.7^\circ$  and  $38.1^\circ$  respectively (Pawlicka *et al.*, 2008 & Hassan *et al.*, 2013).

#### 6.2.1 Deconvolution of XRD patterns for Chitosan–Oxalic acid system (System I)

Feng *et al.*, (2012) reported that the XRD measurement of chitosan exhibits seven crystalline possible polymorphs: “tendon chitosan”, “annealed”, “1-2”, “L-2”, “form-II”, “form-II” (Feng *et al.*, 2012) and “8-fold right-handed” form (Kumirska *et al.*, 2008). In their works, all of the polymorphs (apart from the last one form) have the extended 2-fold helix configuration whereas the “8-fold right-handed” is easily converted into 2-fold helix due to its instability (Kumirska *et al.*, 2008). Pawlicka and co-workers (2008) reported that chitosan complexes show a wide variety of conformations compared to other polysaccharides. This is due to the regular distribution in the polymeric structure primary amino groups.

The x-ray diffractograms of chitosan powder and the ionic crosslinked membranes with their deconvoluted peaks are shown in Fig. 6.3. The first and second crystalline peaks in the crosslinked membranes are found to be at  $8\text{--}13^\circ$  and at  $19\text{--}25^\circ$  respectively. A new peak is observed for the sample OA50 at  $2\theta \sim 36^\circ$  suggesting the presence of local ordering, due to the excess content of oxalic acid. Thus the lowest crystallinity is expected for the OA40 membrane.

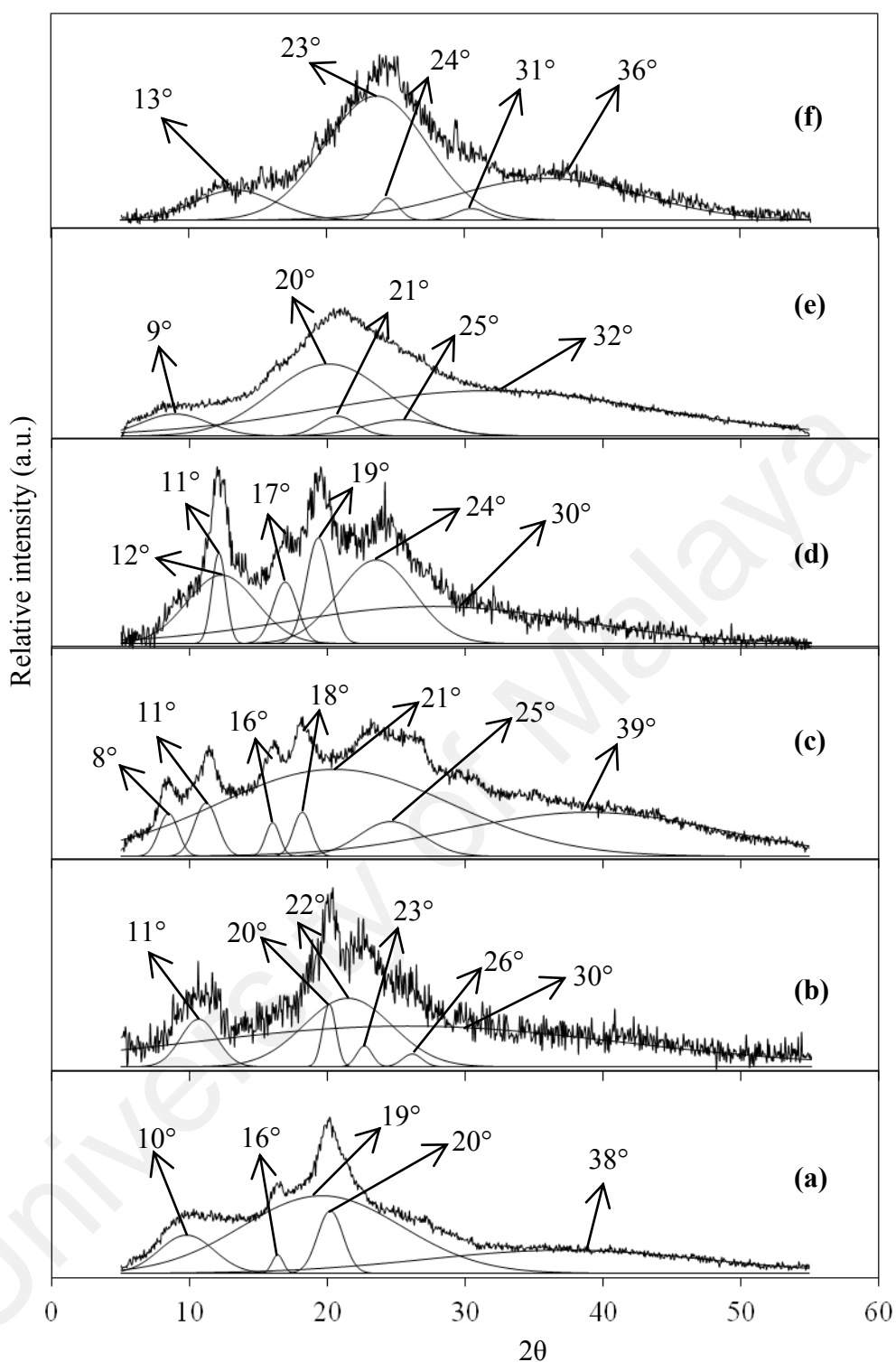


**Figure 6.3:** The deconvolution of XRD patterns of (a) chitosan, (b) OA10, (c) OA20, (d) OA30, (e) OA40, (f) OA50.

The degree of crystallinity and conductivity values were tabulated in Table 6.1.

It can be seen that OA40 membrane shows the lowest degree of crystallinity of 13 % (corresponding to the highest degree of amorphousness) giving the highest ionic

conductivity value. In comparison, the pristine chitosan powder has a higher crystallinity degree of 17 %. The reduction in degree of crystallinity with the addition of oxalic acid might be due to the increase of amine protonation in chitosan to  $R-NH_3^+$  hence diminishing the possibility for hydrogen bond between O at C-3 or O-5 and H of amine group ( $R-NH_2$ ). The numbering position of chitosan is shown in Fig. 6.4.

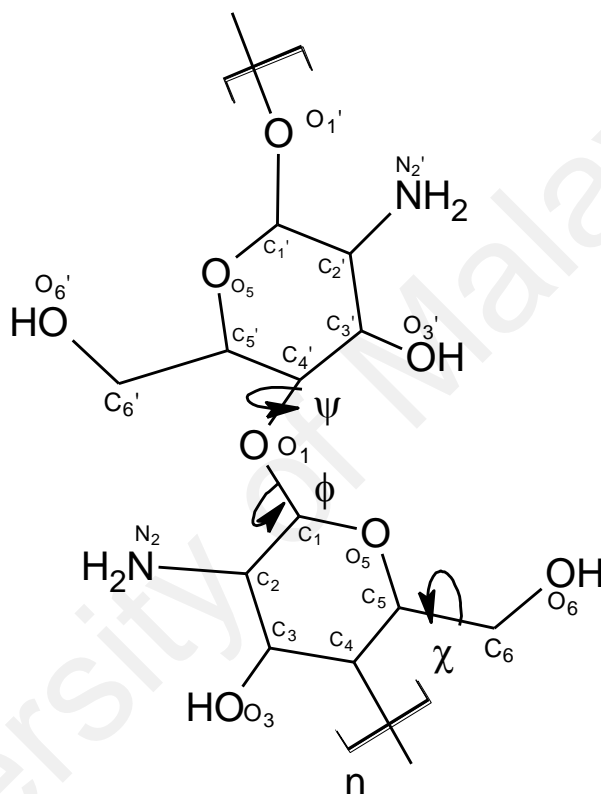


**Figure 6.4:** Chemical structure of chitosan, showing position numbering. The two angles  $\Psi$  and  $\Phi$  define the chain conformation, and the angle  $\chi$  define the O-6 orientation (redrawn from Muzzarelli *et al.*, 2012).

This explanation is in an agreement with the FTIR results since the symmetric and asymmetric stretching bands for  $NH_2$  of chitosan shift to high region from 3366 to  $\sim 3414\text{ cm}^{-1}$  and 3250 to and  $\sim 3332\text{ cm}^{-1}$  as oxalic acid contents increased. In addition, the decreasing peak area at  $1575\text{ cm}^{-1}$  attributed to  $NH_2$  deformation was observed as oxalic acid content is increased. The existence of new peak at  $1610\text{ cm}^{-1}$  confirming the protonation of amine  $NH_2$  group to  $NH_3^+$  (Rittedej *et al.*, 2012).

**Table 6.1:** Room temperature conductivity value and degree of crystallinity of chitosan and the crosslinked membranes.

Sample name	Conductivity, $\sigma$ (S cm <sup>-1</sup> ) at room temperature (300 K)	Degree of crystallinity, $\chi_c$ (%)
Chitosan	-	17
OA10	$2.81 \times 10^{-9}$	16
OA20	$1.27 \times 10^{-8}$	15
OA30	$2.01 \times 10^{-8}$	14
OA40	$4.95 \times 10^{-7}$	13
OA50	$6.26 \times 10^{-9}$	14

### 6.3 XRD study for Chitosan–Oxalic acid–Glycerol system (System II)

The addition of glycerol is expected to modify the rigid structure of the chitosan films by destroying the intermolecular hydrogen bonds between the polysaccharide chains, and at the same time they can form new hydrogen bonds with chitosan. This leads to the increment of mobility of the polymer chains (Lazaridou *et al.*, 2012). In chitosan, the carboxamide  $-C=O$  (acetamide) group exists in particular amount, depending on the degree of deacetylation. The carboxamide group plays an important role in the formation of intermolecular bonds between adjacent chains. Liu *et al.* (2013) and Cervera *et al.* (2004) observed that the addition of glycerol in polymer results in x-ray patterns shift. The addition of glycerol reduced the crystallinity in chitosan based membranes. This situation was likely due to the interaction between glycerol molecules and carboxamide group of chitosan by hydrogen bonds, which prevent the carboxamide groups from forming intermolecular chain hydrogen bonds with other chitosan molecules. This leads to breakdown of the intermolecular connectivity between the polysaccharide chains (Domjan *et al.*, 2009).

The interaction between glycerol and chitosan has been carried out by Domjan *et al.* (2009) using density functional theory calculations on a simplified model system with the Gaussian 03 software package. The polysaccharide chain was modeled by one acetylglucosamine unit with carboxamide group. Although the model system is very small, it represents the important part of the chain from the aspect of the hydrogen bonded network structure. The applied basis set describes the H-bonds with good accuracy, but the calculated energy values were not used because of the simplified model system. The formation of hydrogen bonds between glycerol molecule and the carboxamide group of chitosan is shown in Fig.6.5.

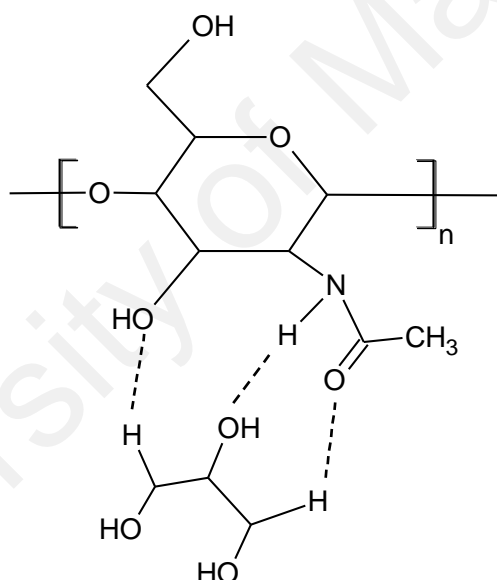


**Figure 6.5:** Hydrogen bonds interaction between glycerol and carboxamide group of chitosan (redrawn from Domjan *et al.*, 2009).

Glycerol reduces the extent of chitosan second-order interactions which are responsible for crystallinity in chitosan without altering their fundamental chemical character (Fundo *et al.*, 2014). The broadness of the peaks in the x-ray diffractograms (Fig. 6.6) implied increase in amorphous region. Pawlicka and co-workers (2008)

reported work on plasticized chitosan/HCl samples in which the addition of plasticizer glycerol and sorbitol promotes a considerable increase in amorphous phase.

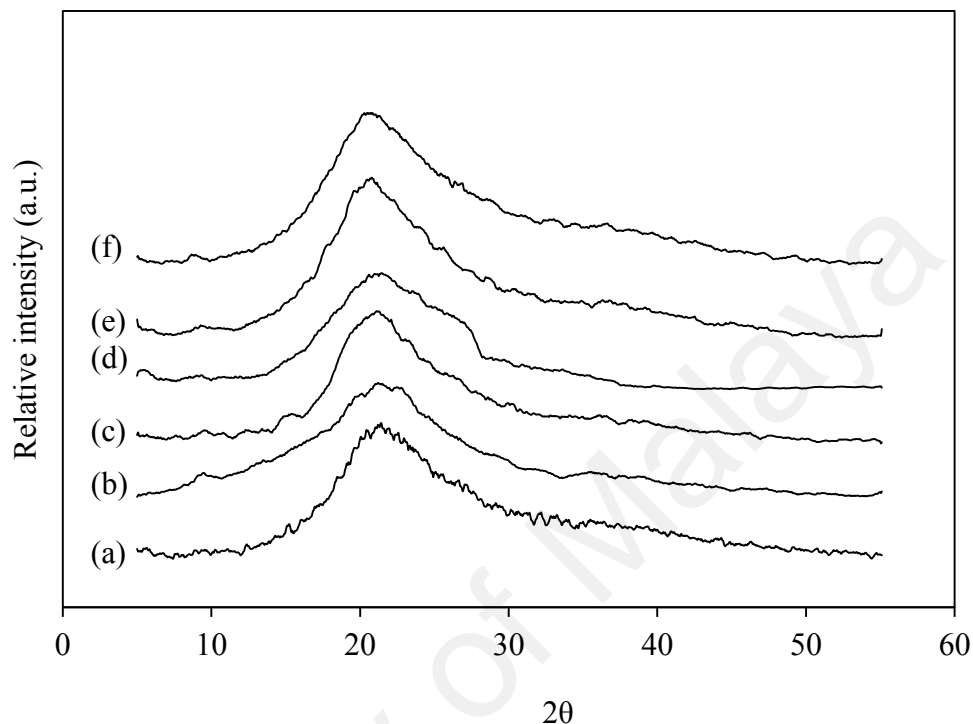


**Figure 6.6:** Xray diffractograms of the plasticized sample membranes (a) OG10 (b) OG20 (c) OG30 (d) OG40 (e) OG50 (f) OG60.

### 6.3.1 Deconvolution of XRD patterns for Chitosan–Oxalic acid–Glycerol system (System II)

The deconvoluted x-ray patterns of OA40 was taken as the reference and all of the OG sample membranes were deconvoluted accordingly using Origin 8.0 software by fitting of multi-peaks using Gaussian distribution. All of the deconvoluted peaks were shown in Fig. 6.7.

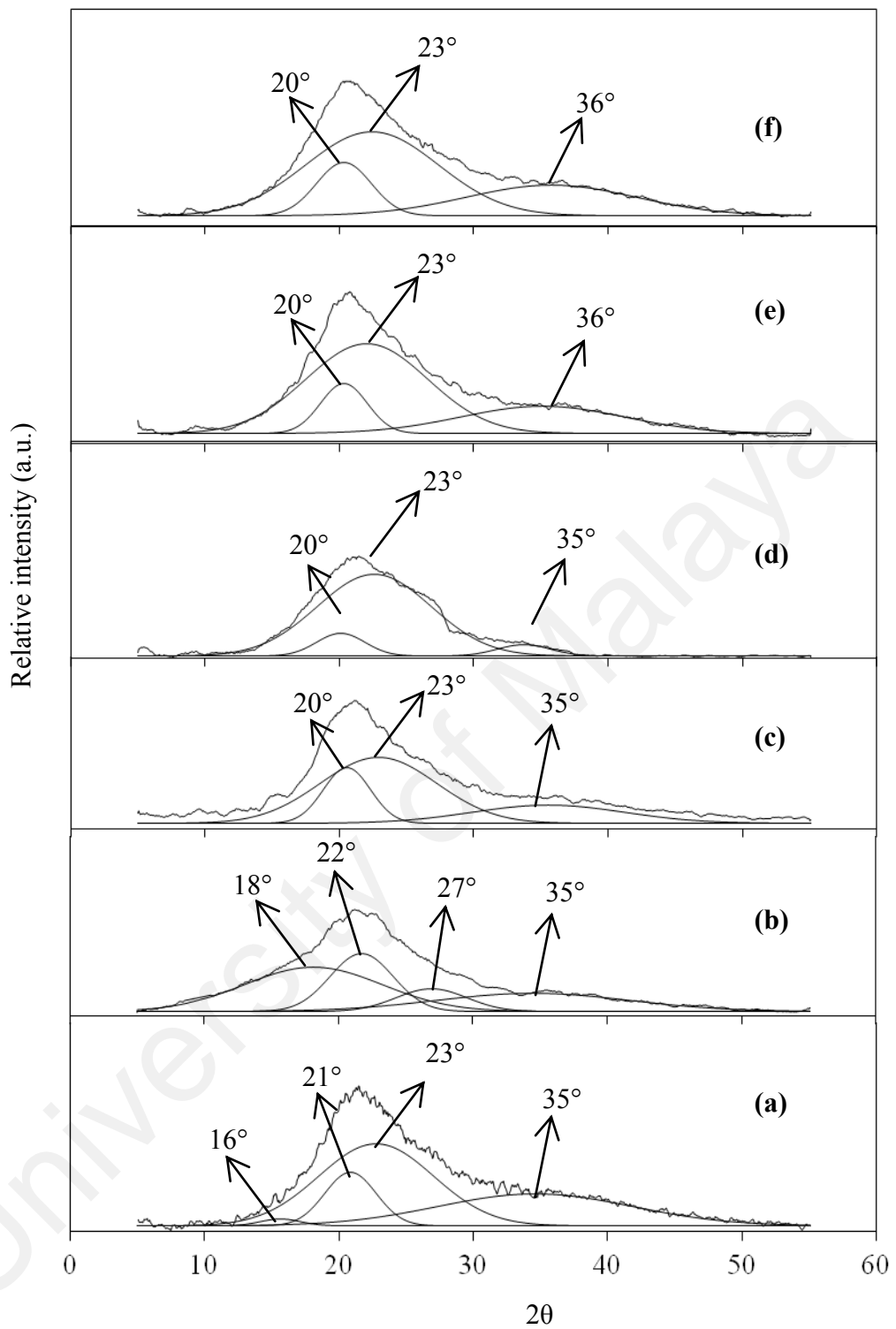


**Figure 6.7:** The deconvolution of XRD patterns of (a) OG10 (b) OG20 (c) OG30 (d) OG40 (e) OG50 (f) OG60.

Liu *et al.*, (2013) stated that the low amount of glycerol results in anti-plasticization effect. They reported that the addition of glycerol lower than 2.5 % caused the degree of crystallinity to increase and the higher glycerol contents (i.e. 5.0 % and

10.0 %) make the membranes exhibit lesser crystallinity. In this work, a sudden increase in degree of crystallinity can be seen in sample membranes with 10 - 40 wt % of glycerol (OG10-OG40). This proved that at low glycerol concentrations more hydrogen bonding occurred between glycerol and chitosan. The reason behind this situation is likely due to strong hydrogen attraction between glycerol molecules at low content (Liu *et al.*, 2013). The degree of crystallinity patterns of System II can be explained as follow:

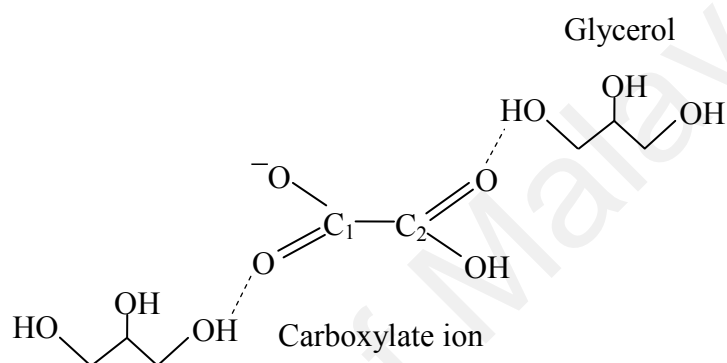


**Figure 6.6:** The possible attraction between carboxylate ions and glycerol based on XRD results.

The hydrogen attraction between H of glycerol and O of carbonyl C<sub>1</sub> oxalate ion results in reduction of electron density of O<sup>-</sup> (at C<sub>1</sub> side) thus minimizes the ionic interaction (Coulombic force) between carboxylate ion and the protonated amine NH<sub>3</sub><sup>+</sup> to occur. The polymer becomes more flexible with the enhancement of bond rotations which leads to the increment of mobility of the polymer chains (Mubarak *et al.*, 2013; Selvasekarapandian *et al.*, 2005; Sudhakar and Selvakumar, 2012; Lazaridou *et al.*, 2012) at high glycerol contents (50 and 60 wt % glycerol). Glycerol favours preferential interaction (i.e. hydrogen bonding) with O of carbonyl C<sub>2</sub> oxalate ion reduces the extent of hydrogen bonding interaction (Lavorgna *et al.*, 2010) between chitosan and oxalic acid. This interaction causes the H of hydroxyl group (at C<sub>2</sub> side) to be released easily

into proton  $H^+$  thus enhances the ionic conductivity in the plasticized sample membranes.

The degree of crystallinity and ionic conductivity values were calculated and tabulated in Table 6.2. The sample OG60 exhibits the lowest degree of crystallinity of 11 %.

**Table 6.2:** Room temperature conductivity value and degree of crystallinity of chitosan and the crosslinked membranes.

Sample name	Conductivity, $\sigma$ ( $S\ cm^{-1}$ ) at room temperature (300 K)	Degree of crystallinity, $\chi_c$ (%)
OG10	$8.13 \times 10^{-7}$	29
OG20	$2.09 \times 10^{-6}$	24
OG30	$4.68 \times 10^{-6}$	20
OG40	$8.71 \times 10^{-6}$	15
OG50	$2.82 \times 10^{-5}$	13
OG60	$9.12 \times 10^{-5}$	11

#### 6.4 Summary

The x-ray diffraction studies on both systems show that:

- In System I, the degree of crystallinity chitosan decreases with the addition of oxalic acid. The reduction of degree crystallinity is due to the less inter or/and intramolecular hydrogen attraction involving the amine group ( $NH_2$ ) of chitosan with higher oxalic acid contents.
- OA40 (with 40 wt. % oxalic acid) in System I exhibited the lowest crystallinity degree of 13 % with the highest conductivity value,  $4.95 \times 10^{-7}\ S\ cm^{-1}$ .
- OG60 (with 60 wt. % glycerol) in System II exhibited the lowest crystallinity degree of 11 % with the highest conductivity value,  $9.12 \times 10^{-5}\ S\ cm^{-1}$ .

## CHAPTER 7

### APPLICATION OF PLASTICIZED POLYMER ELECTROLYTE IN ELECTRICAL DOUBLE LAYER CAPACITOR

#### 7.1 Introduction

A battery differs from a capacitor in terms of electrical energy storage; an indirect storage in batteries happens as potentially available chemical energy requiring faradaic oxidation and reduction of an electroactive reagent to release charges that can perform electrical work when they flow between two electrodes having different electrode potentials. Direct energy storage is defined as an electrostatic way with negative and positive charges on the plates of a capacitor by a process termed as non-faradaic electrical energy storage (Sukhla *et al.*, 2000). Supercapacitors or electrochemical capacitors are electrochemical energy storage devices suited ideally to rapid storage and release of energy can be classified as redox supercapacitor and electrical double layer capacitor (EDLC) based on their modes of energy storage (Ji *et al.*, 2010).

The redox supercapacitor sustains a Faradaic reaction between the electrode and the electrolyte in a suitable potential window. The electrode material in this type of device consists of either transition metal oxides or mixture of carbon and metal oxides/polymers. An EDLC stores electric charge in the electric double layer which is formed at the interface between carbon electrodes and the electrolyte when a *dc* voltage is applied. The major constituent used in the electrodes of EDLC is carbonaceous

material (Jayalakshmi and Balasubramaniam *et al.*, 2008; Chanderasekaran *et al.*, 2010). A pair of polarizable electrodes with collector, a separator, and an electrolyte are the main features in EDLC. The electrical energy stored in the EDLC is discharged at loads (Nomoto *et al.*, 2001). EDLC fills the gap between batteries and conventional capacitors since EDLC can store more energy than the conventional capacitors and offers higher power density than the batteries (Jayalakshmi and Balasubramaniam, 2008). EDLC is used in various power and energy applications such as load-levelling, back-up power sources for electronic devices, engine start or acceleration for hybrid vehicles and electricity storage generated from solar or wind energy (Nomoto *et al.*, 2001; Sharma & Bhatti, 2010). Although the energy density of EDLC is much lower than the rechargeable batteries, EDLCs have stable charge-discharge performance in a wide temperature range, higher power density and able to deliver much higher power during 1 to 10 s provided the equivalent series resistance,  $R_s$ , is small enough (Lassègues *et al.*, 1995; Nomoto *et al.*, 2001).

In this chapter, the highest conducting plasticized electrolyte has been used as an electrolyte in the fabrication of an EDLC using porous carbon electrodes. The linear sweep voltammetry (LSV) of the electrolyte membrane is a crucial step for determining the stable potential range for further EDLC characterization. The fabricated EDLC was characterized using cyclic voltammetry (CV) and galvanostatic charge-discharge cycling in order to determine the specific capacitance ( $C_s$ ), cyclic durability, maximum energy and power.

## 7.2 Electrochemical stability of the plasticized electrolyte

Electrochemical stability is another important property of polymer electrolyte that needs to be investigated since the ionic conductivity value from impedance evaluation is not sufficient to justify whether the polymer electrolyte is suitable for practical application (Nithya *et al.*, 2012; Imperiyka *et al.*, 2014). Generally, the current-voltage characteristics of the polymer electrolyte have to be studied to determine whether the polymer electrolyte can withstand the operating voltage of the EDLC system or otherwise. This can be done using linear sweep voltammetry (Subramania *et al.*, 2006; Saikia *et al.*, 2011). The polymer electrolyte should have electrochemical stability within a wide potential window for suitable use in electrochemical devices. Linear sweep voltammetry was performed in the potential range from -4 to +4 V at a scan rate of 10 mV s<sup>-1</sup> at room temperature. The electrochemical stability window is defined as a potential region where no appreciable Faradaic current flows (Samir *et al.*, 2004; Arof *et al.*, 2010). The experiment was carried out by sandwiching sample OG60 (with 1.5 mm thickness) between two symmetrical stainless steel (SS) electrodes.

The current-voltage response of OG60 is depicted in Fig. 7.1. From the plot of current versus voltage, current flow through the film is almost constant until the applied voltage swept to further positive values and reached a breakdown/decomposition voltage at 2.3 V for OG60. This anodic decomposition limit at 2.3 V of OG60 can be considered as the voltage at which the current flows through the cell (Subramania *et al.*, 2006). This result shows the applicability of OG60 as solid polymer electrolyte in the fabrication of EDLC with electrochemical window limit at 2.3 V.

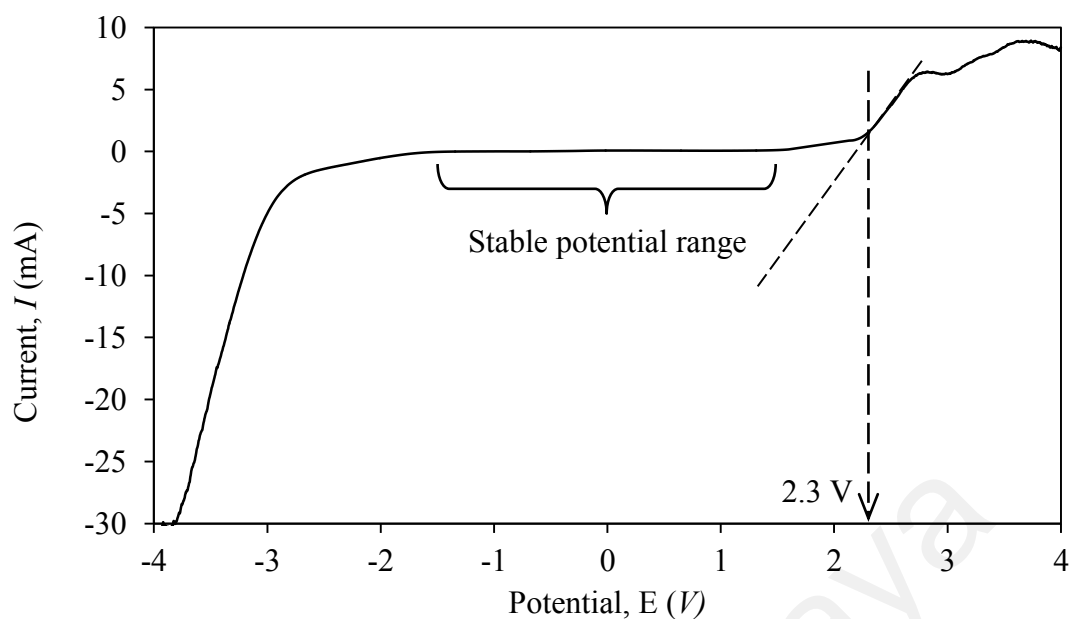


**Figure 7.1:** Linear sweep voltammetry (LSV) of the highest conducting plasticized polymer electrolyte OG60.

### 7.3 Electrochemical study on of electrical double layer capacitor (EDLC)

The electrochemical performance of EDLC is evaluated with cyclic voltammetry (CV) and galvanostatic charge-discharge (GCD). The EDLC is fabricated according to the scheme drawn in Fig. 3.8 with sample membrane OG60 as the electrolyte–cum–separator and porous carbon based material as the symmetrical electrodes.

#### 7.3.1 Cyclic voltammetry study

The performance of EDLC is examined by cyclic voltammetry at five different scan rates; 1, 3, 5, 7, 10  $\text{mV s}^{-1}$  within the potential range between -0.6 and 6.0 V. According to Yalcinkaya *et al.*, (2010) the oxidation of the electrolyte OG60 was observed in the forward scan and the reduction was on the reverse scan (this is distinguished as redox behaviour). The voltammetry curves in Fig. 7.2 exhibit an almost rectangular shape especially at scan rate of 7  $\text{mV s}^{-1}$  which indicates a typical capacitive behaviour with a double layer formed at the interfaces (Lewandowski & Świdowska,

2006; Zhang *et al.*, 2008; Pandey *et al.*, 2011; Senthilkumar *et al.*, 2012). In addition, these types of voltammograms implied that charge and discharge occur almost reversibly at the electrode/electrolyte interface, and sample membrane OG60 is electrochemically stable under this condition (Wada *et al.*, 2004).

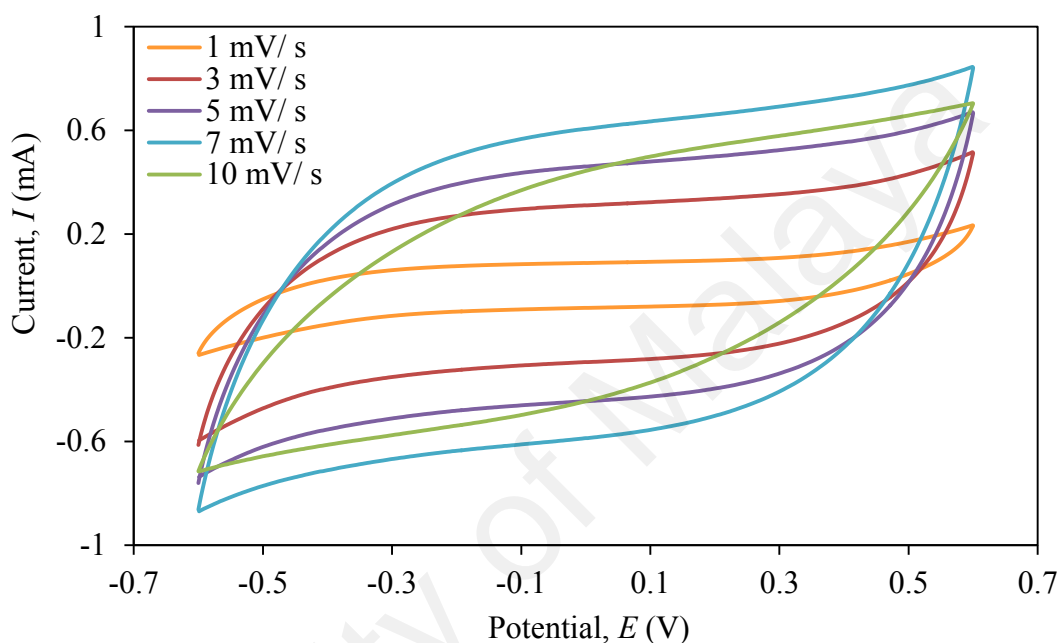


**Figure 7.2:** Cyclic voltammograms for EDLC comprises OG60 as electrolyte.

The low scan rate voltammograms in Fig. 7.2 exhibited almost perfect horizontal plateaus indicating ion diffusion occurs at a fairly constant rate with little impact from ohmic resistance. The deviation from the perfect rectangular shape of CV curve is observed at higher scan rate of  $10 \text{ mV s}^{-1}$  which was attributed to the finite value of the equivalent series resistance (ESR) in polymer based EDLC (Pandey *et al.*, 2011). The effect of equivalent series resistance (ESR) can be observed as scan rate increased. The current is delayed longer at higher scan rate in reaching a constant value on reversal of the potential sweep (Arof *et al.*, 2012). The ion penetration at the pores of carbon becomes more difficult at scan rate higher than  $7 \text{ mV s}^{-1}$  during forward and reverse

scans due to diffusion limitation in the pores may also result in the anomaly of CV curve from the perfect rectangular shape (Chanderasekaran *et al.*, 2010).

The specific capacitance ( $C_s$ ) value of the EDLC can be evaluated from the respective cyclic voltammograms using the equation (Fang *et al.*, 2012; Liew *et al.*, 2014):

$$C_s = \frac{\Delta I}{2\Delta V * m} \quad (7.1)$$

where  $C_s$  is the specific capacitance ( $F g^{-1}$ ),  $\Delta I$  is the average current (mA),  $\Delta V$  is the voltage scan rate ( $mV s^{-1}$ ),  $m$  is the mass per electrode.

**Table 7.1:** The specific capacitance,  $C_s$  value at respective scan rate.

Scan rate, $mV s^{-1}$	Specific capacitance, $C_s$
1	6
3	5
5	4
7	3
10	2

The calculated specific capacitance,  $C_s$  shows that the lowest scan rate exhibited the highest value as depicted in Table 7.1. The phenomenon behind the decrement of  $C_s$  value as the scan rate is increased can be interpreted as the decrease in the capacitive value delivered by the porous carbon electrodes (Zheng *et al.*, 2010). It is also due to the diffusion limitation in pores of carbon during reversal of the potential since the ion penetration is hard to occur at higher scan rate (Chanderasekaran *et al.*, 2010). Thus the EDLC is dependent on scan rate, which is characteristic of capacitor cells.

### 7.3.2 Charge-discharge study

The galvanostatic charge-discharge (GCD) characterization of EDLC was carried out to study the effect of current density on EDLC performance. In this work, two tests on the performance of EDLC was investigated firstly by varying several voltage limits at fixed current; and another test is done by fixing the voltage limits while varying the current.

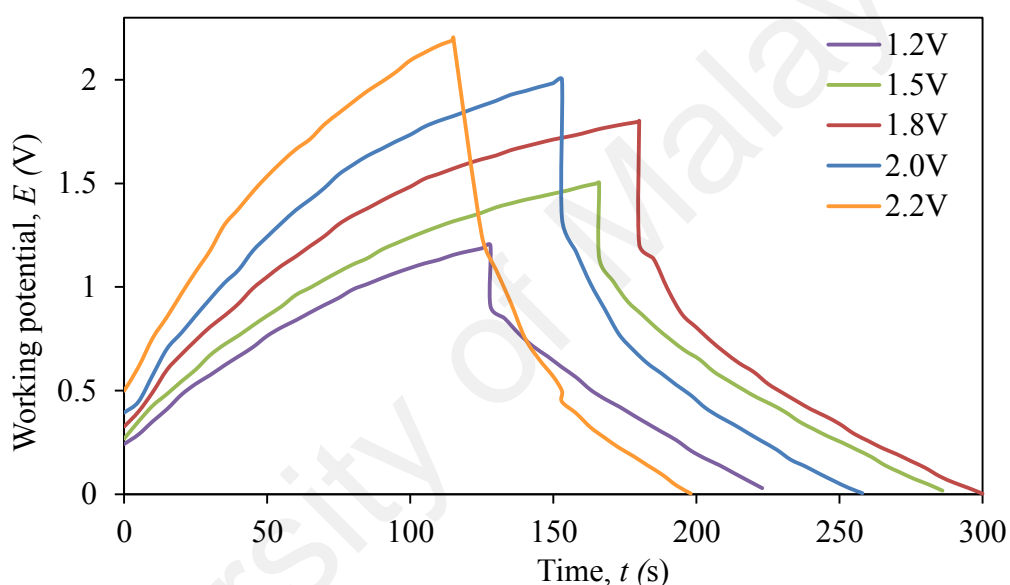


**Figure 7.3:** Charge-discharge characteristic for EDLC at fixed current, 1 mA.

In Fig 7.3, GCD curves were plotted with working potentials of 1.2, 1.5, 1.8, 2.0 and 2.2 V and electrode mass of 0.0098 g. The charging curve of GCD is followed by the discharging curve with a voltage drop at the beginning of the discharging process. This is due to ohmic loss across the internal resistance also known as equivalent series resistance (ESR) in electrode and electrolyte and this represents the resistive behaviour of EDLC (Hashmi *et al.*, 2007; Suhaimi *et al.*, 2012).

The specific capacitance  $C_s$  ( $F g^{-1}$ ) can be calculated from the gradient of the linear portion of the charge and discharge characteristics using equation (Suhaimi *et al.*, 2012):

$$C_s = \frac{i}{m * \left( \frac{\Delta V}{\Delta t} \right)} \quad (7.2)$$

where  $i$  is the discharge current and  $\Delta V/\Delta t$  is the gradient of the linear portion from the discharge curve. Energy density,  $E$  ( $W h kg^{-1}$ ) delivered during the discharge was calculated in using equation:

$$E = \frac{1}{2} (C_s * \Delta V^2) \left( \frac{1000}{3600} \right) \quad (7.3)$$

here  $C_s$  is the specific capacitance and  $\Delta V$  is the is the potential difference. Power density,  $P$  ( $W kg^{-1}$ ) of EDLC can be determined using equation:

$$P = \left( \frac{i * \Delta V}{2 * m} \right) 1000 \quad (7.4)$$

where  $i$  is the discharge current,  $\Delta V$  is the potential difference and  $m$  is the mass of electrode. The calculated values of potential difference, specific capacitance  $C_s$ , energy density  $E$ , and power density  $P$  obtained from the EDLC comprised of OG60 as the electrolyte are listed in Table 7.2.

From Table 7.2, one can observe that the charge-discharge profile of EDLC exhibits the highest specific capacitance  $C_s$  of  $13 F g^{-1}$  at fixed current 1 mA with 1.2 V as the working potential. However, the highest value of energy density  $E$  is  $0.90 W h kg^{-1}$  and power density  $P$  is  $49 W kg^{-1}$  are shown by EDLC operated at the working potential of 2.2 V. This shows that although EDLC deliver lower capacitance at

working potential 2.2 V, in terms of time it can produce higher energy density and power density compared to that operated at 1.2 V. EDLC showed the highest capacitance value of 13 F g<sup>-1</sup> with working potential 1.2 V.

**Table 7.2:** The calculated values of potential difference  $\Delta V$ , specific capacitance  $C_s$ , energy density  $E$ , and power density  $P$  at different working potential.

Working potential (V)	Potential difference, $\Delta V$ (V)	Specific capacitance, $C_s$ (F g <sup>-1</sup> )	Energy density, $E$ (W h kg <sup>-1</sup> )	Power density, $P$ (W kg <sup>-1</sup> )
1.2	0.28	12.76	0.12	14.16
1.5	0.36	11.34	0.23	18.41
1.8	0.60	10.20	0.55	30.35
2	0.70	9.28	0.56	35.71
2.2	0.96	7.29	0.90	48.87

The effect of varying the applied current (0.1, 0.5, 1 mA) while fixing the voltage limits at 1.2 V is studied on a freshly prepared EDLC with electrode mass of 0.0128 g. Fig. 7.4 shows the effect of varying the applied current on charge-discharge profile. The calculated values of potential difference, specific capacitance  $C_s$ , energy density  $E$ , and power density  $P$  obtained from the EDLC comprised of OG60 as the electrolyte are listed in Table 7.3.

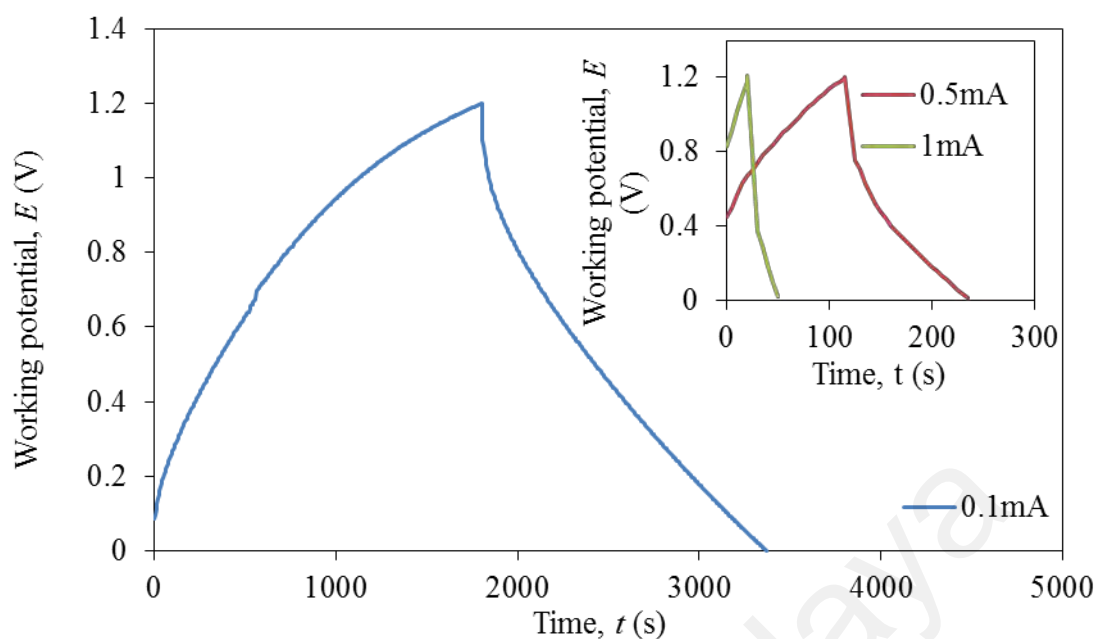


**Figure 7.4:** Charge-discharge profile at different applied current.

**Table 7.3:** The calculated values of potential difference  $\Delta V$ , specific capacitance  $C_s$ , energy density  $E$ , and power density  $P$  at different applied current.

Applied current (mA)	Potential difference, $\Delta V$ (V)	Specific capacitance, $C_s$ ( $F g^{-1}$ )	Energy density, $E$ ( $W h kg^{-1}$ )	Power density, $P$ ( $W kg^{-1}$ )
0.1	0.10	12.56	0.02	0.39
0.5	0.45	6.18	0.17	8.7
1.0	0.84	4.20	0.41	32.7

The highest specific capacitance  $C_s$  of  $\sim 13 F g^{-1}$  with 0.1 mA as applied current was calculated from the charge-discharge profile of EDLC. The highest value of energy density  $E$  ( $0.41 W h kg^{-1}$ ) and power density  $P$  ( $33 W kg^{-1}$ ) were exhibited by the EDLC operated at applied current 1.0 mA. This shows that although EDLC delivered lower capacitance at applied current 1.0 mA, in terms of time it can produce higher energy density and power density compared to that operated at 0.1 mA (as EDLC showed the highest capacitance value of  $13 F g^{-1}$ ). In addition, the specific capacitance value decreases gradually with the increase in the scan rate. This behaviour can be explained

by the reduced diffusion time since the electrolyte ions cannot be fully accessible to the interior surfaces of the electrodes for charge storage at high scan rates (Wang *et al.*, 2013).

Further investigation on EDLC cycle life was done in order to study the stability of the EDLC in terms of charging and discharging processes. Fig. 7.5 shows the GCD profile up to 10 cycles with value of specific capacitance  $C_s$  and coulombic efficiency along with energy density and power density are tabulated in Table 7.4. The coulombic efficiency,  $\eta$  can be calculated using equation:

$$\eta = \frac{C_d}{C_c} \times 100 = \frac{t_d}{t_c} \times 100 \quad (7.5)$$

where  $C_d$  and  $C_c$  are the discharge and charge capacitance respectively,  $t_d$  and  $t_c$  represent the time for galvanostatic discharging and charging respectively.

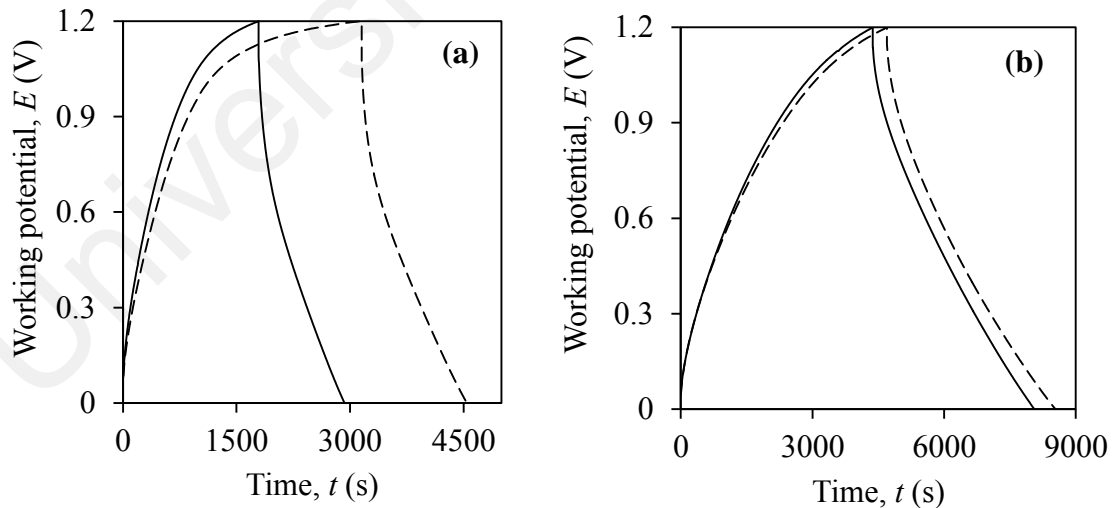


**Figure 7.5:** Charge-discharge profile at applied current (a) 0.1 mA and (b) at 1 mA. The continuous line (–) depicts the GCD curve at 1st cycle meanwhile dotted line (--) depicts curve at 10th cycle.

The performance of EDLC at 1mA after 10th cycle is better than EDLC operated at 0.1 mA. In the former case, the specific capacitance increased to 7 F g<sup>-1</sup> but in the latter case, the specific capacitance does not experience any significant changes. Moreover, the EDLC can deliver higher power density of 380 mW kg<sup>-1</sup> at 1 mA compared to the value that operated at 0.1 mA. In addition, the applied current 1 mA exhibit high coulombic efficiency even after 10<sup>th</sup> cycle, which is almost two-fold of the ones exhibited by EDLC with 0.1 mA as the applied current.

**Table 7.4:** Parameters of GCD at different cyclic processes.

Parameter \ Applied current	0.1 mA		1mA	
	1st cycle	10th cycle	1st cycle	10th cycle
Potential difference, $\Delta V$ (V)	0.111	0.123	0.06	0.05
Specific capacitance, $C_s$ (F g <sup>-1</sup> )	2.04	2.38	4.76	7.14
Energy density, $E$ (mW h kg <sup>-1</sup> )	3.49	5.00	2.72	28.18
Power density, $P$ (mW kg <sup>-1</sup> )	79.29	87.87	457.86	380.71
Coulombic efficiency, $\eta$ (%)	63	44	84	82

#### 7.4 Summary

The electrochemical studies on OG60 as electrical double layer capacitor show that;

- The highest specific capacitance value of the plasticized polymer electrolyte OG60 is 6 F g<sup>-1</sup> when the lowest scan rate 1 mV s<sup>-1</sup> is used.

- EDLC exhibits specific capacitance value of  $13 \text{ F g}^{-1}$  when working potential 1.2 V is used resulting  $0.12 \text{ W h kg}^{-1}$  and  $14 \text{ W kg}^{-1}$  as energy density and power density delivered respectively at fixed current 1 mA.
- When the working potential 1.2 V was fixed, the applied current 0.1 mA produced specific capacitance of  $13 \text{ F g}^{-1}$  with  $0.02 \text{ W h kg}^{-1}$  and  $0.4 \text{ W kg}^{-1}$  as energy density and power. However, the applied current 1 mA produced much higher energy density ( $11 \text{ W h kg}^{-1}$ ) and power density ( $33 \text{ W h kg}^{-1}$ ).
- Cyclic durability test was carried out by scanning up to 10th cycle with different applied current and at fixed potential 1.2 V. The EDLC with applied current 1 mA exhibited a better performance after the 10<sup>th</sup> cycle as there is no significant change in specific capacitance and coulombic efficiency.

## CHAPTER 8

### DISCUSSION

Energy storage systems such as batteries and electrochemical capacitors have started to influence a larger part in our daily activities (Simon & Gogotsi, 2008). This has led to the increment in renewable energy production from the sun and wind, as well as the development of electric vehicles or hybrid electric vehicles with low carbon dioxide emission. Electrical double layer capacitors (EDLC) are one of the emerging energy storage devices. It stores energy in the double-layer at the electrode/electrolyte interface in a suitable potential window (Yang *et al.*, 2005). Various types of carbon materials with high surface area have been used for EDLCs. The porosity of carbon is important since it influences the accessibility of electrolytes in the charge/discharge processes as the surface of the pores is utilized for charge storage at high loading current density. Thus, the presence of porous carbon in the electrodes efficiently increased the transportation of ions into the active sites due to its large surface area (Li *et al.*, 2007).

The main drawback in the utilization of liquid electrolyte in commercial electrochemical devices is its high flammability. To prevent possible electrolyte leakage, metal casing is required. A separator must be placed between cathode and anode to avoid short circuit in the cell. The weight of the container and volume occupied by the separator decrease the specific energy of the device. The use of the liquid electrolyte leads to problems such as production of gases upon overcharge and thermal runaway reaction when it is heated to high temperatures. Besides, large volume of toxic and hazardous materials of the device components is also released to

environment (Arcana et al., 2013). Replacing liquid electrolytes by solid polymer electrolytes is useful due to easy handling (Lewandowski *et al.*, 2001). The potential application of solid polymer electrolytes (SPEs) in electrochemical devices is an interesting issue due to advantages including the ease of fabrication and free of leakage problems (Xu *et al.*, 1998). Polymer electrolyte can be defined as any polymer-based structure with significant ionic conductivity. The solid character of polymers is generally related to the molecular weight of the polymer (Sequeira & Santos, 2010).

In the present work, a study was made on natural chitosan polymer to investigate its ability to host proton conduction provided by oxalic acid. The conductivity of the chitosan-oxalic acid system was also investigated after addition with glycerol. Chitosan is an amino polysaccharide which is chemically derived from chitin that made the exoskeleton of crustaceans (i.e. shrimp, crab) by a chemical process called N-deacetylation in sodium hydroxide (NaOH) solution (Muzzarelli, 1978; Lavorgna *et al.*, 2010). This process converts the acetyl group at N of chitin into amine group and the functional conversion results in chitosan production with treatment time as the conversion parameter. The degree of conversion is called as degree of deacetylation (DD) which is depends on the chemical treatment time. In addition, the higher degree of conversion means that the acetyl group in chitin is highly converted into amine group and DD is evaluated as a percentage (i.e. DD = 80 %).

The polyelectrolyte nature of chitosan makes it a suitable candidate as polymer host for ionic conduction application. However, chitosan cannot dissolve in organic solvents due to the small amount of hydrogen bonding (depending on DD) still present in the polymer backbone even after the N-deacetylation process. The presence of two functional groups in chitosan; hydroxyl (OH) and amine (NH<sub>2</sub>) make it susceptible to

modifications either by chemical or physical means. Chemical modification will result in structure changes and/or molecule conformation whereas physical modification will change or enhance the physical properties of chitosan. In this work, since chitosan can dissolve in dilute acids, ionic crosslinking has been made by dissolving chitosan in an acidic medium. This is due to the proton ( $H^+$ ) from the dilute acid that interacted with the amine group of chitosan and resulted in protonated amine ( $NH_3^+$ ). This reduced the hydrogen bonding in chitosan hence enabling it to dissolve in the acidic medium.

The classification of sample membranes in this work is divided into two systems, namely System I (OA system) and System II (OG system). The first system is comprised of chitosan–oxalic acid, whereas the second one is consisted of chitosan–oxalic acid–glycerol. Oxalic acid is the simplest dicarboxylic acid with high reactivity and low dissociation constant value,  $pK_a$  has been chosen as the dissolution medium. The solid polymer electrolytes were prepared by dissolving in different amounts (as in weight percentages) of oxalic acid. The sample membranes were kept in a desiccator prior to use in order to minimize the moisture content. The oxalic acid was recrystallized to minimize or eliminate the impurities and was always kept in a drying oven.

The dissolution of oxalic acid in water produces protons that will protonate the amine group ( $NH_2$ ) of chitosan into  $NH_3^+$ . Oxalic acid becomes a negatively charge oxalate ion due to its proton loss. The ability of oxalic acid to undergo twice dissociation results in the formation of negatively charged O at its both ends. The positively charged protonated amine at two different chitosan chains will form ionic interaction with the negatively charged oxalate ion hence forming ionic crosslinking. The ionic crosslinking scheme was based on Gümüšoğlu *et al.* (2011) as shown in Fig.

4.6. In their work, they used sulphuric acid to ionic crosslink the chitosan polymer chains in order to lower methanol permittivity and obtain better mechanical integrity. Impedance studies based on oxalic acid crosslinked chitosan has not been reported elsewhere by other researchers. However other work based on ionic crosslinked polyelectrolyte complex membrane based on chitosan and poly(acrylic acid) showed a conductivity of  $\sim 2 \times 10^{-4} \text{ S cm}^{-1}$  in its hydrated condition at  $25 \text{ }^\circ\text{C}$  (Gümüšođlu *et al.* 2011). Another work on hydrated chitosan in water with conductivity value of  $\times 10^{-4} \text{ S cm}^{-1}$  was reported by Wan *et al.* (2003). In their work, chitosan was dissolved in 1 % acetic acid and was immersed in deionized water at room temperature for the required time. Unfortunately, the conductivity value of the membranes in dry form exhibit ionic conductivities between  $10^{-10}$  and  $10^{-9} \text{ S cm}^{-1}$ . The conductivity values reported by Gümüšođlu *et al.* (2011) and Wan *et al.* (2003) differ from the one studied in this work with value of  $4.95 \times 10^{-7} \text{ S cm}^{-1}$ . This due to the dry state of membranes in the chitosan-oxalic acid system. The incorporation oxalic acid in chitosan is insufficient to make the chitosan-based electrolytes useful for application in electrochemical devices. Thus it is necessary for additives to be added in the electrolyte membranes to enhance the ionic conductivity.

The addition of glycerol is able to interpenetrate and swell the polymer network thus increasing the volume for proton conduction in the present work (Lewandowski *et al.*, 2001). The small size of glycerol enables the molecules to intersperse and intercalate among and between polymer chains, disrupting hydrogen bonding and spreading the chains apart, hence increases flexibility (Bourtoom, 2008). In this work, the conductivity of chitosan-oxalic acid membrane increased with glycerol addition. The highest conductivity value of  $9.12 \times 10^{-5} \text{ S cm}^{-1}$  is featured by the sample containing 60 wt. % glycerol (OG60). Besides the conductivity value increased by two

orders of magnitude at room temperature, the prominent change that can be seen is the bulk resistance  $R_b$  value decreased drastically to 94 from 4560  $\Omega$  for sample OG60. The effect of plasticizer addition in polymer electrolytes can be seen in various works. Ng and Mohamad (2006) reported a work on ethylene carbonate plasticization in ammonium nitrate ( $\text{NH}_4\text{NO}_3$ ) doped chitosan. The conductivity of the chitosan-40 wt. %  $\text{NH}_4\text{NO}_3$  film at room temperature was increased by two orders of magnitude with the addition of ethylene carbonate from  $\sim 10^{-4}$  to  $\sim 10^{-2}$   $\text{S cm}^{-1}$ . A polymer blend consists of chitosan and starch as polymer host and lithium perchlorate as a dopant was plasticized with glycerol (Sudhakar & Selvakumar, 2012). The maximum conductivity is found to be  $3.7 \times 10^{-4}$   $\text{S cm}^{-1}$  at room temperature for 60:40 (CS/starch) with 25 wt. % glycerol. This conductivity value is much higher compared to the sample without glycerol plasticization which only can achieve  $\sim 10^{-7}$   $\text{S cm}^{-1}$ . It is therefore, the conductivity value for the chitosan-oxalic acid-glycerol samples in this work is comparable with the previous researches. The increase in conductivity of chitosan based electrolyte with increasing concentration of oxalic acid and glycerol can be seen as depicted in Fig. 4.5 and Fig. 4.20.

The impedance and dielectric properties of chitosan–oxalic acid and chitosan–oxalic acid–glycerol system were studied using electrochemical impedance spectroscopy (EIS). Nyquist plot consists of a depressed semicircle or a depressed semicircle with a tilted spike for chitosan–oxalic acid system or a tilted spike for chitosan–oxalic acid– glycerol system as shown in Fig. 4.4 and Fig. 4.19. The occurrence of the low frequency tilted spike is due to the blocking effects at the electrode/electrolyte interface (Cui *et al.*, 2008). The intersection of the low frequency straight line with real impedance axis  $Z_r$  for both systems with stainless steel as the blocking electrode is found to be less than  $90^\circ$ . According to Karthikeyan *et al.* (2000),

this behaviour could be due to the irregularities in the electrode/electrolyte interface geometry. This condition is in contrast to the ideal capacitance which exhibits a 90° low frequency vertical spike in impedance plot. In this work, it was observed that the bulk resistance  $R_b$  is decreasing with the increasing amount of oxalic acid which led to the increase in conductivity. Same trend was also observed with the addition of glycerol in the chitosan–oxalic acid electrolytes.

The rise in operating temperature results in decrement of  $R_b$  for chitosan-oxalic acid membranes and chitosan-oxalic acid-glycerol membranes as seen in Fig. 4.7 and Fig. 4.22 respectively. The behaviour implies that the conductivity of the electrolyte is improved as the temperature is raised. This shows that the ionic mobility is a thermally activated process (Sekhar *et al.*, 2013). The activation energy  $E_A$  for the highest conducting membranes of each System I and II were obtained from the gradient of the plot of  $\log \sigma$  versus  $1000/T$  as shown in Fig. 4.8 and Fig. 4.23. The highest room temperature conducting samples OA40 and OG60 exhibit a linear line obeying Arrhenius expression with regression value,  $R^2$  were approaching to 1. The linear relation implied that there is no phase transition in the polymer matrix or the domain formed with the addition of oxalic acid and glycerol. The calculated activation energy  $E_A$  for sample OA40 and OG60 are 0.61 and 0.30 eV respectively. During thermal application, the polymer chain acquires faster internal modes which results in bond vibration, favouring inter-chain and intra-chain ion hopping movements and local structure relaxations that increased the conductivity of the polymer electrolyte (Selvasekarapandian *et al.*, 2005; Sudhakar & Selvakumar, 2012). The low activation energy values of these electrolytes suggest that there is relatively fast hopping mechanism for the ions, which is because of the thermally activated mobile protons (Sengwa *et al.*, 2014).

A study on dielectric constant value for both systems was carried out in order to measure the stored charge (Winie & Arof, 2004). An increased value in dielectric at high frequency region implied that the number of free ions is greater along with the reduction of coulombic interaction between ions. The dielectric constant value of OA40 increased from 7.44 to 18.41 with addition of 60 wt. % glycerol (OG60) which indicates that the ion dissociation was assisted by the plasticizer addition. In addition, this dielectric constant values was in an agreement with the values of ionic conductivity. A further investigation of dipole relaxation in the polymer electrolytes was also carried out by calculating the relaxation parameter (Aziz *et al.*, 2012). The best relaxation time  $\tau$  obtained for System I is  $5.27 \times 10^{-5}$  s was shown by OA40, whereas OG60 exhibits a shorter relaxation time of  $3.98 \times 10^{-6}$  s in System II. The values of relaxation time were observed to decrease further with the addition of glycerol in the chitosan–oxalic acid system hence, resulting in the increment of ionic conductivity. In addition, the activation energy for relaxation  $E_B$  for sample OA40 in System I is calculated to be 0.61 eV which is similar to the Arrhenius activation energy  $E_A$ . From the similarities of these values, a conclusion can be made that the ion transportation occurs through hopping mechanism while relaxing as well as while conducting in the chitosan–oxalic acid system (Sengwa *et al.*, 2014).

The interaction between chitosan, oxalic acid and glycerol were investigated by evaluating the transmission of Fourier Transform Infrared (FTIR) spectra. The changes in the spectra such as peak shifting and intensity along with presence of a new peak can determine the types of interaction that occurred in the polymer electrolytes. The protonation of amine group ( $\text{NH}_2$ ) to  $\text{NH}_3^+$  in chitosan occurred as the oxalic acid content is increased hence resulted in the presence of new peaks  $\text{NH}_3^+$  at 1610-1615

$\text{cm}^{-1}$  and  $\text{COO}^-$  at  $1724 \text{ cm}^{-1}$ . The specific region of FTIR spectra was further investigated in order to study the effect on hydroxyl and amine group of chitosan with increasing of oxalic acid content by deconvolution method utilizing the Gaussian-Lorentzian function and the area of the deconvoluted bands were calculated using the OMNIC software. The area under the deconvoluted peaks for protonated amine,  $\text{NH}_3^+$  was observed to increase proportionally with oxalic acid content. On the contrary, the area under the deconvoluted  $\text{NH}_2$  peak decreased with increasing oxalic acid content. Upon the addition of glycerol as plasticizer, the interaction between glycerol and chitosan results in the shift of the doublet peaks of symmetric and asymmetric stretching for alkyl group in chitosan (C-H) at  $2939$  and  $2882 \text{ cm}^{-1}$  upward to  $2944$  and  $2890 \text{ cm}^{-1}$ . In this work, it has been proven that FTIR is an undeniable important tool in detecting the functional groups and determining the interactions in polymer electrolytes consisting chitosan, oxalic acid and plasticizer glycerol.

Polymer electrolytes need to exhibit low degree of crystallinity in order to exhibit high conductivity values. The x-ray diffractions (XRD) were done on the polymer electrolytes by passing the x-ray beam perpendicular and parallel to its surface. In this work, x-ray diffractions has been used to calculate the degree of crystallinity for chitosan based membranes with degree of deacetylation higher than 75 %. The relative degree of crystallinity,  $\chi_c$  of each sample membrane can be calculated using the simplicity approach of the two-phase model from XRD pattern using the equation by Hassan *et al.* (2013) and Lewandowska *et al.* (2011). In System I, the crystallinity degree of chitosan decreases with the addition of oxalic acid. The reduction of crystallinity degree is due to the lesser inter or/ and intramolecular hydrogen attraction involving amine  $\text{NH}_2$  of chitosan with higher oxalic acid contents. The highest conducting membrane in System I OA40 exhibited the lowest degree of

crystallinity of 13 %. Whereas in System II, the degree of crystallinity for the sample membranes increases abruptly as high as 29 % with the addition of glycerol as low as 10 wt. % which is due to the anti-plasticization effect at low glycerol content (Liu *et al.*, 2013). They reported that the addition of glycerol lower than 2.5 % caused the degree of crystallinity to increase and at higher glycerol contents such as 5.0 % and 10.0 % will reduce the crystallinity of the membranes. In this work, the reduction in degree of crystallinity with the increasing of glycerol contents is due to preferential interaction between glycerol and oxalate ions. This caused the polymer becomes more flexible with the enhancement of bond rotations which leads to the increment of mobility of the polymer chains (Mubarak *et al.*, 2013; Selvasekarapandian *et al.*, 2005; Sudhakar & Selvakumar, 2012; Lazaridou *et al.*, 2012). Sample membrane OG60 in System II exhibited the lowest crystallinity degree of 11 %.

The highest conducting plasticized polymer electrolyte OG60 was fabricated into electrical double layer capacitor (EDLC) with symmetrical porous carbon as electrodes. Linear sweep voltammetry experiment was performed on OG60 in the potential range of -4 to 4 V with scan rate of 10 mV/ s at room temperature with stainless steel as the electrodes in order to determine the electrochemical stability of polymer electrolytes (Subramania *et al.*, 2006; Saikia *et al.*, 2011). It was observed from the plot of current versus voltage, current flow in the film is almost constant until the applied voltage swept to further positive value and reached a voltage breakdown/ decomposition voltage of 2.3 V. The performance of EDLC is examined by cyclic voltammetry at five different scan rates; 1, 3, 5, 7, 10 mV/ s with the potential range between -0.6 and 6.0 V and the highest specific capacitance value of the plasticized polymer electrolyte OG60 is 6 F g<sup>-1</sup> when the lowest scan rate 1 mV s<sup>-1</sup> is used.

The galvanostatic charge-discharge (GCD) characterization of EDLC was carried out to study the effect of current density on EDLC performance. In this work, two tests on the performance of EDLC was investigated firstly by varying several voltage limits at fixed current; and another test is done by fixing the voltage limits while varying the current. The EDLC exhibits a specific capacitance value of  $13 \text{ F g}^{-1}$  when working potential  $1.2 \text{ V}$  is used resulting  $0.12 \text{ W h kg}^{-1}$  and  $14 \text{ W kg}^{-1}$  as energy density and power density delivered respectively at fixed current  $1 \text{ mA}$ . The presence of a voltage drop at the beginning of the discharging process can be seen in Fig. 7.4. This is due to ohmic loss across the internal resistance also known as equivalent series resistance (ESR) in electrode and electrolyte and this represents the resistive behaviour of EDLC (Hashmi *et al.*, 2007; Suhaimi *et al.*, 2012). When the working potential  $1.2 \text{ V}$  is fixed, the applied current  $0.1 \text{ mA}$  produced specific capacitance of  $13 \text{ F g}^{-1}$  with  $0.5 \text{ W h kg}^{-1}$  and  $0.4 \text{ W kg}^{-1}$  as energy density and power. However, the applied current  $1 \text{ mA}$  produced much higher energy density ( $0.41 \text{ W h kg}^{-1}$ ) and power density ( $33 \text{ W h kg}^{-1}$ ). A cyclic durability test was carried out by scanning the EDLC up to 10th cycle with different applied current and at fixed potential  $1.2 \text{ V}$ . The EDLC with  $1 \text{ mA}$  as applied current exhibited a better performance after the 10<sup>th</sup> cycle as no significant change in specific capacitance and coulombic efficiency were observed.

## CHAPTER 9

### CONCLUSION AND SUGGESTIONS FOR FURTHER WORK

This work discussed the preparation of chitosan based solid polymer electrolyte incorporating oxalic acid as proton donor. Chitosan is a biopolymer and the molecules of chitosan exist as cationic polyelectrolyte in acidic solution. Being a polyelectrolyte, chitosan spontaneously acquiring a large number of elementary charges distributed along the molecular chain when dissolved in oxalic acid. The main objectives of this work are to develop and optimize the high conducting plasticized chitosan based solid polymer electrolytes. The highest ionic conductivity at room temperature was found to be  $4.95 \times 10^{-7} \text{ S cm}^{-1}$  for sample OA40 with 40 wt. % oxalic acid. The conductivity of OA40 was increased with the addition of plasticizer glycerol. Glycerol is a small molecule polyol type plasticizer that able to intersperse and intercalate among and between chitosan polymer chains, disrupting hydrogen bonding and spreading the chains apart. Furthermore, it can assist the proton dissociation by forming hydrogen bonds between its hydroxyl group and carbonyl group of oxalic acid. This interaction withdrew the electron density of the oxygen of hydroxyl group in oxalic acid thereby the proton was released easily. Sample with 60 wt. % glycerol (OG60) exhibited the highest room temperature conductivity value of  $9.12 \times 10^{-5} \text{ S cm}^{-1}$ . The conductivity studies on this plasticized chitosan based electrolyte proved that the objectives of this have been achieved. The dielectric constant value of OA40 was found to be increased from 7.44 to 18.41 with addition of 60 wt. % glycerol (OG60) which indicates that the ion dissociation was assisted by the plasticizer addition. This dielectric constant values was in an agreement with the values of ionic conductivity.

A further investigation of dipole relaxation in the polymer electrolytes was also carried out by calculating the relaxation parameter (Aziz *et al.*, 2012). The lowest relaxation time  $\tau$  obtained for System I is  $5.27 \times 10^{-5}$  s was exhibited by OA40, whereas OG60 exhibits the lowest value of  $3.98 \times 10^{-6}$  s in System II. From these relaxation time values, a conclusion can be made that the ionic conductivity is inversely related to the relaxation time. The conductivity values for both OA40 and OG60 from System I and System II respectively showed the maximum while the relaxation time values were the minimum.

The conduction behaviour is directly correlated with the crystallinity of the polymer electrolyte. X-ray diffraction has been used to calculate the crystallinity degree of chitosan based membranes. In System I, the crystallinity degree of chitosan decreases with the addition of oxalic acid. The highest conducting membrane OA40 in System I exhibited the lowest crystallinity degree of 13 %. Whereas in System II, the crystallinity degree of the sample membranes increases abruptly as high as 29 % with the addition of glycerol as low as 10 wt. % which is due to the anti-plasticization effect at low glycerol content. The reduction of crystallinity degree with the increasing of glycerol contents is due to preferential interaction between glycerol and oxalate ions. Sample membrane OG60 in System II exhibited the lowest crystallinity degree of 11 %.

Another objective in this work is to fabricate an electrochemical double layer capacitor (EDLC) device using OG60 as the electrolyte. The symmetrical electrodes for EDLC containing porous carbon and poly(vinyl pyrrolidone) (PVP) in ratio 8:1 were prepared by doctor blade technique. The linear sweep voltammetry of sample OG60 reached a breakdown/decomposition voltage at 2.3 V. The cyclic voltammetry curves

of OG60 exhibit an almost rectangular shape especially at scan rate of  $7 \text{ mV s}^{-1}$ . The EDLC exhibits specific capacitance value of  $13 \text{ F g}^{-1}$  when working potential  $1.2 \text{ V}$  is used producing  $4 \text{ W h kg}^{-1}$  and  $14 \text{ W kg}^{-1}$  as energy density ( $E$ ) and power density ( $P$ ) delivered respectively at fixed current  $1 \text{ mA}$ . The cyclic durability test was carried out on the EDLC by scanning up to 10th cycle with different applied current and at fixed potential  $1.2 \text{ V}$ . The EDLC with applied current  $1 \text{ mA}$  exhibited a better performance after the 10<sup>th</sup> cycle compared to that of applied current  $0.1 \text{ mA}$  as there is no significant change in specific capacitance and coulombic efficiency. The electrochemical results obtained show that the objective of fabricating EDLC with the optimized plasticized polymer electrolyte OG60 has been achieved.

Further work studies should be extended to improve the ionic conductivity for chitosan based solid polymer electrolyte. Accordingly, different types of ionic liquids such as sulfonium-, thiophenium- and thioxonium-cation based can be doped in order to increase the ionic conductivity and operating voltage of EDLC. This ionic liquid can widen the electrochemical stability window and enhance the specific capacitance.

Ali, R. M., Harun, N. I., Ali, A. M. M., & Yahya, M. Z. A. (2012). Effect of ZnS dispersoid in structural and electrical properties of plasticized CA-NH<sub>4</sub>I. *Physics Procedia*, 25, 293-298.

Arcana, I. M., Bundjali, B., Achmad Rochliadi, A., & Hariyawati, N. K. (2013, Nov.). *Preparation of Polymers Electrolyte Membranes from Styrofoam Waste for Lithium Battery*. Paper presented at Joint International Conference on Rural Information & Communication Technology and Electric-Vehicle Technology (rICT & ICeV-T), Bandung-Bali, Indonesia.

Arof, A. K., Kufian, M. Z., Shukur, M. F., Aziz, M. F., Abdelrahman, A. E., & Majid S. R. (2012). Electrical double layer capacitor using poly(methyl methacrylate)-C<sub>4</sub>BO<sub>8</sub>Li gel polymer electrolyte and carbonaceous material from shells of mata kucing (*Dimocarpus longan*) fruit. *Electrochimica Acta*, 74, 39-45.

Arof, A. K., Amiruddin, S., Yusof, S. Z., & Noor, I. M. (2014). A method based on impedance spectroscopy to determine transport properties of polymer electrolytes. *Physical Chemistry Chemical Physics*, 16, 1856-1867.

Arof, A. K., Shuhaimi, N. E. A., Alias, N. A., Kufian, M. Z., & Majid, S. R. (2010). Application of chitosan/iota-carrageenan polymer electrolytes in electrical double layer capacitor (EDLC). *Journal Solid State Electrochemistry*, 14, 2145-2152.

Asghar, A., Samad, Y. A., Lalia, B. S., & Hashaikh, R. (2012). PEG based quasi-solid polymer electrolyte: Mechanically supported by networked cellulose. *Journal of Membrane Science*, 421-422, 85-90.

Aziz, N. A., Majid, S. R., & Arof, A. K. (2012). Synthesis and characterizations of phthaloyl chitosan-based polymer electrolytes. *Journal of Non-Crystalline Solids*, 358, 1581-1590.

Aziz, S. B., & Abidin, Z. H. Z. (2014). Electrical and morphological analysis of chitosan:AgTf solid electrolyte. *Materials Chemistry and Physics*, 144, 280-286.

Azizi Samir, M. A. S., Chazeau, L., Alloin, F., Cavaillé, J. -Y., Dufresne, A., & Sanchez, J. -Y. (2005). POE-based nanocomposite polymer electrolytes reinforced with cellulose whiskers. *Electrochimica Acta*, 50, 3897-3903.

Banwell, C. N., & McCash, E. M. (2006). *Fundamentals of Molecular Spectroscopy* (4th ed.). New Delhi, India: Tata McGraw-Hill.

Baran, E. J. (2008). Spectroscopic investigation of the VO<sup>2+</sup>/chitosan interaction. *Carbohydrate Polymer*, 74, 704-706.

Baskaran, R., Selvasekarapandian, S., Hirankumar, G., & Bhuvaneshwari, M. S. (2004). Vibrational, ac impedance and dielectric spectroscopic studies of poly(vinylacetate)-*N,N*-dimethylformamide-LiClO<sub>4</sub> polymer gel electrolytes. *Journal of Power Sources*, 134, 235-240.

Boczar, M., Kurczab, R., Wojcik, M.J. (2010). Theoretical and spectroscopic studies of vibrational spectra of hydrogen bonds in molecular crystal of  $\beta$ -oxalic acid. *Vibrational Spectroscopy*, 52, 39-47.

- Bourtoom, T. (2008). Plasticizer effect on the properties of biodegradable blend film from rice starch-chitosan. *Songklanakarin Journal of Science and Technology*, 30, 149-165.
- Brett, C. M. A., & Brett, A. M. O. (1993). *Electrochemistry principles, methods and applications*. New York, NY: Oxford University Press Inc.
- Buraidah, M. H., Teo, L. P., Majid, S. R., & Arof, A. K. (2009). Ionic conductivity by correlated barrier hopping in NH<sub>4</sub>I doped chitosan solid electrolyte. *Physica B: Condensed Matter*, 404, 1373-1379
- Burke, A. (2007). R & D considerations for the performance and application of electrochemical capacitors. *Electrochimica Acta*, 53, 1083-1091.
- Cervera, M. F., Karjalainen, M., Airaksinen, S., Rantanen, J., Krogars, K., Heinamaki, J., Colarte A. I., & Yliruusi, J. (2004). Physical stability and moisture sorption of aqueous chitosan-amylose starch films plasticized with polyols. *European Journal of Pharmaceutics and Biopharmaceutics*, 58, 69-76.
- Chanderasekaran, R., Koh, M., Yamauchi, A., & Ishikawa, M. (2010). Electrochemical cell studies based on non-aqueous magnesium electrolyte for electric double layer capacitor application. *Journal of Power Sources*, 195, 662-666.
- Cheruku, R., & Govindaraj, L. G. (2012). Electrical relaxation studies of solution combustion synthesized nanocrystalline Li<sub>2</sub>NiZrO<sub>4</sub> material. *Material Science Engineering B*, 177, 771-779.
- Choi, J. W., Cheruvally, G., Kim, D. S., Ahn, J. H., Kim, K. W., Ahn, H. J. (2008). Rechargeable lithium/sulfur battery with liquid electrolytes containing toluene as additive. *Journal of Power Sources*, 183, 441-445.
- Chopra, S., Sharma, S., Goel, T. C., Mendiratta, R.G. (2003). Structural, dielectric and pyroelectric studies of Pb<sub>1-x</sub>Ca<sub>x</sub>TiO<sub>3</sub> thin films. *Solid State Communication*, 127, 299-304.
- Choudhary, S., & Sengwa, R. J. (2011). Dielectric properties and structural conformation of melt compounded PEO-LiCF<sub>3</sub>SO<sub>3</sub>-MMT nanocomposite electrolytes. *Indian Journal of Pure & Applied Physics*, 49, 600-605.
- Cui, Z., Xiang, Y., Si, J., Yang, M., Zhang, Q., & Zhang, T. (2008). Ionic interactions between sulfuric acid and chitosan membranes. *Carbohydrate Polymer*, 73, 111-116.
- Dakhara, S. L., & Anajwala, C. C. (2010). Polyelectrolyte complex: A pharmaceutical review. *Systematic Review in Pharmacy*, 1, 121-127.
- Di Noto, V., Lavina, S., Giffin, G. A., Negro, E., & Scrosati, B. (2011). Polymer electrolytes: Present, past and future. *Electrochimica Acta*, 57, 4-13.
- Dimzon, I. K. D., Ebert, J., & Knepper, T. P. (2013). The interaction of chitosan and olive oil: Effects of degree of deacetylation and degree of polymerization. *Carbohydrate Polymers*, 92, 564-570.
- Domján, A., Bajdik, J. & Pintye-Hódi, K. (2009). Understanding of the Plasticizing Effects of Glycerol and PEG 400 on Chitosan Films Using Solid-State NMR Spectroscopy. *Macromolecules*, 42, 4667-4673.

Duconseille, A., Astruc, T., Quintana, N., Filip Meersman, F., & Sante-Lhoutellier, V. (2014). Gelatin structure and composition linked to hard capsule dissolution: A review. *Food Hydrocolloids*. doi: 10.1016/j.foodhyd.2014.06.006

Emmenegger, Ch., Mauron, Ph., Sudan, P., Wenger, P., Hermann, V., Gallay, R., & Züttel, A. (2003). Investigation of electrochemical double-layer (ECDL) capacitors electrodes based on carbon nanotubes and activated carbon materials. *Journal of Power Sources*, 124, 321-329.

Fang, Y., Jiang, F., Liu, H., Wu, X., & Lu, Y. (2012). Free-standing Ni-microfiber-supported carbon nanotube aerogel hybrid electrodes in 3D for high-performance supercapacitor. *Royal Society of Chemistry Advances*, 2, 6562-6569.

Feng, F., Liu, Y., Zhao, B., Hu, K. (2012). Characterization of half-acetylated chitosan powders and films. *Procedia Engineering: Proceedings of Chinese Material Conference 2011*, 27, 718-732. New York, NY: Curran Associates, Inc.

Feng, L., Zhu, Y., Ding, H., & Ni, C. (2014). Recent progress in nickel based materials for high performance pseudocapacitor electrodes. *Journal of Power Sources*, 267, 430-444.

Forsyth, M., Meakin, P. M. & MacFarlane, D. R. (1995). A <sup>13</sup>C NMR study of the role of plasticizers in the conduction mechanism of solid polymer electrolytes. *Electrochimica Acta*, 40, 2339-2342.

Frackowiak, E. & Beguin, F. (2001). Carbon materials for the electrochemical storage of energy in capacitors. *Carbon*, 39, 937-950.

Fuentes, S., Retuert P. J., & González, G. (2003). Transparent conducting polymer electrolyte by addition of lithium to the molecular complex chitosane-poly(aminopropyl siloxane). *Electrochimica Acta*, 48, 2015-2019.

Fundo, J. F., Fernandes, R., Almeida, P. M., Carvalho, A., Feio, G, Silva C. L. M., & Quintas, M. A. C. (2014). Molecular mobility, composition and structure analysis in glycerol plasticised chitosan films. *Food chemistry*, 144, 2-8.

Gómez-Guillén, M.C., Pérez-Mateos, M., Gómez-Estaca, J., López-Caballero, E., Giménez B., & Montero, P. (2009). Fish gelatin: a renewable material for developing active biodegradable films. *Trends in Food Science & Technology*, 20, 3-16.

Gómez-Siurana, A., Marcilla, A., Beltrán, M., Berenguer, D., Martínez-Castellanos, I., & Menargues, S. (2013). TGA/FTIR study of tobacco and glycerol-tobacco mixtures. *Thermochimica Acta*, 573, 146-157.

Grant, S., Blair, H. S. & McKay, G. (1989). Structural studies on chitosan and other chitin derivatives. *Die Makromolekulare Chemie*, 190, 2279-2286.

Gümüsoğlu, T, Arı, G. A., & Deligöz, H. (2011). Investigation of salt addition and acid treatment effects on the transport properties of ionically cross-linked polyelectrolyte complex membranes based on chitosan and polyacrylic acid. *Journal of Membrane Science*, 376, 25-34.

Han, H. B., Zhou, S. S., Zhang, D. J., Feng, S. W., Li, L. F., Liu, K., ... Zhou, Z. B. (2011). Lithium bis(fluorosulfonyl)imide (LiFSI) as conducting salt for nonaqueous

liquid electrolytes for lithium-ion batteries: Physicochemical and electrochemical properties. *Journal of Power Sources*, 196, 3623-3632.

Hashmi S. A., Kumar, A., & Tripathi, S. K. (2007). Experimental studies on poly methyl methacrylate based gel polymer electrolytes for application in electrical double layer capacitors. *Journal Physical D Applied Physics*, 40, 6527-6534.

Hashmi, S. A., & Upadhyaya, H. M. (2002). Polypyrrole and poly(3-methyl thiophene)-based solid state redox supercapacitors using ion conducting polymer electrolyte. *Solid State Ionics*, 152-153, 883-889.

Hashmi, S.A., Kumar, A., Maurya, K.K., Chandra, S. (1990). Proton-conducting polymer electrolyte I. The polyethylene oxide  $\text{NH}_4\text{ClO}_4$  system. *Journal of Physics D: Applied Physics*, 23, 1307-1314.

Hassan, F., Woo, H. J., Aziz, N. A., Kufian, M. Z., & Majid, S. R. (2013). Synthesis of  $\text{Al}_2\text{TiO}_5$  and its effect on the properties of chitosan- $\text{NH}_4\text{SCN}$  polymer electrolytes. *Ionics*, 19, 483-489.

Hernández-Molina, J. M., Cordero-Lorenzo, M., & Otero, J. (2004). Computational study of the dissociation of oxalic acid in water clusters. *Chemical Physics*, 302, 53-60.

Huang, J., Xu, Z., Zhao, S., Li, S., Feng, X., Wang, P., & Zhang, Z. (2010). Study on carrier mobility measurement using electroluminescence in frequency domain and electrochemical impedance spectroscopy. *Measurement*, 43, 295-298.

Il'ina, A. V., & Voronov, V. P. (2005). Chitosan-based polyelectrolyte complexes: A review. *Applied Biochemistry and Microbiology*, 41, 5-11.

Imperiya, M., Ahmad, A., Hanifah, S. A., Mohamed, N. S., & Rahman M. Y. A. (2014). Investigation of plasticized UV-curable glycidyl methacrylate based solid polymer electrolyte for photoelectrochemical cell (PEC) application. *International Journal of Hydrogen Energy*, 39, 3018-3024.

Ingram, M. D., Staesche, H., & Ryder, K. S. (2004). 'L-proline' polypyrrole: possible electrode material for inclusion in electrochemical supercapacitors?. *Journal of Power Sources*, 129, 107-112.

Jayalakshmi, M., & Balasubramaniam, K. (2008). Simple Capacitors to Supercapacitors- An Overview. *International Journal of Electrochemical Science*, 3, 1196-1217.

Ji, Q. Q., Guo, P. Z., & Zhao, X. S. (2010). Preparation of Chitosan-Based Porous Carbons and Their Application as Electrode Materials for Supercapacitors. *Acta Physico-Chimica Sinica*, 26, 1254-1258.

Kang, J., Wen, J., Jayaram, S. H., Yu, A., Wang, X. (2014). Development of an equivalent circuit model for electrochemical double layer capacitors (EDLCs) with distinct electrolytes. *Electrochimica Acta*, 115, 587-598.

Karthikeyan, A., Vinatier, P. & Levasseur, A. (2000). Study of lithium glassy solid electrolyte/electrode interface by impedance analysis. *Bulletin of Material Science*, 23, 179-183.

- Khiar, A. S. A., Puteh, R., & Arof, A. K. (2006). Conductivity studies of a chitosan-based polymer electrolyte *Physica B*, 373, 23–27.
- Kötz, R. & Carlen, M. (2000). Principles and applications of electrochemical capacitors. *Electrochimica Acta*, 45, 2483-2498.
- Krishnakumar, V., & Shanmugam, G. (2012). Electrical and optical properties of pure and  $Pb^{2+}$  on op PVA–P G polym r compos t l c trolyt f lms *Ionics*, 18, 403-4011.
- Kumirska, J., Czerw ck M K c yńsk Z Bychowsk A Br o owsk K Thöming, J., & Stepnowski, P. (2010). Application of Spectroscopic Methods for Structural Analysis of Chitin and Chitosan. *Marine Drugs*, 8, 1567-1636.
- Kurita, K. (2001). Controlled functionalized of the polysaccharide chitin. *Progress in Polymer Science*, 26, 1921-1971.
- Kwon, S. H., Lee, E., Kim, B. S., Kim, S. G., Lee, B. J., Kim, M. S., & Jung, J. C. (2014). Activated carbon aerogel as electrode material for coin-type EDLC cell in organic electrolyte. *Current Applied Physics*, 14, 603-607.
- Lalia, B. S., Samad, Y.A., & Hashaikh, R. (2014). Ternary polymer electrolyte with enhanced ionic conductivity and thermo-mechanical properties for lithium-ion batteries. *International Journal of Hydrogen Energy*, 39, 2964-2970.
- Lassègues, J. C., Grondin, J., Servant, L., & Hernandez, M. (1995). Supercapacitor using a proton conducting polymer electrolyte. *Solid State Ionics*, 77, 311-317.
- Lavall, R. L., Borges, R. S., Calado, H. D. R., Welter, C., Trigueiro, J. P. C., Rieumont, J., Neves, B. R. A., & Silva, G. G. (2008). Solid state double layer capacitor based on a polyether polymer electrolyte blend and nanostructured carbon black electrode composites. *Journal of Power Sources*, 177, 652–659.
- Lavorgna, M., Piscitelli, F., Mangiacapra, P., & Buonocore, G. (2010). Study of the combined effect of both clay and glycerol plasticizer on the properties of chitosan films. *Carbohydrate Polymers*, 82, 291-298.
- Lazaridou, A., & Biliaderis, C. G. (2002). Thermophysical properties of chitosan, chitosan–starch and chitosan–pullulan films near the glass transition. *Carbohydrate Polymers*, 48, 179-190.
- Leceta, I., Guerrero, P., de la Caba, K. (2013). Functional properties of chitosan-based films. *Carbohydrate Polymers*, 93, 339-346.
- Lee, J. I., Kim, D. W., Lee, C., & Kang, Y. (2010). Enhanced ionic conductivity of intrinsic solid polymer electrolytes using multi-armed oligo(ethylene oxide) plasticizers. *Journal of Power Sources*, 195, 6138-6142.
- Leones, R., Sentanin, F., Rodrigues, L. C., Ferreira, R. A. S., Marrucho, I. M., Esperança, J. M. S. S., ... Silva, M. M. (2012). Novel polymer electrolytes based on gelatin and ionic liquids. *Optical Materials Volume*, 35, 187-195.
- Lewandowska, K. (2011). Miscibility and interaction in chitosan acetate/ poly(N-vinylpyrrolidone) blends. *Thermochimica Acta*, 517, 90-97.

- Lewandowski, A., & Świrski, A. (2006). Solvent-free double-layer capacitors with polymer electrolytes based on 1-ethyl-3-methyl-imidazolium triflate ionic liquid. *Applied Physics A*, 82, 579-584.
- Lewandowski, A., & Olejniczak, A. (2007). N-Methyl-N-propylpiperidinium bis(trifluoromethanesulphonyl)imide as an electrolyte for carbon-based double-layer capacitors. *Journal of Power Sources*, 172, 487-492.
- Lewandowski, A., Zajder, M., Frąckowski, & Béguin, F. (2001). Supercapacitor based on activated carbon and polyethylene oxide-KOH-H<sub>2</sub>O polymer electrolyte. *Electrochimica Acta*, 46, 2777-2780.
- Li, W., Chen, D., Li, Z., Shi, Y., Wan, Y., Wang, G., Jiang, Z., Zhao, D. (2007). Nitrogen-containing carbon spheres with very large uniform mesopores: The superior electrode materials for EDLC in organic electrolyte. *Carbon*, 45, 1757-1763.
- Lian, F., Guan, H. Y., Wen, Y., & Pan, X. R. (2014). Polyvinyl formal based single-ion conductor membranes as polymer electrolytes for lithium ion batteries. *Journal of Membrane Science*, 469, 1 November 2014, 67-72.
- Liew, C. W., Ramesh, S., & Arof, A. K. (2014). Good prospect of ionic liquid based-poly(vinyl alcohol) polymer electrolytes for supercapacitors with excellent electrical, electrochemical and thermal properties. *International Journal of Hydrogen Energy*, 39, 2953-2963.
- Lindman, B. B., Karlström, G., & Stigsson, L. L. (2010). On the mechanism of dissolution of cellulose. *Journal of Molecular Liquids*, 156, 76-81.
- Liu, G., Kang, F., Li, B., Huang, Z., & Chuan, X. (2006). Characterization of the porous carbon prepared by using halloysite as template and its application to EDLC. *Journal of Physics and Chemistry of Solids*, 67, 1186-1189.
- Liu, H., Adhikari, R., Guo, Q., & Adhikari, B. (2013). Preparation and characterization of glycerol plasticized (high-amylose) starch-chitosan films. *Journal of Food Engineering*, 116, 588-597.
- Luo, Y., & Wang, Q. (2014). Recent development of chitosan-based polyelectrolyte complexes with natural polysaccharides for drug delivery. *International Journal of Biological Macromolecules*, 64, March 2014, 353-367.
- Ma, G., Peng, H., Mu, J., Huang, H., Zhou, X., & Lei, Z. (2013). In situ intercalative polymerization of pyrrole in graphene analogue of MoS<sub>2</sub> as advanced electrode material in supercapacitor. *Journal of Power Sources*, 229, 72-78.
- Ma, G., Li, J., Sun, K., Peng, H., Mu, J., & Lei, Z. (2014). High performance solid-state supercapacitor with PVA-KOH-K<sub>3</sub>[Fe(CN)<sub>6</sub>] gel polymer as electrolyte and separator. *Journal of Power Sources*, 256, 281-287.
- Ma, X., Chang, P. R., Yu, J., Lu, P. (2008). Characterizations of glycerol plasticized-starch (GPS)/carbon black (CB) membranes prepared by melt extrusion and microwave radiation. *Carbohydrate Polymers*, 74, 895-900.
- Macdonald, J. R., & Johnson, W. B. (2005). Fundamentals of Impedance Spectroscopy. In Barsoukov, E., & Macdonald, J. R. (Eds.), *Impedance*

*Spectroscopy Theory, Experiment, and Applications* (2nd ed., pp.1-20). New Jersey, USA: John Wiley & Sons, Inc.

MacFarlane, D. R., Sun, J., Meakin, P., Fasoulopoulos, P., Hey, J., & Forsyth, M. (1995). Structure-property relationships in plasticized solid polymer electrolytes. *Electrochimica Acta*, *40*, 2131-2136.

Machado, G. O., Ferreira, H. C. A., & Pawlicka, A. (2005). Influence of plasticizer contents on the properties of HEC-based solid polymeric electrolytes. *Electrochimica Acta*, *50*, 3827-3831.

Majid, S. R., & Arof, A. K. (2007). Electrical behavior of proton-conducting chitosan-phosphoric acid-based electrolytes. *Physica B*, *390*, 209-215.

Masuda, Y., Nakayama, M., & Wakihara, M. (2007). Fabrication of all solid-state lithium polymer secondary batteries using PEG-borate/aluminate ester as plasticizer for polymer electrolyte. *Solid State Ionics*, *178*, 981-986.

Matsuura, Y., Oshima, Y., Tanaka, K., & Yamabe, T. (1996). AC conductivity of C<sub>60</sub>-doped poly (*o*-ethylaniline). *Synthetic Metals*, *79*, 7-10.

McKubre, M. C. H., & Macdonald, D. D. (2005). Measuring Techniques and Data Analysis (2nd ed.). In E. Barsoukov & J. R. Macdonald, (Eds.), *Impedance Spectroscopy Theory, Experiment, and Applications* (pp. 129-204). New Jersey, NJ: John Wiley and Sons Inc.

Michael, M. S., & Prabakaran S. R. S. (2004). Rechargeable lithium battery employing a new ambient temperature hybrid polymer electrolyte based on PVK+PVdF-HFP (copolymer). *Journal of Power Sources*, *136*, 408-415.

Missan, H. P. S., Chu, P. P., & Shekon, S. S. (2006). Ion conduction mechanism in non-aqueous polymer electrolytes based on oxalic acid: Effect of plasticizer and polymer. *Journal of Power Sources*, *158*, 1472-1479.

Mobarak N. N., Ahmad, A., Abdullah, M. P., Ramli, N., & Rahman M. Y. A. (2013). Conductivity enhancement via chemical modification of chitosanbased green polymer electrolyte. *Electrochimica Acta*, *92*, 161-167.

Mourya, V. K., & Inamdar, N. N. (2008). Chitosan-modifications and applications: Opportunities galore. *Reactive and Functional Polymers*, *68*, 1013-1051.

Muzzarelli, R. A. A. (1978). *Chitin*. Great Britain: Pergamon Press Ltd.

Muzzarelli, R. A. A., Boudrant, J., Meyer, D., Manno, N., DeMarchis, M. & Paoletti, M. G. (2012). Current views on fungal chitin/chitosan, human chitinases, food preservation, glucans, pectins and inulin: A tribute to Henri Braconnot, precursor of the carbohydrate polymers science, on the chitin bicentennial. *Carbohydrate Polymers*, *87*, 995-1012.

Ng, L. S., & Mohamad, A. A. (2008). Effect of temperature on the performance of proton batteries based on chitosan-NH<sub>4</sub>NO<sub>3</sub>-EC membrane. *Journal of Membrane Science*, *325*, 653-657.

Ng, L. S., & Mohamad, A. A. (2006). Protonic battery based on a plasticized chitosan-NH<sub>4</sub>NO<sub>3</sub> solid polymer electrolyte. *Journal of Power Sources*, *163*, 382-385.

- Nithya, H., Selvasekarapandian, S., Selvin, P. C., Kumar, D. A., & Kawamura, J. (2012). Effect of propylene carbonate and dimethylformamide on ionic conductivity of P(ECH-EO) based polymer electrolyte. *Electrochimica Acta*, *66*, 110–120.
- Niya, S. M. R., & Hoorfar, M. (2013). Study of proton exchange membrane fuel cells using electrochemical impedance spectroscopy technique. *Journal of Power Sources*, *240*, 281-293.
- Nohara, S., Wada, H., Furukawa, N., Inoue, H., Morita, M., & Iwakura, C. (2003). Electrochemical characterization of new electric double layer capacitor with polymer hydrogel electrolyte. *Electrochimica Acta*, *48*, 749–753.
- Nomoto, S., Nakata, H., Yoshioka, K., Yoshida, A., & Yoneda, H. (2001). Advanced capacitors and their application. *Journal of Power Sources*, *97-98*, 807-811.
- Osman, Z., Ibrahim, Z. A., & Arof, A. K. (2001). Conductivity enhancement due to ion dissociation in plasticized chitosan based polymer electrolytes. *Carbohydrate Polymers*, *44*, 167-173.
- Pandey, G. P., Kumar, S., & Hashmi, S. A. (2011). Ionic liquid incorporated PEO based polymer electrolyte for electrical double layer capacitors: A comparative study with lithium and magnesium system. *Solid State Ionics*, *190*, 93-98.
- Pandey, K., Asthana, N., Dwivedi, M. M. & Chaturvedi, S. K. (2013). Effect of Plasticizers on Structural and Dielectric Behaviour of [PEO + (NH<sub>4</sub>)<sub>2</sub>C<sub>4</sub>H<sub>8</sub>(COO)<sub>2</sub>]. *Polymer Electrolyte Journal of Polymers*, *2013*, 1-12.
- Pandolfo, A. G. & Hollenkamp, A. F. (2006). Carbon properties and their role in supercapacitors. *Journal of Power Sources*, *157*, 11-27.
- Patrice Simon, P. & Gogotsi, Y. (2008). Materials for electrochemical capacitors. *Nature Materials*, *7*, 845-854.
- Pawlak, A., Mucha, M. (2003). Thermogravimetric and FTIR studies of chitosan blends. *Thermochimica Acta*, *396*, 153-166.
- Pawlicka, A., & Donoso, J. P. (2010). Polymer electrolyte based on natural polymers. In Sequira, C. & Santos, D. *Polymer electrolytes: Fundamentals and applications*. (pp. 95-124). Cambridge, UK: Woodhead Publishing Limited.
- Pawlicka, A., Danczuk, M., Wieczorek, W., & Zylło-Monikowska E. (2008). Influence of plasticizer type on the properties of polymer electrolytes based on chitosan. *Journal of Physical Chemistry A*, *112*, 8888-8895.
- Pernaut, J. M., & Goulart, G. (1995). Electrochemical capacitor using polymer/carbon composites. *Journal of Power Sources*, *55*, 93–96.
- Pradhan, D. K., Choudhary, R. N. P., Samantaray, B. K., Karan, N. K. & Katiyar, R. S. (2007). Effect of plasticizer on Structural and Electrical Properties of Polymer Nanocomposite Electrolytes. *International Journal of Electrochemical Science*, *2*, 861-871.
- Qian, X., Gu, N., Cheng, Z., Yang, X., Wang, E., & Dong, S. (2002). Plasticizer effect on the ionic conductivity of PEO-based polymer electrolyte. *Materials Chemistry and Physics*, *74*, 98–103.

- Rajendran, S., Babu, R. S., & Sivakumar, P. (2007). Effect of salt concentration on poly (vinyl chloride)/poly (acrylonitrile) based hybrid polymer electrolytes. *Journal of Power Sources*, 170, 460-464
- Ramasamy, C., Palma del Val, J., Anderson, M. (2014). An electrochemical cell study on polyvinylpyrrolidone aqueous gel with glycol addition for capacitor applications. *Electrochimica Acta*, 135, 181-186.
- Ravi Kumar, M. N. V. (2000). A review of chitin and chitosan applications. *Reactive and Functional Polymers*, 46, 1-27.
- Ravi Kumar, V., & Veeraiah, N. (1998). Dielectric properties of ZnF<sub>2</sub>-PbO-TeO<sub>2</sub> glasses. *Journal Physics and Chemistry of Solids*, 59, 91-97.
- Reicha, F. M., El-Heiti, M., El-Sonabati, A. Z., Diab, & M. A., (1991). Conducting polymers. V. Electrical conductivity of polymer complexes of bis-2,6-diaminopyridinesulphoxide-copper halides. *Journal of Physics D: Applied Physics*, 24, 369-374.
- Ritthidej, G. C., Phaechamud, T., Koizumi, T. (2002). Moist heat treatment on physicochemical change of chitosan salt films. *International Journal of Pharmaceutics*, 232, 11-22.
- Saikia, D., Wu, H. Y., Pan, Y. C., Lin, C. P., Huang, K. P., Chen, K. N., Fey, G. T. K., & Kao, H. M. (2011). Highly conductive and electrochemically stable plasticized blend polymer electrolytes based on PVdF-HFP and triblock copolymer PPG-PEG-PPG diamine for Li-ion batteries. *Journal of Power Sources*, 196, 2826–2834.
- Sajomsang, W. (2010). Synthetic methods and applications of chitosan containing pyridylmethyl moiety and its quaternized derivatives: A review. *Carbohydrate Polymers*, 80, 631-647.
- Samir, A., Alloin, F., Gorecki, W., Sanchez, J., & Dufresne, A. (2004). Nanocomposites polymer electrolytes based on poly(oxyethylene) and cellulose nanocrystal. *Journal of Physical Chemistry B*, 108, 10845–10852.
- Saroj, A. L. & Singh R. K. (2012). Thermal, dielectric and conductivity studies on PVA/Ionic liquid [EMIM][EtSO<sub>4</sub>] based polymer electrolytes, *Journal of Physics and Chemistry of Solids*, 73, 162–168.
- Sekhar. P. K., Sarraf, H., Mekonen, H., Mukundan, R., Brosha, E. L., & Garzon, F. H. (2013). Impedance spectroscopy based characterization of an electrochemical propylene sensor. *Sensors and Actuators B*, 177, 111-115.
- Selvasekarapandian, S., Baskaran, R., Kamishima, O., Kawamura, J., Hattori, T. (2006). Laser Raman and FTIR studies on Li<sup>+</sup> interaction in PVAc–LiClO<sub>4</sub> polymer electrolytes. *Spectrochimica Acta Part A: Molecular and Biomolecular Spectroscopy*, 65, 1234–1240.
- Selvasekarapandian, S., Baskaran, R., & Hema, M. (2005). Complex AC impedance, transference number and vibrational spectroscopy studies of proton conducting PVAc-NH<sub>4</sub>SCN polymer electrolytes. *Physica B*, 357, 412-419.
- Sengwa, R. J., Dhatarwal P., & Choudhary, S. (2014). Role of preparation methods on the structural and dielectric properties of plasticized polymer blend electrolytes:

- Correlation between ionic conductivity and dielectric parameters. *Electrochimica Acta*, 142, 359–370.
- Senthilkumar, S. T., Kalai Selvan, R., Ponpandian, N., & Melo, J. S. (2012). Redox additive aqueous polymer gel electrolyte for an electric double layer capacitor. *Royal Chemistry Society Advances*, 2, 8937-8940.
- Sequeira, C. A. C., & Santos, D. M. F. (2010). Introduction to polymer electrolyte materials. In Sequeira, C. & Santos, D. *Polymer electrolytes: Fundamentals and applications*. (pp. 1-52). Cambridge, UK: Woodhead Publishing Limited.
- Sharma, P., & Bhatti, T. S. (2010). A review on electrochemical double layer. *Energy Conversion and Management*, 51, 2901-2912.
- Shin, J. H., Jeong, S. S., Kim, K. W., & Passerini, S. (2005). FT-Raman spectroscopy study on the effect of ceramic fillers in P(EO)<sub>20</sub>LiBETI. *Solid State Ionics*, 176, 571-577.
- Shriver, D. F., Atkins P. W., & Langford, C. H. (1994). *Inorganic Chemistry* (2nd ed.). Oxford, Great Britain: Oxford University Press.
- Shukla, S. K., Ajay K. Mishra, A. K., Arotiba, O. A., & Mamba, B. B. (2013). Chitosan-based nanomaterials: A state-of-the-art review. *International Journal of Biological Macromolecules*, 59, 46-58.
- Simon, P., & Burke, A. (2008). Nanostructured carbons: Double layer capacitance and more. *The Electrochemical Society*, 17, 38-43.
- Singh, K. P., & Gupta, P. N. (1998). Study of dielectric relaxation in polymer electrolytes. *European Polymer Journal*, 34, 1023-1029.
- Sivaraman, P., Kushwaha, R. K., Shashidhara, K., Hande, V. R., Thakur, A. P., Samui, A. B., & Khandpekar, M. M. (2010). All solid supercapacitor based on polyaniline and crosslinked sulfonated poly[ether ether ketone]. *Electrochimica Acta*, 55, 2451–2456.
- Solomon, T. W. G., & Fryle. C. (2004). *Organic Chemistry* (8th ed.) U. P. Noida, India: Wiley International Edition.
- Staiti, P., Minutoli, M., & Lufrano, F. (2002). All solid electric double layer capacitors based on Nafion ionomer. *Electrochimica Acta*, 47, 2795–2800.
- Stewart, K. C., Kolman, D. G., & Taylor, S. R. (1993). The effect of parasitic conduction pathways on EIS measurements in low conductivity media. In J. R. Scully, D. C. Silverman, M. W. Kendig, (Eds.), *Electrochemical Impedance: Analysis and Interpretation, ASTM STP 1188*, (pp. 73-93). Philadelphia: American Society for Testing and Materials.
- Subramania, A., Sundaram N. T. K., & Kumar, G.V. (2006). Structural and electrochemical properties of micro-porous polymer blend electrolytes based on PVdF-co-HFP-PAN for Li-ion battery applications. *Journal of Power Sources*, 153, 23 January, 177-182.
- Sudhakar, Y. N., & Selvakumar, M. (2012). Lithium perchlorate doped plasticized chitosan and starch blend as biodegradable polymer electrolyte for supercapacitors. *Electrochimica Acta*, 78, 398-405.

Suhaimi, N. E. A., Teo, L. P., Woo, H. J., Majid, S. R., & Arof, A. K. (2012). Electrical double-layer capacitors with plasticized polymer electrolyte based on methyl cellulose. *Polymer Bulletin*, *69*, 807-826.

Sukhla, A. K., Sampath, S., & Vijayamohanan, K. (2000). Electrochemical supercapacitors: energy storage beyond batteries. *Current Science*, *79*, 1656-1661.

Venkatesan, S., Obadja, N., Chang, T. W., Chen, L. T., & Lee, Y. L. (2014). Performance improvement of gel- and solid-state dye-sensitized solar cells by utilization the blending effect of poly (vinylidene fluoride-co-hexafluoropropylene) and poly (acrylonitrile-co-vinyl acetate) co-polymers. *Journal of Power Sources*, *268*, 77-81.

Vicentini, D. S., Smania Jr., A., Laranjeira, M. C. M. (2010) Chitosan/poly (vinyl alcohol) films containing ZnO nanoparticles and plasticizers. *Material Science and Engineering: C*, *30*, 503-508.

Wada, H., Nohara, S., Furukawa, N., Inoue, H., Sugoh, N., Iwasaki, H., Morita, M., & Chiaki Iwakura, C. (2004). Electrochemical characteristics of electric double layer capacitor using sulfonated polypropylene separator impregnated with polymer hydrogel electrolyte. *Electrochimica Acta*, *49*, 4871-4875.

Wan, Y., Creber, K. A. M., Peppley, B., & Bui, V. T. (2003). Ionic conductivity of chitosan membranes. *Polymer*, *44*, 1057-1065.

Wang, J. G., Yang, Y., Huang, Z. H., & Kang, F. (2013). A high-performance asymmetric supercapacitor based on carbon and carbon-MnO<sub>2</sub> nanofiber electrodes. *Carbon*, *61*, 190-199.

Wen, S., Lee, J. W., Yeo, I. H., Park, J., Mho, S. I. (2004). The role of cations of the electrolyte for the pseudocapacitive behavior of metal oxide electrodes, MnO<sub>2</sub> and RuO<sub>2</sub>. *Electrochimica Acta*, *50*, 849-855.

Wen, Z., Itoh, T., Uno, T., Kubo, M., & Yamamoto, O. (2003). Thermal, electrical, and mechanical properties of composite polymer electrolytes based on cross-linked poly(ethylene oxide-co-propylene oxide) and ceramic filler. *Solid State Ionics*, *160*, 141-148.

Winie, T., & Arof, A. K. (2004). Dielectric Behaviour and AC conductivity of LiCF<sub>3</sub>SO<sub>3</sub> doped H-Chitosan polymer films. *Ionics*, *10*, 193-199.

Winie, T., Ramesh, S., & Arof, A. K. (2009). Studies on the structure and transport properties of hexanoyl chitosan-based polymer electrolytes. *Physica B: Condensed Matter*, *404*, 4308-4311.

Woo, H. J., Majid, S. R. & Arof, A. K. (2012). Dielectric properties and morphology of polymer electrolytes on poly( $\epsilon$ -caprolactone) and ammonium thiocyanate. *Materials Chemistry and Physics*, *134*, 755-761.

Wu, H., Hou, W., Wang, J., Xiao, L., & Jiang, Z. (2010). Preparation and properties of hybrid direct methanol fuel cell membranes by embedding organophosphorylated titania submicrospheres into a chitosan polymer matrix. *Journal of Power Sources*, *195*, 4104-4113.

- Xiang, Y., Yang, M., Guo, Z., & Cui, Z. (2009). Alternatively chitosan sulfate blending membrane as methanol-blocking polymer electrolyte membrane for direct methanol fuel cell. *Journal of Membrane Science*, 337, 318-323.
- Xu, W., Deng, Z. H., Zhang X. Z., & Wan, G. X. (1998). The influence of the compatibility of plasticizers with polymer ionic conductors on ionic conduction. *Journal of Solid State Electrochemistry*, 2, 257-261.
- Yalcinkaya, S., Demetgul, C., Timur, M., & Colak, N. (2010). Electrochemical synthesis and characterization of polypyrrole/chitosan composite on platinum electrode: Its electrochemical and thermal behavior. *Carbohydrate Polymers*, 79, 908-913.
- Yang, C. C., Hsu, S. T., & Chien, W. C. (2005). All solid-state electric double-layer capacitors based on alkaline polyvinyl alcohol polymer electrolytes. *Journal of Power Sources*, 152, 303-310.
- Yap, K. S., Teo, L. P., Sim, L. N., Majid, S. R., & Arof, A. K. (2012). Investigation on dielectric relaxation of PMMA-grafted natural rubber incorporated with  $\text{LiCF}_3\text{SO}_3$ . *Physica B: Condensed Matter*, 407, 2421-2428.
- Yu, H., Wu, J., Fan, L., Lin, Y., Xu, K., Tang, Z., Cheng, C., Tang, S., Lin, J., Huang M., & Lan, Z. (2012). A novel redox-mediated gel polymer electrolyte for high-performance supercapacitor. *Journal of Power Sources*, 198, 402-407.
- Yu, H., Wu, J., Fan, L., Xu, K., Zhong, X., Lin, Y., & Lin, J. (2011). Improvement of the performance for quasi-solid-state supercapacitor by using PVA-KOH-KI polymer gel electrolyte. *Electrochimica Acta*, 56, 6881-6886.
- Zhang, H., Zhang, W., Cheng, J., Cao, G., & Yang Y. (2008). Acetylene black agglomeration in activated carbon based electrochemical double layer capacitor electrodes. *Solid State Ionics*, 179, 1946-1950.
- Zhang, Y., Feng, H., Wu, X., Wang, L., Zhang, A., Xia, T., Dong, H., Li, X., & Zhang, L. (2009). Progress of electrochemical capacitor electrode materials: A review. *International Journal of Hydrogen Energy*, 34, 4889-4899.
- Zhang, Y., Xue, C., Xue, Y., Gao R., & Zhang, X. (2005). Determination of the degree of deacetylation of chitin and chitosan by X-ray powder diffraction. *Carbohydrate Research*, 340, 1914-1917.
- Zheng, C., Qi, L., Yoshio, M., & Wang, H. (2010). Cooperation of micro- and meso-porous carbon electrode materials in electric double-layer capacitors. *Journal of Power Sources*, 195, 4406-4409.